united nations
educational, scientific
and cultural
organization

international atomic
energy agency

the
abdus salam
international centre for theoretical physics

H4.SMR/1241-16

"Workshop on Three-Dimensional Modelling
of Seismic Waves Generation and their Propagation"

25 September - 6 October 2000

INVERSION OF FOCAL MECHANISMS FOR STRESS FIELD DETERMINATION

F.H. CORNET

Institut de Physique du Globe de Paris
France

Inversion of Focal Mechanisms for Stress field determination

F.H. Cornet
Institut de Physique du Globe de Paris

Lecture notes prepared for

Workshop on three dimensional modeling of Seismic Waves Generation, Propagation and their inversion

UNESO Abdus Salam International Center for Theoretical Physics

Trieste; 25 September – 6 October 2000

Table of content

One of the key variables involved in the understanding of deformation processes of the crust is stress. Because stresses are an essential boundary condition to many an applied engineering problem, be it mining, civil or petroleum, most techniques for determining stresses at depth have involved measurements in boreholes. But deformation processes in the crust involve depths that are generally not accessible to boreholes. Hence, methods based on remote observations are being developed for determining the stress field at depth greater than a few kilometers. Presently two methods are being used routinely, the analysis of shear wave polarization (shear wave splitting analysis) and the inversion of double couple focal mechanisms.

This presentation first recalls some elementary principles for stability analysis. Then two methods of fault plane solution inversions are presented. Examples where they have been applied are discussed. They help precise conditions that must be satisfied for the methods to be valid. It is shown that, when applied to microseismicity induced by fluid injections, they may help to map the pore pressure field. An example chosen from a geothermal field located on a creeping segment of the Philippine fault shows that this fault segment is normal to the regional **minimum** principal stress direction.

1.Elementary failure criteria for the crust

(Typing convention: bold letters are vectors, bold letters underlined by tilde are tensors)

1.1 the stress vector and the Mohr representation

The stress vector is defined by:

$$\mathbf{t} = \underset{\sim}{\sigma}\,\mathbf{n}, \qquad (1)$$

t is the stress vector acting on a surface element S, with normal **n** and unit area, on which exists at all points the stress tensor $\underset{\sim}{\sigma}$. In this expression, the unit area is assumed to be small as compared to distances for which stress variations are significant so that stress gradients may be neglected. Hence, all components of the stress tensor are constant.

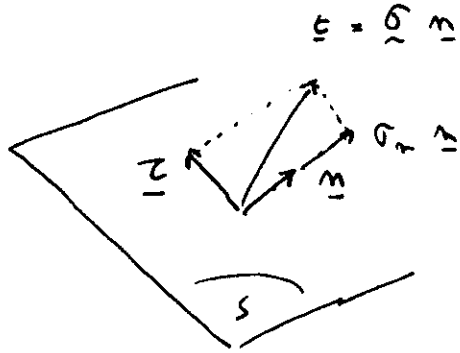

The stress vector has a normal component, (called the normal stress (scalar)) :

$$\sigma_n = \underset{\sim}{\sigma}\,\mathbf{n} \cdot \mathbf{n} \qquad (2)$$

and a shear component (vector):

$$\tau = \underset{\sim}{\sigma}\,\mathbf{n} - (\underset{\sim}{\sigma}\,\mathbf{n} \cdot \mathbf{n})\,\mathbf{n} \qquad (3)$$

The stress tensor $\underset{\sim}{\sigma}$ is symmetrical when there exists no moment in any small volume of the body under consideration. Hence it is characterized by six components, i.e. σ_{ij} , with i, j = 1,2,3, the components in any frame of reference, or its eigen values (σ_1 , σ_2 , σ_3 , with the classical convention $\sigma_3 < \sigma_2 < \sigma_1$) and its eigen vectors $\mathbf{e_1}$, $\mathbf{e_2}$, $\mathbf{e_3}$. The eigen vectors are defined by three independent angles, called the Euler angles, namely ψ , φ and θ. ψ and φ correspond to the azimuth and dip of $\mathbf{e_1}$ in the frame of reference (defined by the unit vectors $\mathbf{I_1}$, $\mathbf{I_2}$, $\mathbf{I_3}$, which may be the geographical frame of reference so that North is $\mathbf{I_1}$, East is $\mathbf{I_2}$, and $\mathbf{I_3}$ is vertical positive downward). Once the frame of reference has been rotated so that $\mathbf{I_1}$ becomes $\mathbf{e_1}$ and $\mathbf{I_2}$ becomes $\mathbf{I_2'}$, θ is the rotation about $\mathbf{e_1}$ which brings $\mathbf{I_2'}$ parallel to $\mathbf{e_2}$.

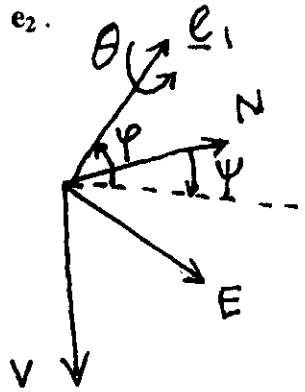

For $\mathbf{n}$ parallel to any eigen vector, $\tau = \mathbf{0}$. Given that σ_n and $|\tau|$ vary with the orientation of $\mathbf{n}$, the set of all couples of values σ_n and $|\tau|$ corresponds to the area limited by the three Mohr circles as shown on figure 1.

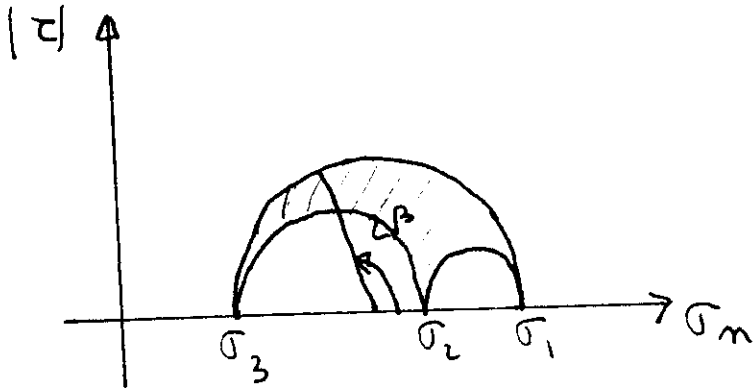

Figure 1 : The Mohr Circles. Each circle corresponds to the set of values for σ_n and $|\tau|$ when $\mathbf{n}$ is perpendicular to either $\mathbf{e_1}$, $\mathbf{e_2}$ or $\mathbf{e_3}$.

When $\mathbf{n}$ is perpendicular to $\mathbf{e_2}$, the values for σ_n and $|\tau|$ are :

$$\sigma_n = (\sigma_1 + \sigma_3)/2 + [(\sigma_1 - \sigma_3)/2]\cos(2\beta) \qquad (4)$$

$$|\tau| = [(\sigma_1 - \sigma_3)/2]\sin(2\beta) \qquad (5)$$

where β is the angle between the normal $\mathbf{n}$ and $\mathbf{e_1}$ (see figure 1)

The rock mass is globally in equilibrium (i.e. in between slip events, whether seismic or aseismic), so that the stress components must satisfy the equilibrium equation:

$$\sigma_{ij,i} + \rho\, b_j = 0 \; ; \; i, j = 1,3 \qquad (6)$$

with $\mathbf{b} = g\delta_{j3}\, \mathbf{I}_j$, the gravity, and ρ the rock density. Typically, for rocks, the vertical component of the vertical stress gradient is of the order of 2 to 3 mPa per 100 meters.

1.2. Stress failure criteria for rock masses submitted to compressive stresses

A rock mass involves both, intact rock volumes and preexisting fractures and faults. Hence failure criteria must address both the failure of intact rocks and that of preexisting weakness planes.

1.2.1 Criteria of failure for intact rocks

Once the minimum principal stress gets larger than 2 to 5 mPa, failure in compression involves the formation of macroscopic shear zones. Various stress criteria have been proposed to characterize the stress condition that must be met for these shear zones to appear.

The Tresca criterion.

$$(\sigma_1 - \sigma_3) = K \qquad (7)$$

The Tresca criterion assumes that failure occurs when the maximum differential stress in the material reaches a critical value, which is independent of the minimum principal stress magnitude. Note (see the Mohr representation on figure 2) that this assumes that the corresponding shear zone is inclined 45 ^{o} to the maximum stress orientation. Laboratory work has shown that for rock, this is valid only for very soft material like clay or salt, or for stress and temperature conditions which, for most rocks, correspond to depths greater than 20 km. It is not valid for seismicity observed in the upper 10 to 15 km.

The Coulomb criterion and the Mohr envelope

$$|\tau| = \mu\, \sigma_n + C_0 \qquad (8)$$

μ is called the internal friction angle and C_0 is called the cohesion. This criterion has been found to be valid for limited stress domains. For large stress domains the so-called friction angle decreases as the minimum principal stress increases. It gets close to 0 when both the minimum principal stress and the temperature gets large so that the criterion of failure gets close to the Tresca criterion (see figure 2). Hence the failure criterion is not represented by the simple linear law proposed by Coulomb but may be approached by a parameterization of the so-called Mohr envelope. This envelope corresponds to the set of values for $|\tau|$ and σ_n for which failure occurs. It is often assumed to be independent of the intermediate principal stress magnitude, so that failure surfaces are assumed to be parallel to the intermediate principal stress direction. However recent laboratory work, in particular by Haimson et al.(1997), has shown this not always to be valid. This will not be discussed further here for it has no incidence for our discussion

The effective stress principle

When the rock mass is saturated with a fluid under pressure, experiments show that, under compressive conditions, failure is controlled by so-called effective stresses rather than by total stresses. The effective stress tensor $\underset{\sim}{\sigma}'$ is defined as :

$$\underset{\sim}{\sigma}' = \underset{\sim}{\sigma} - P\underset{\sim}{I} \qquad (9)$$

where **I** is the unit tensor and P is pore pressure. Note that, on the Mohr diagram, subtracting P to all diagonal terms of the stress tensor matrix corresponds to shifting all Mohr circles to the left, leaving unchanged their radius.

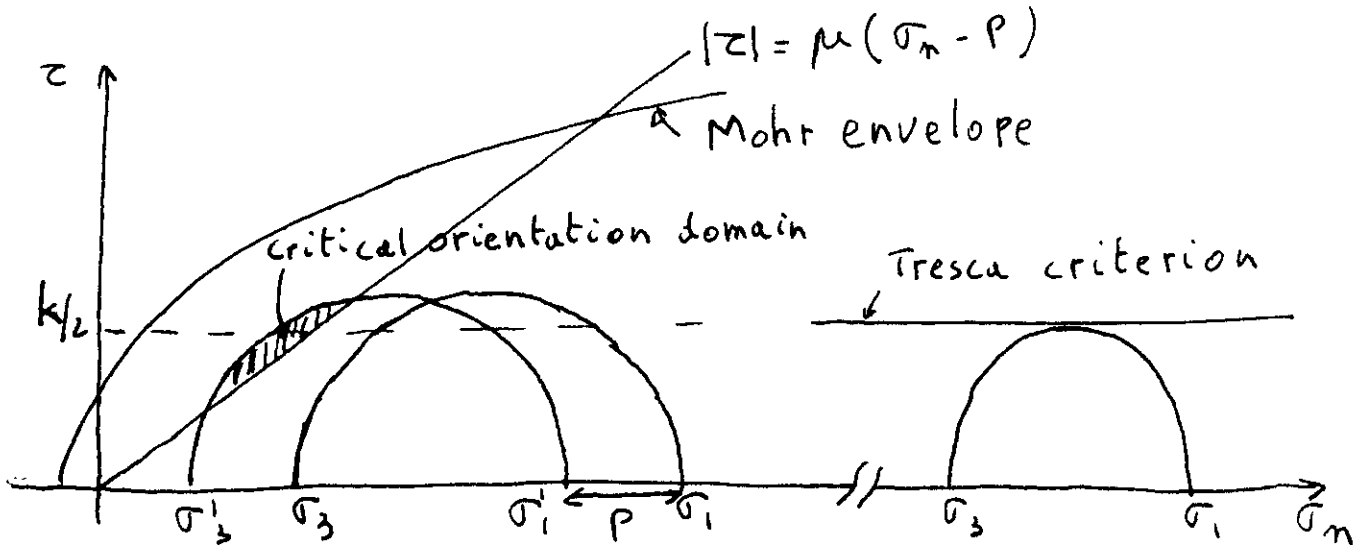

Figure 2 Description of failure conditions in a rock mass. It includes both, failure in the intact rock and failure along preexisting weakness planes as expressed in terms of effective stresses.

1.2.2 Failure along preexisting weakness planes

It is generally accepted that failure along preexisting planes is well represented by Coulomb's friction law, expressed in terms of effective stresses :

$$|\tau| = \mu(\sigma_n - P) + C_0 \qquad (10)$$

Byerlee (1978) has shown that for most rocks the friction coefficient ranges from 0.6 to 0.9. For wet rocks, most field data point out to values for the friction coefficient ranging from 0.6 to 0.8 and negligible cohesion, so that the failure along preexisting weakness planes at depths greater than a few hundred meters is well represented by Byerlee's law :

$$|\tau| = \mu(\sigma_n - P);\ 0.6 \leq \mu \leq 0.8 \qquad (11)$$

It may be noted that $|\tau|$ and σ_n are computed for the corresponding weakness plane. Hence, it is possible for the Mohr circles to intersect the line which corresponds to Byerlee's law and yet to observe stability. This is possible if there is no preexisting plane in the critical orientation domain. However, it has been argued that fractured rock masses

have a long enough tectonic history that there always exists a plane with critical orientation. Hence it is often considered that the Mohr circle representing the stress at any point in the rock mass is at most tangent to the straight line which corresponds to Byerlee's law.

Let us observe that, because sliding depends on effective stresses, planes with a great variety of orientations may slip if the local pore pressure becomes large enough, as pointed out by McKenzie (1969).

The equilibrium of rock masses is classically analyzed with a Mohr diagram as shown on figure 2. Note that failure along preexisting weakness planes is the controlling phenomenon in most cases. An important difference between the development of new shear zones and the slipping along preexisting weakness planes, is that the orientation of new shear planes may be determined from the principal stress directions, if the corresponding internal friction coefficient is known (the Mohr circle at rupture is tangent to he Mohr envelope), but this is not true for preexisting weakness planes, given the role of pore pressure.

It is concluded that seismicity occurring in the upper 15 to 20 km of the crust involves fracture planes that make an unknown angle with respect to the principal stress directions.

In the above discussion, the friction angle and the cohesion are isotropic so that, if slip occurs, it will occur in the direction of the resolved shear stress (τ) in the plane (Bott, 1959). But this direction of resolved shear stress depends on the relative orientation of the slip plane with respect to the principal directions as well as on the relative magnitude of principal stress components. This is the basic principle underlying stress determinations from a collection of fault planes solutions.

2. Inversion of double couple focal mechanisms for stress determination

2.1 data produced by Fault plane solutions

Focal mechanisms of pure shear faults (pure double couples, no significant dilatancy), yield for both nodal planes the dip and azimuth of the plane (d and a) as well as the slip direction in the plane (rake angle r of slip vector s) when it corresponds to the fault plane.

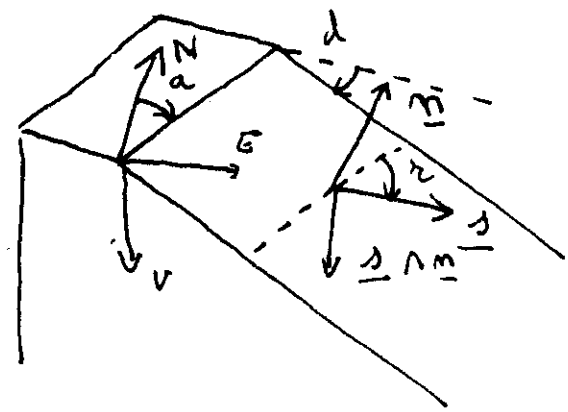

But it is impossible to identify which of the two nodal planes is the actual fault plane, if only the polarity of P waves is considered. The method proposed by Zollo and Bernard (1989, 1991) for determining focal plane solutions conducts an exhaustive search

of all possible solutions and each solution is associated with a probability. Hence solutions with 60 %, 90 % and 99 % confidence levels are determined. These confidence level domains are used then to determine the corresponding uncertainty associated with the various angles determination.

Note that when enough three components stations are being used, the radiation pattern for S waves help identify the fault plane. In the following, it is considered that the fault plane has not been identified so that both nodal planes are equally likely to be the fault plane. Hence for each focal mechanism, a set of 12 values is identified : (a_1, d_1, r_1, εa_1, εd_1, εr_1 , a_2, d_2, r_2, εa_2, εd_2 , εr_2).

It is customary to identify P and T axis with focal mechanisms. These are inclined 45° with respect to the nodal planes. It has been proposed sometimes to associate these axes respectively with the maximum and minimum principal stress direction. It should be noted here that, only when failure occurs according to the Tresca failure criterion (i.e. for very deep earthquakes) is this proposition valid. Hence this proposition is erroneous for most seismic events of the upper crust since either these correspond to the reactivation of preexisting weakness planes, or the newly formed shear zones are inclined by less than 45° with respect to the maximum principal stress orientation.

2.2 Determination of the regional stress field from focal mechanisms

Gephart and Forsyth's approximate method

The method (Gephart and Forsyth, 1984) is based on the following assumptions :

1. Slip occurs parallel to the direction of the resolved shear stress;

2. All seismic events are distant enough from each other that the stress perturbation induced by each event does not alter the stress field for other events;

3. The original stress field is uniform within the volume sampled by the various events.

Validity of hypothesis 1 implies that the shear strength in all planes is isotropic while hypothesis 3 implies that events are not too distant from each other so that stress gradients may be neglected. This has implication for the depth ranges of events considered for a single inversion.

Because focal mechanisms yield only the direction (and sense) of slip and not the magnitude, the stress tensor cannot be fully determined. Only four parameters are determined : the three Euler angles and an aspect ratio R defined as :

$$R = (\sigma_2 - \sigma_1) / (\sigma_3 - \sigma_1) \qquad (12)$$

So that $0 \leq R \leq 1$. Indeed, the stress at any point may be rewritten :

$$\sigma = \sigma_1 \mathbf{I} + (\sigma_3 - \sigma_1) \mathbf{T} \qquad (13)$$

with :

$$(T) = \begin{pmatrix} 0 & 0 & 0 \\ 0 & R & 0 \\ 0 & 0 & 1 \end{pmatrix}$$

so that $\underset{\sim}{T}$ is characterized by 4 parameters (ψ , φ , θ , R). Note that ψ ranges from 0 to 360 °, while the range for φ is 90° and that for θ is 180°. Hence, the complete set of solutions for $\underset{\sim}{T}$ is fairly limited and it can be fully explored with a grid search method. The solution is that which fits best the collection of focal mechanisms.

Let us determine now the condition for $\underset{\sim}{T}$ to be consistent with a given focal mechanism, i.e. the tensor $\underset{\sim}{T}$ for which the resolved shear stress τ_0 on a fault plane is parallel to the observed slip vector s. First it will be noted that $\tau_0 . s > 0$.

We consider now two frames of reference : the first one (R) is associated with the eigen vectors of $\underset{\sim}{T}$. The second one (R') is associated with the fault plane ($\mathbf{n}$, $\mathbf{s} \wedge \mathbf{n}$, $\mathbf{s}$).

Let β be the orthogonal tensor which rotates R to R'. It may be observed that in R', the stress component σ'_{12} is null. Hence, given the definition of R, we obtain :

$$\sigma'_{12} = \sigma_1 \beta_{11} \beta_{21} + \sigma_2 \beta_{12} \beta_{22} + \sigma_3 \beta_{13} \beta_{23} = 0 \qquad (14)$$

so that

$$R = (\sigma_2 - \sigma_1) / (\sigma_3 - \sigma_1) = - \beta_{13} \beta_{23} / \beta_{12} \beta_{22} \qquad (15)$$

For a given fault plane defined by the triplet (a, d, r), and given a tensor $\underset{\sim}{T}$ with Euler angles ψ , φ , θ, there is a unique value of R which fits the direction of slip in the corresponding plane. This is taken to advantage for identifying both the best solution $\underset{\sim}{T_s}$ for the given set of focal mechanisms and its domains of confidence level.

The idea is to explore the set of possible solutions and to identify that which fits best observations, namely the tensor, which yields resolved shear stress directions closest to observed slip vector directions. The problem is three folds :

1. Identify for each focal mechanism which nodal plane is the fault plane;

2. For all focal mechanisms define a measure of their misfit with a given tensor $\underset{\sim}{T}$.

3. Identify the best solution and associated confidence level domains.

The measure of misfit and the identification of fault planes

It has been proposed sometimes to characterize the misfit between a given fault plane and a given tensor $\underset{\sim}{T}$ by the angle between the shear stress resolved on that plane and the observed slip vector. But this assumes that the fault plane is known exactly while in reality this is not the case as mentioned here above. Gephart and Forsyth (1984) proposed to consider as measure of misfit, for any given plane, the smallest rotation which brings s parallel to the resolved shear stress in the plane (τ). They observe that this misfit is a well behaved function so that it suffices to consider only three rotations axis, namely $\mathbf{n}$, $\mathbf{s} \wedge \mathbf{n}$ and $\mathbf{s}$.

The rotation angles are computed according to equation (15) once R' has been replaced by the frame of reference R" that corresponds to the rotated R' :

$$\underset{\sim}{\mathbf{R}}'' = \underset{\sim}{\alpha}(i)\ \underset{\sim}{\mathbf{R}}' \qquad (16)$$

where $\underset{\sim}{\alpha}(i)$ is the orthogonal tensor corresponding to rotations about $\mathbf{n}$, $\mathbf{s} \wedge \mathbf{n}$ or $\mathbf{s}$. The angles of rotation are given here below :

Table 1

Expressions for rotations about axes of fault plane geometry.

Rotation axis	Algorithm	Period
$\mathbf{n}$	$\theta = -\tan^{-1}\left[\dfrac{RB_{12}B_{22} + B_{13}B_{23}}{RB_{12}B_{32} + B_{13}B_{33}}\right]$	Π
$\mathbf{s} \wedge \mathbf{n}$	$\theta = \tan^{-1}\left[\dfrac{RB_{12}B_{22} + B_{23}B_{13}}{RB_{22}B_{32} + B_{23}B_{33}}\right]$	Π
$\mathbf{s}$	$\theta = \frac{1}{2}\tan^{-1}\left(\frac{2}{k}\right)$ where $k = \dfrac{R(B_{12}^2 - B_{22}^2) + B_{13}^2 - B_{23}^2}{RB_{12}B_{22} + B_{13}B_{23}}$	$\frac{\Pi}{2}$

For any given $\underset{\sim}{\mathbf{T}}$ and any focal mechanism six rotation angles are computed : 3 for the first nodal plane and 3 for the second nodal plane. The nodal plane which yields the smallest rotation is chosen as fault plane and the measure of misfit for the corresponding plane is the smallest rotation. Hence, the misfit value associated to any given $\underset{\sim}{\mathbf{T}}^{(i)}$, is the sum of the misfit measures for all focal mechanisms. It is given by :

$$m_i = \sum_{k=1}^{N} \min(x_k^l, l = 1,6) \qquad (17)$$

where x_k^l is the l^{th} rotation for focal plane solution k.

The solution is the tensor for which m_i is minimum. The corresponding value for the misfit is noted m_{min}. Here, the L_1 norm has been chosen rather than a least squares norm. Indeed, the choice of the nodal plane as fault plane is either right or wrong so that the error associated with the rotation angle determination does not obey a Gaussian law.

It has been proposed (Julien and Cornet, 1987) to introduce weight factors in the misfit function by dividing the minimum rotation angle by the uncertainty on the orientation of the nodal plane as defined by the focal mechanism determination. Also, when the rotation angle is larger than the solid angle that corresponds to the 90 % confidence level for the fault plane orientation, the focal mechanism is considered to be heterogeneous with the corresponding tensor. Then the quality of the solution is defined not only by the misfit value but also by the number of inconsistent data. Indeed, it may be argued that a solution which requires very small rotation angles but is heterogeneous with more than 50 % of the data is not satisfactory.

Let m_{50} and m_{90} be the values for the bounds of the misfit function which characterize respectively the 50 % and the 90 % confidence levels. For the L1 norm, Parker and McNutt (1980) have showed that these bounds may be defined with respect to the best solution as :

$$m_{90} = \{ [1.645(\pi/2\text{-}1)^{1/2} N^{1/2} + N] / (N\text{-}k) \} m_{min} \quad (18)$$

and

$$m_{50} = \{ [0.676(\pi/2\text{-}1)^{1/2} N^{1/2} + N] / (N\text{-}k) \} m_{min} \quad (19)$$

where k is the number of parameters in the model (here k= 4) and N is the total number of focal mechanisms.

Hence, all solutions for which the misfit m_i is found to be smaller than either m_{50} or m_{90} are plotted on a stereo net. The contour plot of these solutions identifies the 50 and 90 % confidence levels.

Once the approximate solution and its associated confidence levels are known, fault planes have been identified for each focal mechanism. Cornet and Julien (1987) have proposed a method based on a least squares method for identifying the best solution, once the approximate solution is known. However, experience has shown that this refining of the solution is not necessary for the solution remains within the 50 % confidence level domain. It suffices to run the approximate method with a finer grid restricted to the 90 % confidence level domain.

Stress determination in large volumes

When inverting for tensor $\underset{\sim}{T}$, it is assumed that the stress is uniform throughout the volume sampled by the various focal mechanisms. But, if only because of gravity, it is known that the stresses vary with depth and possibly also laterally. Hence the question arises as to the validity of this hypothesis.

Interestingly, most stress field measurements have shown that the stress varies linearly with depth. Further, as shown by Mc Garr (1980), when there is no lateral stress variation, the vertical direction is principal. Hence, in many a situation, the stress field may be written :

$$\underset{\sim}{\sigma}(x_3) = \underset{\sim}{\sigma}(x_c) + (x_3 - x_{3c}) \underset{\sim}{\alpha} \quad (20)$$

where $\underset{\sim}{\sigma}(x_3)$ is the stress at depth x_3, $\underset{\sim}{\sigma}(x_c)$ is the stress at the reference depth x_c (6 independent components) and $\underset{\sim}{\alpha}$ is the vertical stress gradient (six independent components which reduce to 4 independent components, namely the three eigen values and the orientation of one of the horizontal eigen vectors, when there is no lateral stress variation).

Equation (20) has revealed very useful for interpreting direct stress measurements in boreholes. Indeed, it is usually found that close to ground surface many perturbations of the stress field exist whichmay be lumped as a fixed term for a given depth interval. But, as depth gets larger, the gradient term becomes more significant so that, when depth gets greater than 1 km, it may be considered that the vertical stress gradient dominates the stress field and that the constant term may be neglected. When this is the case, then the stress field can again be simplified so as to be characterized by only four parameters, namely the three Euler angles and the R aspect ratio. However, now, R describes the aspect ratio of the vertical stress gradient and not the complete stress tensor at depth z ;

$$R = (\alpha_2 - \alpha_1) / (\alpha_3 - \alpha_1) \quad (21)$$

Given that usually the rock mass density α_3, is rather well known, the determination of the ratio R provides constraints on the relative variations of both horizontal stress components when there is no lateral stress variation.

This observation opens the door now to a possibility of extrapolating borehole stress determinations, which are usually conducted in the upper kilometer of the crust, down to depths of natural microseismic activity. This is possible provided the stress gradient is continuous and stable for the complete depth interval. Hence the mapping of the complete stress field at the scale of the crust may become realistic, when combining borehole data and focal mechanisms of natural seismicity.

2.3 Integrating focal plane solutions with other data for a complete stress determination

A great diversity of methods has been developed for determining the stress field in the vicinity of boreholes (Cornet, 1993). One of the most efficient such method is hydraulic fracturing and its generalization, the so-called Hydraulic Test on Preexisting Fractures (HTPF) method. The HTPF method basically provides measurements of the normal stress supported by fractures of known orientation (Cornet, 1993).

It has been applied to investigate the validity of stress determination from focal mechanisms of microseismic events induced by large fluid injections. In this example, microseismic events are within the same volume as that in which the stress measurements have been conducted. This is presented in the two following papers. In the first one, the method for integrating HTPF results with focal mechanisms is presented. In the second paper, results from the induced seimicity experiment are presented together with a brief overview of the HTPF method. The joint inversion helps characterize the stress field as well as the pore pressure field in the rock mass. In addition, it points out the fact that natural faults are zones of local stress heterogeneity so that microseismic events which occur within major fault zones may not be representative of the regional stress away from the fault. Orders of magnitudes for the stress heterogeneity are presented.

References

Bott B., 1959, The mechanics of oblique slip faulting, Geol. Mag., vol 96, nb 2, pp 109-117

Byerlee J., 1978, Friction of rocks, Pure and App. Geophys., vol 116, pp 615-626

Cornet F.H.; 1993; Stresses in Rock and Rock Masses; Comprehensive Rock Engineering (Hudson ed.), vol. 3, ch. 12, pp 297-327, Pergammon Press Oxford.

Cornet F.H.; 1993; The HTPF and the Integrated stress determination methods; Comprehensive Rock Engineering (Hudson ed.); Vol 3, ch. 15, pp 413-432 Pergammon Press, Oxford.

Gephart J.W. and D.W. Forsyth, 1984, An improved method for determining the regional stress tensor using earthquake focal mechanism data : application to the SanFernando earthquake sequence, jou. Geophys. Res., vol 89, nb b11, pp 9305-9320

Julien Ph. and F.H. Cornet; 1987; Stress Determination from Aftershocks of the Campania-Lucania Earthquake of November 23, 1980; Ann. Geoph., vol. 5b, no 3, pp 289-300.

Mc Garr A., 1980, Some constraints on levels of shear stress in the crust from observation and theory, Jou. Geophys. Res., vol. 85, p 6231

McKenzie D.P., 1969, The relation between fault plane solutions for earthquakes and the directions of principal stresses, Bull. Seism. Soc. Am., vol 59, nb 2, pp 591-601

Parker R. L. and M.K. McNutt; 1980, Statistics or the one norm misfit measure, Jou. Geophys. Res., vol 85, p 4489.

Zollo A and P. Bernard; 1989, S-wave polarization inversion of the 15 October 1979, 23:19 Imperial Valley aftershock : evidence for anisotropy and a single source mechanisms, Geophys. Res. Let., vol 16, pp 1047-1050

Zollo A and P. Bernard, 1991, How does an asperity break/new elements from the wave form inversion of accelerograms for the 2319 UT, October 15, 1979 Imperial valley after shock, Geophys. Res. Let. Vol 23, pp 111-126

GEOPHYSICAL RESEARCH LETTERS, VOL. 21, NO. 24, PAGES 2645-2648, DECEMBER 1, 1994

Integrated stress determination by joint inversion of hydraulic tests and focal mechanisms

J. M. Yin and F. H. Cornet
Département de Sismologie, Institut de Physique du Globe de Paris

Abstract. An inversion method, based on a genetic algorithm, is proposed for interpreting jointly various kinds of stress data in order to overcome the limitation, in number and quality, of each data set. The method has been applied to results from hydraulic tests in boreholes and to focal mechanisms of induced seismicity observed within the same depth interval. The regional stress field is described by two symmetrical tensors. The first one represents the stress at a given depth and the second one the vertical stress gradient. Results indicate that one of the principal directions is vertical. They are consistent with all but one of the hydraulic tests considered in the inversion and with about 70% of the focal mechanisms. This inversion confirms previous results suggesting that, for the scale of these induced microseismic events, the regional stress field cannot be determined solely from an inversion of the fault plane solutions.

Introduction

Many techniques have been developed for determining the natural stress field at depth but none of them yield directly all the stress components. Further, because these techniques seldom provide means to assess the precision of the determination, investigators often try to compare results obtained by more than one technique (Barton et al., 1988; Haimson et al., 1989).

We present in this paper a method for inverting jointly hydraulic test measurements and focal mechanisms of induced microseismicity obtained within the same depth interval.

Data and separate determinations

The granite test site at Le Mayet de Montagne, in central France, has been developed for conducting large scale in-situ experiments on forced water circulation. The stress field was investigated by the Hydraulic Tests on Preexisting Fractures (HTPF) method which is based on measurements of the normal stress supported by various preexisting fractures of known orientation (Cornet and Valette, 1984). Prior to the water circulation experiments, 18 HTPF measurements were conducted in various boreholes at the site. They have been successfully inverted with a stress field model which assumes a vertical principal direction throughout the volume of interest and a linear variation with depth. The results are consistent with the regional stress field determined in neighbouring sites (Cornet and Burlet, 1992). Two years after the water circulation tests had been completed, another 13 HTPF measurements were conducted. They are quite consistent with the stress field initially determined except for two tests located near one of the most hydraulically conductive zones (Scotti and Cornet, 1994).

Copyright 1994 by the American Geophysical Union.

Paper number 94GL02584
0094-8534/94/94GL-02584$03.00

The water injections induced some microseismicity which was monitored with a network of fifteen 3-D seismic stations (Cornet and Julien, 1989; Cornet et al., 1992). About 200 events were recorded and located with more than 12 P waves and 10 S waves arrivals. Out of these, 87 events yield well constrained fault plane solutions characteristic of shear slip (i.e. two nodal planes with standard deviation generally less than 10° on their strike and dip determination). For the remaining events, only one nodal plane was determined because of insufficient or poor spatial coverage of polarity measurements.

These focal mechanisms were separated into two groups corresponding respectively to the 70-hour initial injection and to the large scale circulation test which lasted four months in total. For both sets of focal mechanisms, the regional stress field has been determined using Julien and Cornet's inversion method (1987) which is derived from that initially proposed by Gephart and Forsyth (1984). The slip vector in the fault plane is assumed to be parallel to the resolved shear stress supported by the plane. The principal directions and a shape factor R ($(\sigma_2-\sigma_1)/(\sigma_3-\sigma_1)$) are supposed to be uniform throughout the volume considered. The inversion of the focal mechanisms obtained during the preliminary injection yields a solution significantly different from that obtained with the HTPF data (Cornet and Julien, 1989). Scotti and Cornet (1994) have suggested that some microseismic events induced by this injection were associated with local stress heterogeneities. Indeed, results obtained from the microseismic events observed during the subsequent large scale injection revealed nearly consistent with the HTPF solution (Cornet et al., 1992; Yin, 1994). However, these results are only fairly constrained. Also, for the various depth intervals, the maximum horizontal principal stress direction exhibits a systematic clockwise rotation equal to about 30° in comparison with the HTPF solution. Such discrepancy may be due to the parameterization difference between the two methods. In order to alleviate the hypotheses associated with each determination technique taken alone, a joint inversion has been attempted.

Joint inversion method

Parameterization. Because of the absence of strong topography and because of the homogeneity of the granite, we adopt a stress model with linear vertical variation but with no variation in horizontal directions. No assumption is made concerning the verticality of one principal stress, unlike in the previous model chosen for fitting only the HTPF data. Thus ten parameters suffice to represent the stress field $\mathcal{O}(z)$: $\mathcal{O}(z) = S_{z_0} + (z - z_0)\mathcal{A}$. Here S_{z_0} is the stress tensor at a given depth z_0, $\mathcal{A}$ is the vertical gradient tensor. S_{z_0} is characterized by three principal values (S_1, S_2 and S_3) and three Euler angles (λ_1, λ_2 and λ_3). From equilibrium conditions it is found that the horizontal uniformity assumption implies that the vertical direction is principal for $\mathcal{A}$. So $\mathcal{A}$ is characterized by four parameters: three principal values (α_1, α_2 and α_3) and the azimuth (η) of the maximum horizontal principal component (α_1).

Inversion strategy. Our objective is to search for the optimal solution and its confidence limit. The inversion of

focal mechanisms is a non-linear problem and this makes the joint inversion also non-linear, so that an extensive exploration of the model space is required. The minimum absolute criterion (ℓ_1-norm) is adopted for the measurement of misfit. Given the diversity of data considered in the inversion, this criterion has been shown to exhibit a stronger robustness than the least squares criterion (e.g. Tarantola, 1987).

Misfit function. A dimensionless misfit function is defined to deal with different data sets. Let Φ_h be the measure of misfit associated with the N HTPF data:

$$\Phi_h = \sum_{i=1}^{N} |\sigma_{no}^i - \sigma_{np}^i|/\delta_h^i \quad (1)$$

where σ_{no}^i is the observed normal stress for the ith HTPF datum, σ_{np}^i is the predicted one, δ_h^i is the sum of the standard deviation associated with σ_{no}^i and another term representing the uncertainty on the normal stress because of the error associated with the identification of the normal to the corresponding fracture plane.

For the jth focal mechanism, let χ^j be the minimum rotation angle that brings the observed slip vector into coincidence with the resolved shear direction as computed for the currently tested stress model. Following Gephart and Forsyth's approximate method (1984), the minimum angle is searched among three orthogonal rotations (one about the slip vector s, one about the normal to the nodal plane n and one about the axis coaxial with n×s) for each of the two nodal planes. The fault plane is chosen to be the nodal plane which requires the smallest rotation. The measure of misfit Φ_f associated with M focal mechanisms is:

$$\Phi_f = \sum_{j=1}^{M} |\chi^j|/\delta_f^j \quad (2)$$

δ_f^j is the standard deviation associated with the evaluation of the nodal plane geometry.

Because the number of data of one kind is generally different from that of the other kind and also, because the error range is fairly different for the two data sets, weighting factors for the two measures of misfit are introduced in the global misfit function. First, the two sets of data are inverted separately so as to estimate, for each data set, the largest number of data (N_c^{max} and M_c^{max}) consistent with the stress model as well as the corresponding minimum measure of misfit (Φ_h^{min} and Φ_f^{min}) as defined by (1) and (2). The criterion for consistency is defined by assuming that errors are normally distributed and by rejecting data which do not belong to the 99% confidence level. Then, we define the measure of global misfit so as to give an equal weight to each data set by normalizing the two measures of misfit separately:

$$\Phi_s = \frac{1}{2}\frac{N_c^{max}}{N_c}\frac{\Phi_h}{\Phi_h^{min}} + \frac{1}{2}\frac{M_c^{max}}{M_c}\frac{\Phi_f}{\Phi_f^{min}} \quad (3)$$

N_c and M_c are the number of data which are consistent with the currently tested model.

It may happen that one type of data, such as the focal mechanisms in our application, does not constrain all the parameters of the stress model. An approximate partial model is considered sufficient to make a reasonable estimation of the corresponding weighting factor. For example, the stress model has been reduced to seven parameters for the evaluation of the weighting factor associated with the focal mechanisms, as is discussed later.

Inversion procedure. A genetic algorithm (GA) is used first for estimating Φ_h^{min}, Φ_f^{min}, N_c^{max} and M_c^{max}, then for searching the optimal model corresponding to Φ_s^{min}. The classic Monte Carlo (MC) technique is applied to find a random sample of models for establishing the corresponding 95% confidence level according to the ℓ_1-norm criterion. GA is a very efficient optimization technique which has been recently introduced in geophysical inverse problems guided MC (e.g., Gallagher et al., 1991). However, the sic MC method has been chosen for error analysis bec to our knowledge, the practical use of GA for this pu has not yet been published. Some essentials of GA a called here for presenting the particular adaptation us this paper. After discretizing the parameters, a popul of Q models are generated at random and coded in nary strings. GA optimizes the models by strings ma lation through a 3-step iteration (or generation): repro tion, cross-over and mutation. (1) The reproduction selects the models from those of the previous iteration misfit dependent probability Pr(i), chosen as a linear f $Pr(i) = [\Phi_s^{max} - \Phi_s(i)]/[Q(\Phi_s^{max} - \Phi_s^{avg})](i = 1,...$ where Φ_s^{max} and Φ_s^{avg} are respectively the maximum the mean value of $\Phi_s(i)$. This choice of Pr has a wide di bution; thus it avoids favoring excessively the better mo Yet, the best model is forced to be selected at least o (2) The cross-over step creates new models by transpo one of two string segments (cut at a randomly chosen sition) between randomly paired models with a probab Pc. Large Pc values are chosen (Pc>0.8) for speeding up ploitation of the model information contained in the in population. (3) The mutation step perturbs the string with a small probability Pm (Pm < 1/10000, as propo by Holland, 1992). This step is designed for introduc some diversity into the model population. Pm is kept sr in order to avoid a degeneracy of GA into a conventic MC.

Results from Le Mayet de Montagne

The complete data involve 31 HTPF measureme within the 50-780 m depth interval and 87 focal mec nisms within the 300-950m depth interval. Seven HT data in the upper 200m and another two near 780m are taken into account because of the absence of seismic data the shallowest depth range on one hand and, on the otl hand, the existence of a greatly altered zone around 780 well documented by various borehole logs (Scotti and C net, 1994). Thus only 22 HTPF data are involved in t joint determination. In contrast, all the focal mechanis are considered because no a priori information is availal for examining their consistency with the global stress fie

Searching the optimal model with GA. The discretiz tion interval for the angular parameters is 2° or 3° (coveri the full range of 180°), that for stress magnitudes is 0.2 M in a range of 13 MPa and that for stress gradients is 0.00 MPa/m in a range of 0.02 MPa/m. All ranges are center around the corresponding values of previous regional stre field determination (Cornet and Burlet, 1992). The specif weight of overburden (α_3) is fixed at 0.0265 MPa/m. Th leaves nine parameters to be determined. Our GA impl mentation uses a 6 bits coding for each parameter so th each parameter may take 63 possible values. Each model nine parameters forms a string of 54 bits.

The GA is first applied only to the HTPF data. Fig.1(a shows the mean and the minimum misfit evolution for thre different model populations. For each of them, the minimu misfit is obtained as early as the 200th iteration althoug the mean value for larger populations may decrease mo slowly. The corresponding stress model is found to be th same as that obtained by a least squares method (Corne and Valette, 1984) for the two larger populations.

In the case of focal mechanisms, there is no informatio constraining the absolute stress magnitudes, so the GA i applied by fixing the vertical stress magnitude (not nece ssarily being a principal stress) and another eigenvalue, i.e only seven parameters are searched. Fig.1(b) shows a per formance of GA similar to that observed for the HTPF data

These two analyses yield: Φ_h^{min}=13.0, N_c^{max}=22

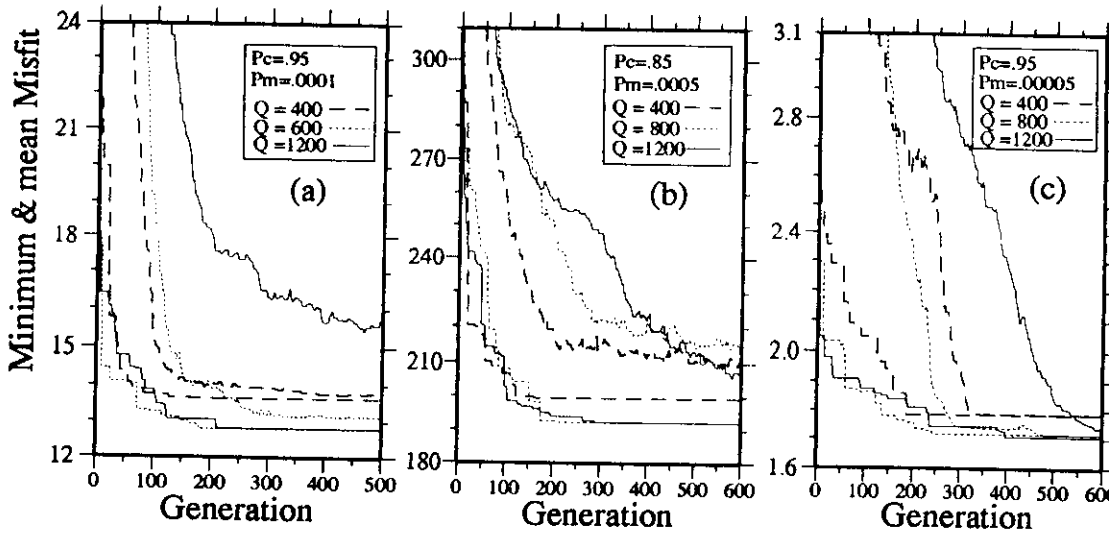

Figure 1 : Performance evolution and comparison of GA used in the various inversions: (a) HTPF data alone, (b) focal mechanisms alone and (c) joint inversion. In each inversion, GA was run with three different population size Q, with the crossover probability Pc and mutation probability Pm. Each run is displayed by two curves in the same style, the upper one represents the average misfit while the lower one represents the minimum misfit.

Φ_s^{min}=192.0 and M_c^{max}=72. The joint inversion by GA brings again a performance similar to the two previous ones as illustrated by Fig.1(c). The optimal model is chosen as that for which the minimum misfit has been found (Φ_s^{min} =1.71): S_1 = 20, S_2 = 19.4, S_3 = 11.8MPa, $\lambda_1 = -34^0$, $\lambda_2 = 86^0$, $\lambda_3 = 88^0$ (z_0 = 750m, λ_1 and λ_2 are respectively the strike and dip of S_1 axis, λ_3 is the angle between S_2 axis and the horizontal line in the plane perpendicular to S_1); α_1 = .0258, α_2 = .0146, α_3 = .0265MPa/m, $\eta = 162^0$ (azimuth of α_1). This model fits 21 HTPF data and 63 focal mechanisms (Nc=21 and Mc=63 in eq.(3)).

Note that for all three cases, the minimum population size which allows identification of the optimal model lies around 600~800.

Model space exploration by MC. 30 million models generated at random, within a regular grid twice as coarse as that used for the GA, have been tested. 430 models for which the misfit Φ_s is less than the 95% confidence limit $\Phi_s^{95\%}$ (=2.13) are retained. They are used to establish the 95% confidence level of the optimal stress model obtained from GA (Fig.2a). They are quite concentrated around the optimal solution. These models explain in average 95% of the HTPF data and 70% of the focal mechanisms. For the other 30% of the focal mechanisms, the mean rotation angle exceeds either 18° or three times the corresponding standard deviation (eq.2) for more than 50% of these 430 models.

During this exploration we have also retained some 60000 models fitting only the HTPF data by the same confidence limit criterion. A sample of 3000 of them is used to draw the 95% confidence level of the optimal HTPF solution (Fig.2b).

A comparison between Fig.2a and Fig.2b brings the fol-

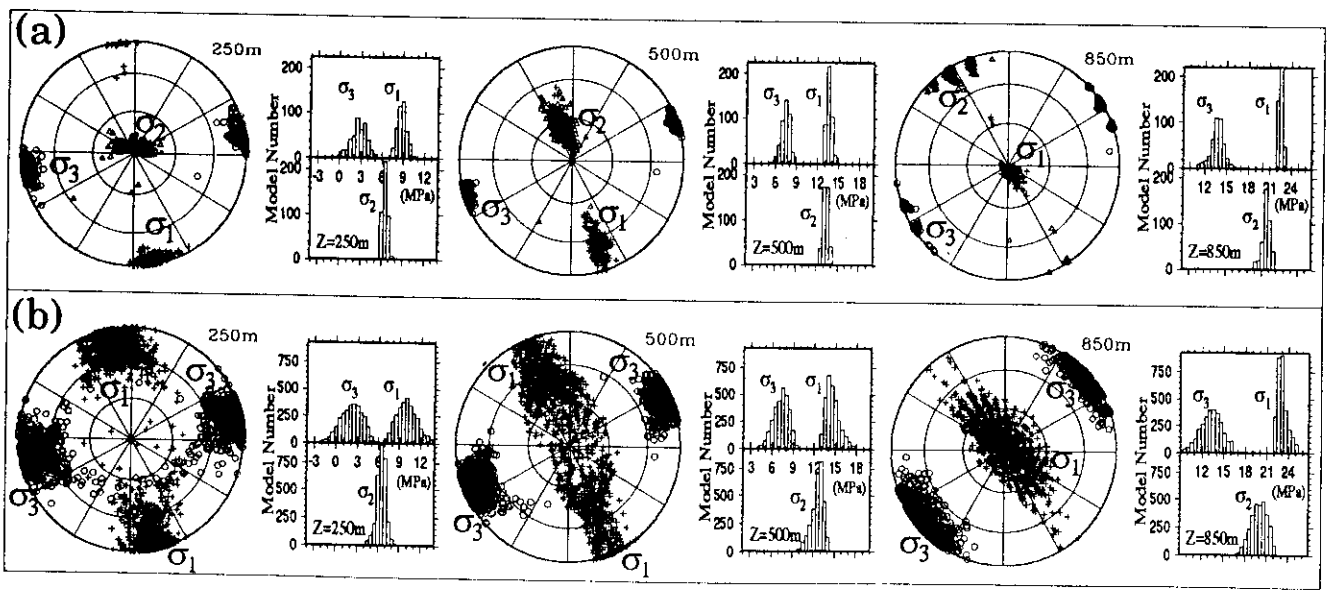

Figure 2 : (a) Lower hemisphere equal area projection of principal stress axes and Histogram of principal stress magnitudes, for various depths, for the joint inversion. (b) Results obtained by inversion of the sole HTPF data. Same notations as for (a), but the σ_2 axes are not shown.

lowing observations: The model space is fully explored as shown in Fig.2a, so the retained models of joint inversion are representative of all the possible solutions, and the confidence zonation is significant. The joint results are similar in magnitudes as well as in principal orientation to those obtained with the sole HTPF data, but their certainty increases clearly. The major horizontal stress direction of the joint results shows a clockwise rotation of 5 to 10° in comparison with the HTPF results. Such a difference has the same tendency as already mentioned for the results obtained by inversion of the focal mechanisms taken alone and with a uniform stress model of four parameters. However, the difference with respect to this former solution is larger than 30° (see Table 1). This implies that the seismic data have effectively contributed to the joint result but their role is not as important as that of the HTPF data. However, it has been statistically verified that the weight of the focal mechanisms is slightly greater than that of HTPF data (the mean ratio of the second term over the first one in eq.(3) is equal to about 1.16). This paradox can be explained by the fact that the seismic data are less consistent than the HTPF data in term of the regional stress field. The earthquakes are located in or near the hydraulically conductive fractured zones which often coincide with altered zones, while the borehole intervals of the HTPF tests were intentionally selected in intact rock. This proposition is supported by the observation that the inversion of various sets of HTPF data has consistently led to similar results while the four parameter inversion of focal mechanisms observed during the initial injection tests yields results significantly different from those derived from the focal mechanisms observed during the large scale injections.

It can be concluded that the discrepancy between the results obtained by previous separate inversions disappears in the joint inversion. However, some focal mechanisms remain inconsistent with the joint results (up to 30% of the whole). This implies first, that when only focal mechanisms are used for the stress determination, those which are inconsistent with the regional stress field influence significantly the output of the inversion. Thus for the scale of these events (slip zones of the order of 1 m^2), the regional stress field cannot be determined by the sole inversion of focal mechanisms of induced microseismicity. Further, the joint inversion provides means to identify those focal mechanisms which are heterogeneous with the regional stress field and this may reveal powerful for identifying the main zones of alteration.

Table 1. Azimuth of the maximum horizontal stress

Results type	Z=450-550m	Z=750-900m
HTPF (1)	NE 155±20°	NE 140 ± 23°
Focal mech.(2)	NE 30±20°	NE 170 ± 18°
Joint method	NE 160± 8°	NE 146 ± 15°

(1) Same for Cornet et al.(1992) and the present study.
(2) From Cornet et al. (1992).

Conclusion

A joint inversion method has been proposed for integrating two or more kinds of data gathered in the same rock mass for the sake of determining the regional stress field. It includes an optimal model search using a genetic algorithm and the error analysis by the classic Monte Carlo technique. Successful application of this method to HTPF measurements and focal mechanisms of induced seismicity illustrates the improvement that the joint inversion technique brings as compared to the results obtained with the separate determinations.

The results of the joint inversion has demonstrated that the concept of the regional stress field is valid for large volumes of rock (about 1 km^3). It also outlines the existence of focal mechanisms which are not consistent with the reg stress field. These inconsistent focal mechanisms shoul veal helpful for identifying zones of stress heterogeneit

Acknowledgements. This work was funded by Centre Nat de la Recherche Scientifique (PIRSEM) and by the Euro Economic Communities (DG XII). The help of B. Bert, L. tel and G. Rozières for the data acquisition process is great acknowledged.

References

Barton C.A., M.D. Zoback and K.L. Burns, In situ st orientation and magnitude at the Fenton Hill geother site, New Mexico, determined from wellbore breako *Geophys. Res. Lett.*, 15, No.5, 467-470, 1988.

Cornet F.H. and Burlet D., Stress field determination France by hydraulic tests in boreholes. *J. Geop Res.*, 97, B8, 11,829-11,849, 1992.

Cornet F.H. and Julien Ph., Stress determination from draulic tests data and focal mechanisms of induced s micity.*Intern. J. Rock Mech. Min. Sci. & Geom Abs.*, 26, 235-248, 1989.

Cornet F.H. and B. Valette, In-situ stress determinati from hydraulic injection test data. *J. Geophys. R* 89, B13, 11,527-11,537, 1984.

Cornet F.H., J.M. Yin and L. Martel, Stress heterogen and flow path in a granite rock mass, in *Fractured jointed rock masses* (L. Myer ed.), vol.1, 80-87, Lawre Berkeley Laboratory report LBL - 32379, 1992.

Gallagher K., M. Sambridge and G. Drijkoningen, Gen Algorithms: an evolution on Monte Carlo methods strongly non-linear geophysical optimization proble *Geophys. Res. Lett.*, 18, No.12, 2177-2180, 1991.

Gephart J.W. and D.W. Forsyth, An improved method determining the regional stress tensor using earthqu focal mechanism data: application to the San Fernan earthquake sequence. *J. Geophys. Res.*, 89, 9305-93 1984.

Haimson B.C., L.W. Tunbridge, M.Y. Lee and C.M. Co ing, Measurement of rock stress using the hydraulic fr turing method in Cornwall, U.K.—Part II. Data red tion and stress Calculation, *Int. J. Rock Mech. Min. S* 26, 6, 361-372, 1989.

Holland J.H. Genetic algorithms. *Scientific American*, J 1992, 44-50, 1992.

Julien Ph. and F.H. Cornet, Stress determination from tershocks of the Campania-Lucania earthquake of Nove ber 23, 1980. *Ann. Geophys.*, 5, No.3, 289-300, 1987.

Scotti O. and F.H. Cornet, In situ evidence for fluid induc aseismic slip event along fault zones, *Int. J. Rock Me Min. Sci.* 31, 347-358, 1994.

Tarantola A, Inverse problem theory: Methods for data f ting and model parameter estimation, Elsevier, 1987.

Yin J.M., Détermination du champ de contrainte region à partir des tests hydrauliques et des mécanismes foyer de microséismes induits, Ph.D. thesis of Universi Paris 7, 1994.

F.C. Cornet and J.M. Yin, Sismologie, Institut de Physiq du Globe de Paris, 4 Place Jussieu, 75252 Paris, France.

(Received April 27, 1994; revised August 29, 1994; accepted September 13, 1994.)

PAGEOPH, Vol. 145, Nos. 3/4 (1995) 0033-4553/95/040677-24$1.50 + 0.20/0
© 1995 Birkhäuser Verlag, Basel

Analysis of Induced Seismicity for Stress Field Determination and Pore Pressure Mapping

F. H. CORNET[1] and YIN JIANMIN[1]

Abstract—The focal mechanisms of some one hundred microseismic events induced by various water injections have been determined. Within the same depth interval, numerous stress measurements have been conducted with the HTPF method. When inverted simultaneously, the HTPF data and the focal plane solutions help determine the complete stress field in a fairly large volume of rock (about 15×10^6 m^3). These results demonstrate that hydraulically conductive fault zones are associated with local stress heterogeneities. Some of these stress heterogeneities correspond to local stress concentrations with principal stress magnitudes much larger than those of the regional stress field. They preclude the determination of the regional stress field from the sole inversion of focal mechanisms. In addition to determining the regional stress field, the integrated inversion of focal mechanisms and HTPF data help identify the fault plane for each of the focal mechanisms. These slip motions have been demonstrated to be consistent with Terzaghi's effective stress principle and a Coulomb friction law with a friction coefficient ranging from 0.65 to 0.9. This has been used for mapping the pore pressure in the rock mass. This mapping shows that induced seismicity does not outline zones of high flow rate but only zones of high pore pressure. For one fault zone where no significant flow has been observed, the local pore pressure has been found to be larger than the regional minimum principal stress but no hydraulic fracturing has been detected there.

Key words: Induced seismicity, stress determination, stress heterogeneity, fluid flow, fault morphology.

1. Introduction

The injection of water in a fractured rock mass generates some seismicity when the injection pressure becomes large enough (e.g., PEARSON, 1981; NIITSUMA *et al.*, 1982; CORNET *et al.*, 1982; PINE and BATCHELOR, 1984; TALEBI and CORNET, 1987; HOUSE, 1987; FEHLER, 1989). In most cases this microseismicity is caused by shear events generated by the decrease in effective normal stress, supported by pre-existing fracture surfaces. This decrease in effective normal stress is caused by the increase in interstitial pressure induced by water injection.

In this paper, attention focuses on an analysis of focal plane solutions of microseismic events induced by various water injections in a granite rock mass. This

[1] Département de Sismologie, Institut de Physique du Globe de Paris, 4 place Jussieu, 75252 Paris cedex 05, France.

analysis concerns first the possibility of using focal mechanisms for determining the regional stress field. Results obtained with a stress determination method, which integrates hydraulic test data and focal plane solutions, are discussed.

This regional stress field determination, combined with the identification of the proper fault plane for each of the consistent focal mechanisms, helps constrain the friction coefficient and the effective stress law which control the stability of this rock mass. These values provide means to map the fluid pressure away from the injection well within two fault structures which exhibit different hydraulic connection patterns.

2. Injection Tests at Le Mayet de Montagne

The granite test site at Le Mayet de Montagne, located in central France some 25 km to the southeast of Vichy, has been developed for conducting large-scale *in situ* experiments on forced water circulation (CORNET, 1989). The first deep borehole, INAG III-8, reaches 780 m, while the second one, INAG III-9, is 840 m deep and located 100 m away. Preliminary injection tests were run in these wells at flow rates equal to 8.6 l/s in order to identify the main flowing zones in the lowest 250 m from the bottom of the wells. In INAG III-9 only four significant flowing zones have been identified. The upper one occurs around 650 m.

During the early stage of the reservoir development, a small-scale circulation test was conducted between the two boreholes. Water was injected through the 250 m open hole section at the bottom of INAG III-9, with a 8.3 l/s injection flow rate and a 8.2 MPa well head pressure, for about 70 hours. At the end of this circulation test, the production well (INAG III-8) was shut off while injection proceeded for another 3 hours at 22.2 l/s (12 MPa well head pressure).

During this preliminary reservoir development, the induced seismicity was monitored with a network of fifteen 3D seismic stations. P- and S-wave velocities were determined by detonating small charges of dynamite at various depths in the two deep wells as well as in some superficial ones so as to cover various azimuths and the entire depth range in which events were expected. These blasts were also favorably utilized to determine the orientation of the horizontal components of the seismic stations. The velocity field identified in this manner has been found to be fairly anisotropic and this anisotropy has been taken into account in locating events (TALEBI and CORNET, 1987). About 100 events were recorded during the small-scale circulation experiment, from which 31 well-defined focal mechanisms could be computed (CORNET and JULIEN, 1989; see also Table 1).

The large-scale reservoir development involved three phases during which the induced microseismicity was continuously monitored by the previously mentioned network. During the first phase, injection proceeded through INAG III-8 between the bottom of the well and an inflatable packer set at 713 m. Two inflatable packers

Table 1

Location and focal plane solutions for the microseismic events observed during the initial reservoir development. Events 100, 101 and 102 were observed during initial stimulations in the well INAG III-8 while all the others correspond to injections in the well INAG III-9. Origin of coordinates is on the INAG III-8 well head. For the nodal planes, d is azimuth and p is dip while i is rake. δ and ε refer to standard deviations of the parameter shown as index

				First nodal plane						Second nodal plane					
No.	X (east)	Y (north)	Z (downward)	($d1$,	$p1$,	$i1$)	($\delta d1$,	$\delta p1$,	$\delta i1$)	($d2$,	$p2$,	$i2$)	($\delta d2$,	$\delta p2$,	$\delta i2$)
1	87 ± 7	−56 ± 4	850 ± 13	266	66	48	30	7	20	150	48	146	20	3	15
2	68 ± 8	−96 ± 8	640 ± 8	342	78	223	12	4	7	240	48	343	12	5	8
7	92 ± 7	−108 ± 1	664 ± 10	96	32	226	7	5	6	326	67	294	7	4	6
8	88 ± 7	−101 ± 5	655 ± 8	356	58	237	10	5	10	226	45	310	10	6	12
12	71 ± 8	−56 ± 10	656 ± 8	183	71	199	10	2	5	87	72	340	14	4	3
14	95 ± 5	−37 ± 2	532 ± 2	120	84	36	5	2	5	25	55	173	1	5	3
15	55 ± 2	−78 ± 3	770 ± 13	172	80	230	4	2	3	70	40	345	4	2	2
21	63 ± 15	−58 ± 4	830 ± 15	339	58	21	11	4	4	237	72	146	11	3	5
23	75 ± 8	−42 ± 2	823 ± 13	354	79	205	2	1	6	258	65	347	2	6	1
24	55 ± 3	−142 ± 3	478 ± 6	209	88	238	15	4	6	115	32	356	15	4	6
26	95 ± 2	−107 ± 2	668 ± 9	194	84	40	3	2	5	99	50	172	4	5	2
27	67 ± 3	−50 ± 2	831 ± 13	180	89	224	2	2	2	90	46	359	2	2	2
29	87 ± 6	−122 ± 6	660 ± 15	78	65	188	1	5	2	346	82	335	3	1	5
31	75 ± 3	−40 ± 4	800 ± 6	182	70	203	1	4	2	85	68	339	2	2	4
32	98 ± 3	−108 ± 5	770 ± 15	160	75	221	6	2	6	56	45	339	6	3	3
33	92 ± 3	−64 ± 3	763 ± 12	142	86	220	8	2	3	48	50	355	9	2	3
34	50 ± 0	−100 ± 5	950 ± 10	22	81	181	1	1	1	291	89	352	1	1	1
38	75 ± 2	−62 ± 8	798 ± 5	140	85	220	9	2	2	46	50	354	11	2	2
43	52 ± 3	1 ± 3	520 ± 12	248	42	56	10	9	27	108	56	116	20	7	25
45	86 ± 2	−109 ± 4	653 ± 4	242	88	54	10	2	3	150	36	177	13	2	5
49	66 ± 4	11 ± 5	486 ± 10	296	74	24	3	2	3	199	68	163	1	3	2
51	61 ± 3	12 ± 4	509 ± 9	243	48	18	5	13	3	142	76	136	5	2	7
52	61 ± 1	−49 ± 2	449 ± 5	72	79	38	2	2	2	334	54	167	2	2	2
55	73 ± 3	−66 ± 3	816 ± 11	170	84	225	5	2	2	74	46	350	7	2	2
58	61 ± 2	25 ± 3	482 ± 11	256	46	35	5	7	10	140	66	131	5	5	8

Continued overleaf

Table 1 (*Contd.*)

No.	X (east)	Y (north)	Z (downward)	First nodal plane ($d1$,	$p1$,	$i1$)	($\delta d1$,	$\delta p1$,	$\delta i1$)	Second nodal plane ($d2$,	$p2$,	$i2$)	($\delta d2$,	$\delta p2$,	$\delta i2$)
59	55 ± 2	-29 ± 3	825 ± 10	160	80	223	8	4	2	60	48	346	8	4	5
61	87 ± 1	-5 ± 8	555 ± 17	50	50	185	1	1	3	317	88	320	5	4	1
62	101 ± 3	-12 ± 14	770 ± 30	324	77	211	13	4	4	224	60	344	3	4	4
66	83 ± 1	-84 ± 2	521 ± 6	324	80	231	14	4	5	221	40	344	14	5	5
69	80 ± 2	-69 ± 3	477 ± 5	340	72	261	6	2	2	185	20	293	21	10	20
70	74 ± 3	-2 ± 4	512 ± 6	230	50	12	5	4	2	132	80	140	3	3	5
71	71 ± 3	-50 ± 3	827 ± 3	168	81	221	5	2	4	70	50	349	6	3	3
100				305	69	61				195	48	140			
101				325	68	8				233	85	149			
102				330	68	15				236	80	149			

were also placed in INAG III-8 in order to limit as much as possible short circuits caused by the well. Injection proceeded for 210 hours at a flow rate equal to 8.3 l/s with a well head pressure which varied from 7.5 MPa at the beginning of the test to 9.1 MPa (stabilized value at the end of the test). Only two microseismic events were observed during this phase. Thereafter the injection flow rate was increased to 16.7 l/s with a well head pressure reaching 10.8 MPa (total injected volume of 11 665 m^3). During this phase eleven microseismic events were monitored, ten of which yielded clear fault plane solutions (Table 2).

During the second phase, injection proceeded through the 250 m long open hole section at the bottom of INAG III-9 at a flow rate equal to 8.3 l/s with a well head pressure equal to about 9.2 MPa. A stationary condition was reached after one week of injection. This stationary condition was maintained for about 21 days so that the total injected volume for this phase reached 14 790 m^3. During this phase, 50 microseismic events were recorded from which 23 yielded well-defined focal mechanisms (Table 2).

The third phase (injection between 600 m and 840 m in INAG III-9) involved a first period designed for characterizing the hydraulic properties of the system while the second period was run for testing long duration stationary circulation conditions. During the first period the system was tested for various flow rates. Each flow rate was maintained constant for periods ranging from 5 to 3 days. The maximum flow rate reached 21.1 l/s with a well head pressure equal to 12.5 MPa after three days of pumping, then the flow rate was decreased to 16.6 l/s. During this third period 46 microseismic events were recorded from which 19 yielded a well-defined focal mechanism (Table 2). No event was recorded during the pumping tests at flow rates smaller than, or equal to, 8.3 l/s (well head pressures smaller than 9.3 MPa). All events occurred during the initial period of this phase except for one event which occurred just before the end of pumping, when the flow rate had been increased to 12.5 l/s (well head pressure equal to 10.2 MPa) and another one occurred when pumping had stopped. The total injected volume during the first period of this phase reached 16 310 m^3.

Thus, while the seismic activity monitored during the early reservoir development (about one hundred events) corresponds to a total injected volume of about 2200 m^3, the various seismically active phases (11 events, 50 events, 46 events) associated with the large-scale injection tests correspond to injected volumes ranging from 11 665 m^3 to 16 310 m^3. The location of all events recorded while injection was proceeding through the well INAG III-9 are shown on Figure 1.

The duration of most events ranges between 0.3 and 0.5 seconds, with the largest ones reaching 0.6 s. The *P*-wave corner frequencies vary between 200 and 400 Hz while the seismic moments vary between 10^7 and 10^8 Nm. Accordingly, the magnitudes of these events range between -2 and -1.

Three main active zones can be identified in Figure 1: a deeper zone, in which no clear structure has been identified, and two subplanar structures. CORNET and

Table 2

Location and focal plane solutions for the microseismic events observed during the large-scale injection tests. Coordinate system is centered on the well head of INAG III-8. For the nodal planes d is azimuth and p is dip, i is rake; ε and δ refer to the standard deviation of the parameter shown as index

No.	X(east)	Y(north)	Z(down)	First nodal plane						Second nodal plane					
				(d1,	p1	i1)	(δd1,	δd1,	δd1)	(d2,	p2,	i2)	(δ2,	δp2,	δi2)
2	21 ± 7	51 ± 16	803 ± 3	28	75	196	5	4	3	294	75	345	5	2	4
3	22 ± 6	50 ± 5	757 ± 15	121	70	184	6	2	3	30	86	340	7	3	2
4	22 ± 1	−124 ± 7	557 ± 10	326	80	227	5	2	6	225	44	345	8	5	4
5	22 ± 3	−118 ± 4	553 ± 2	49	85	2	5	3	3	319	88	175	5	3	3
6	23 ± 2	−248 ± 3	428 ± 6	34	70	11	4	3	10	300	80	160	6	9	3
7	166 ± 8	78 ± 2	849 ± 7	28	77	206	6	5	4	292	65	346	8	3	5
8	91 ± 14	−14 ± 4	505 ± 8	324	80	190	3	3	3	232	80	350	4	2	3
9	5 ± 6	−254 ± 2	385 ± 8	53	80	20	5	2	6	319	70	169	6	6	3
10	46 ± 3	1 ± 2	464 ± 12	356	70	190	5	5	2	262	80	340	3	1	5
11	32 ± 4	−109 ± 5	562 ± 25	76	82	16	3	2	2	344	74	172	5	2	3
13	26 ± 4	−131 ± 3	601 ± 3	344	88	212	3	2	7	253	58	358	5	7	2
15	70 ± 3	−45 ± 1	494 ± 7	332	85	202	4	2	3	240	68	355	5	3	3
16	83 ± 4	−67 ± 9	439 ± 12	350	88	18	2	2	2	259	72	178	4	2	2
17	100 ± 5	−51 ± 3	523 ± 3	22	70	219	4	2	9	277	54	335	10	7	6
19	14 ± 15	−68 ± 5	858 ± 13	296	70	191	3	5	2	202	80	336	4	1	5
20	69 ± 2	−42 ± 4	498 ± 14	348	78	201	6	2	3	254	70	347	8	3	3
21	100 ± 10	−100 ± 2	798 ± 2	284	72	186	4	4	2	192	84	342	3	2	5
23	73 ± 6	−74 ± 4	416 ± 1	83	78	14	7	2	2	350	76	168	6	2	2
24	99 ± 10	−56 ± 9	813 ± 7	141	86	206	4	2	3	49	64	356	3	3	2
26	96 ± 6	5 ± 10	500 ± 18	254	50	27	6	4	5	146	70	137	10	2	4
29	129 ± 5	−61 ± 8	563 ± 22	26	70	32	4	2	6	284	60	157	7	5	3
31	93 ± 2	−89 ± 4	839 ± 6	140	85	205	3	2	5	48	65	355	4	5	2
34	103 ± 9	−65 ± 3	566 ± 12	311	88	207	7	2	2	220	63	358	8	2	3
35	106 ± 7	−53 ± 5	567 ± 8	320	75	196	3	2	3	226	75	345	5	2	3
36	114 ± 11	−93 ± 6	795 ± 7	286	79	185	3	5	2	195	85	349	4	2	5
38	114 ± 2	−47 ± 5	554 ± 7	80	82	36	5	2	5	344	55	170	8	4	3
40	122 ± 1	−167 ± 7	621 ± 10	29	68	11	4	1	10	295	80	158	7	9	2

41	84 ± 2	−15 ± 1	566 ± 5	250	90	330	4	2	6	340	60	180	4	6	3
42	45 ± 5	−90 ± 3	804 ± 9	360	90	348	2	2	4	90	78	180	3	4	2
46	75 ± 1	10 ± 2	492 ± 6	342	86	198	3	1	3	251	72	355	5	3	2
48	119 ± 14	−74 ± 12	913 ± 16	165	75	202	7	4	4	69	69	344	6	2	4
51	78 ± 14	20 ± 8	294 ± 12	82	43	62	5	2	10	298	53	114	11	2	10
56	55 ± 5	−29 ± 4	847 ± 9	168	82	217	3	2	3	72	53	350	5	3	3
64	93 ± 8	−19 ± 7	530 ± 3	345	84	188	5	2	3	254	82	354	6	3	2
65	72 ± 3	8 ± 4	501 ± 23	268	76	24	3	2	5	172	67	165	5	4	3
67	76 ± 3	−19 ± 2	806 ± 10	296	68	185	4	5	1	204	85	338	6	1	5
71	93 ± 6	−75 ± 4	548 ± 6	356	78	201	6	1	7	262	70	347	7	6	2
76	84 ± 2	−17 ± 2	485 ± 8	336	80	200	4	2	3	242	70	349	7	3	2
78	104 ± 12	−56 ± 3	568 ± 9	332	84	212	5	2	5	238	58	353	7	5	4
80	105 ± 9	−57 ± 2	831 ± 4	314	80	210	6	3	4	218	60	348	8	4	4
83	77 ± 4	−12 ± 2	483 ± 8	334	86	202	3	2	3	242	68	356	4	3	3
88	123 ± 8	−83 ± 2	369 ± 15	133	90	57	5	4	3	43	33	180	5	3	7
90	97 ± 2	−59 ± 11	568 ± 10	336	85	194	7	2	3	245	76	355	8	2	3
92	30 ± 2	−77 ± 4	401 ± 4	33	64	205	5	2	7	292	68	332	9	6	4
93	96 ± 8	−53 ± 1	564 ± 2	121	75	182	5	2	3	31	88	345	5	2	2
94	82 ± 3	−32 ± 5	939 ± 6	264	75	180	5	5	1	174	90	345	5	1	5
95	129 ± 6	−100 ± 4	801 ± 4	18	64	202	8	4	7	278	70	332	8	5	5
96	81 ± 5	−64 ± 3	853 ± 25	290	75	188	5	5	3	198	82	344	5	2	5
97	103 ± 9	4 ± 4	870 ± 3	304	84	204	4	1	5	211	66	353	5	5	2
98	98 ± 3	−72 ± 7	528 ± 8	236	42	8	7	5	6	140	85	132	6	2	5
102	101 ± 5	−62 ± 4	558 ± 9	298	86	201	4	2	3	207	69	356	5	3	3
105	103 ± 11	−64 ± 4	568 ± 7	298	85	202	4	1	3	206	68	355	5	3	2

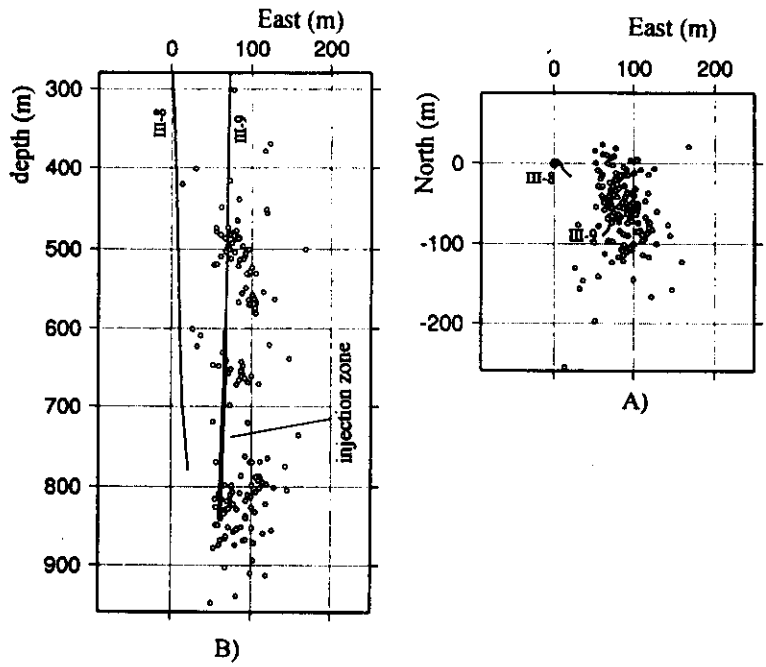

Figure 1
Location of all events recorded while injection was proceeding through the well INAG III-9. A) Projection on a horizontal plane, B) Projection on a vertical plane oriented in the east-west direction. Injection was conducted between 598 m and 840 m.

SCOTTI (1993) identified by a least-squares technique the best fitting planes passing through the upper and lower planar structures. The upper seismic zone fits with a plane oriented N 04°E and dipping 61° to the east. It intersects the well INAG III-9 in the 481–521 m depth range. The lower planar structure has been fitted with a plane oriented N 174°E and dipping 36° to the east. It intersects the well INAG III-9 in the depth range 630–654 m. Within both these depth intervals sonic logs outline zones of alterations, confirmed by the analysis of the cuttings produced during drilling operations.

Interestingly, none of these orientations could be identified from a statistical analysis of the fractures identified by borehole imaging within these depth intervals. Yet it is one of the dominant fault orientations mapped on site. This demonstrates that the small-scale morphology of a fractured (fault) zone does not always reflect its large-scale geometry and that fault zones may involve small-scale fractures of very diverse orientations. Also, while both zones are clearly visible on the geophysical logs and in the cuttings, only those around 650 m exhibit a significant hydraulic conductivity: The zone intersected around 500 m does not appear on the initial flow

logs and therefore is not connected to the large-scale hydraulically significant fracture network (CORNET and SCOTTI, 1993).

3. Determination of the Regional Stress Field

The regional stress field has been determined by three different methods: The Hydraulic Tests on Pre-existing Fractures (HTPF) method, the inversion of focal mechanisms of induced seismicity, the simultaneous inversion of HTPF data and focal plane solutions. These results have already been published (CORNET and JULIEN, 1989; CORNET *et al.*, 1992; YIN and CORNET, 1994). They are briefly recalled here for later discussions.

3.1 The HTPF Stress Determination

The HTPF method consists of conducting hydraulic tests on pre-existing fractures of known orientation (characterized by the normal $\mathbf{n}$ to the fracture plane) for determining the normal stress σ_n supported by the fracture plane. The problem is to determine the six components of the stress σ such that $\sigma\mathbf{n} \cdot \mathbf{n} = \sigma_n$. The regional stress field σ is presumed to vary linearly with the spatial coordinates (x_1, x_2, x_3; x_1 horizontal, positive to the north, x_2 horizontal, positive to the east, x_3 vertical, positive downward):

$$\sigma = \mathbf{S} + x_1\alpha^1 + x_2\alpha^2 + x_3\alpha^3 \tag{1}$$

where $\mathbf{S}$, α^1, α^2, α^3 are symmetrical tensors. α^1, α^2, α^3 are the stress gradients respectively in the x_1, x_2, x_3 directions. Equilibrium conditions show that, in the absence of topography or lateral heterogeneities ($\alpha^1 = \alpha^2 = 0$), one of the principal directions of α^3 is vertical (CORNET, 1992). This result is very similar to that proposed by MCGARR (1980) except that, here, no assumption is made regarding the constitutive equation of the rock mass. It is only assumed that, within the domain of interest, the stress field varies fairly smoothly around some central point so that its components can be approximated by linear functions. From now on the tensor α^3 will be simply denoted by α. The stress determination consists of determining $\mathbf{S}$ and α derived from N HTPF data. A HTPF datum includes both the normal stress measurement and the fracture orientation determination.

At Le Mayet de Montagne, eighteen HTPF measurements have been conducted between 60 m and 730 m, prior to the water circulation experiments. For this stress determination the regional stress field and its first derivative are assumed continuous up to ground surface. The solution is defined by the principal values of $\mathbf{S}$($S_1 = 5.1$ MPa, $S_2 = 0.2$ MPa; $S_3 = 0$; S_1 is horizontal and oriented N 24°E.) and α($\alpha_1 = 0.0226$ MPa/m; $\alpha_2 = 0.0084$ MPa/m; $\alpha_3 = 0.0264$ MPa/m; α_1 is oriented 104°

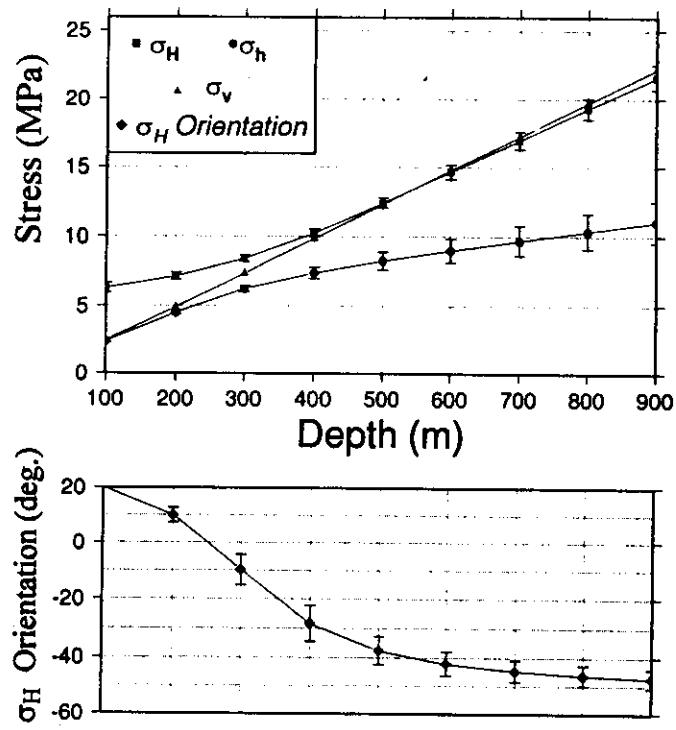

Figure 2
Stress profiles derived from the HTPF measurements conducted prior to the injection tests. σ_H orientation is measured from the north and positive eastward.

to the north of S_1). Values for the horizontal principal stress magnitudes σ_H and $\sigma_h(\sigma_H > \sigma_h)$ and for the orientation of σ_H with respect to north (positive eastward) are indicated for various depths in Figure 2.

Two and a half years after the main water circulation experiment was completed, another 13 HTPF measurements have been carried out in well INAG III-9. These measurements demonstrate that no permanent large-scale stress perturbation has been induced by the various water injections (CORNET 1992). It has been observed, however, that two of these HTPF measurements (at 780 m and 773 m) are heterogeneous with respect to the original regional stress field and that, according to a spinner log, these heterogeneous data are located close to one of the most hydraulically significant zones of the borehole.

3.2 Integration of Focal Solutions in the Stress Determination

A few authors (e.g., VASSEUR *et al.*, 1983; GEPHART and FORSYTH, 1984; JULIEN and CORNET, 1987; RIVEIRA and CISTERNAS, 1990) have proposed deter-

mining the regional stress field from an inversion of the focal plane solutions of seismic events. These determinations asssume that the stress field is uniform throughout the volume in which the seismic events occurred and that the slip vector is parallel to the resolved shear stress supported by the slipping planes (WALLACE, 1951; BOTT, 1959). Because only the direction of the shear component is constrained (and not its magnitude), these stress determinations yield only the principal stress directions (defined by the Euler angles ϕ, ψ and θ where ϕ and ψ are respectively the azimuth and dip of σ_1 and θ is the angle between the σ_2 direction and the horizontal plane) and a factor R characteristic of the ellipticity of the tensor: $R = (\sigma_2 - \sigma_1)/(\sigma_3 - \sigma_1)$; $(\sigma_1 > \sigma_2 > \sigma_3)$.

CORNET and JULIEN (1989) attempted a first stress determination with the focal mechanisms of the microseismic events observed during the preliminary reservoir development (injection of 2200 m^3). In order to satisfy the hypothesis of stress uniformity, they considered three different depth ranges: an upper one (above 550 m), an intermediate one (between 750 m and 550 m) and a lower one (below 750 m). For the two upper systems no satisfactory solution could be identified (too many inconsistent data). For the deeper system, 14 well-defined focal mechanisms were available for the inversion. Results establish that the maximum principal stress is vertical, but the maximum horizontal principal stress is oriented 70° to the east of the HTPF solution ($\varphi = 329°$, $\psi = 79°$, $\theta = 24°$, $R = 0.55$; Figure 3). This solution is consistent with 12 of the 14 mechanisms.

Another stress determination (YIN, 1994) has been undertaken with the complete set of focal mechanisms (seismicity induced by the large-scale injections combined with that of the early reservoir development). Here again the data has been separated into three different depth ranges in order to satisfy the stress homogeneity hypothesis. Although the resolution is not very good, results are far more satisfactory than Cornet and Julien's solution. For the deeper seismic system (Fig. 4), the solution yields $\varphi = 354°$, $\psi = 46°$, $\theta = 92°$, $R = 0.32$. For all depth

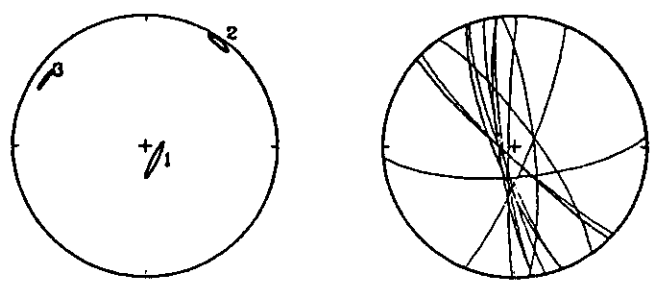

Figure 3
Stress determination derived from the inversion of focal mechanisms of the microseismic events observed during the preliminary reservoir development (total injected volume of 2200 m^3). Only the deepest seismic domain (see Fig. 1B) is considered. The stereographic projection of the principal directions is shown on the left. The orientation of selected planes is shown on the right.

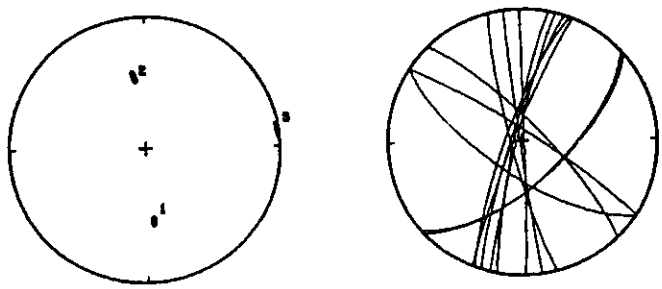

Figure 4
Same as Figure 3 but the seismic events considered are those induced by the large-scale reservoir development (injected volumes of 14 790 m^3 and 16 310 m^3).

ranges, a systematic 20 to 30 degrees discrepancy is observed for the maximum horizontal principal stress orientation, as determined on the one hand with this focal plane inversion and on the other hand with the HTPF method.

While the HTPF solution remains stable when new data are introduced, the focal plane solution varies, depending on the set of data considered for the inversion. As mentioned above, the post-circulation HTPF measurements outlined zones of local stress heterogeneity associated with some of the main flowing zones. Thus it has been concluded that some of the focal mechanisms are very likely "polluted" by local stress heterogeneities, and these, in turn, influence the stress determination.

However, the HTPF measurements involve only subvertical fractures, resulting in very poor resolution on the vertical stress component. Further, the HTPF stress determination assumes that the stress field is continuous up to the surface and that the vertical direction is principal at all depths. In order to alleviate these limitations and take advantage of those focal mechanisms which are not influenced by local stress heterogeneities, a joint inversion method integrating the HTPF data and the focal mechanisms has been developed (YIN and CORNET 1994). In this inversion scheme the stress field is represented by ten parameters. In equation (1), the tensor S represents the stress at a given depth; none of its six components (the three principal values S_1, S_2 and S_3 and the three Euler angles λ_1, λ_2 and λ_3) is assumed *a priori* to be null. The tensor α is the vertical stress gradient around this depth and lateral stress variations are presumed to be negligible within the domain of interest. Equilibrium conditions impose that α exhibits a vertical principal direction so that it is described by 4 parameters. The inversion scheme uses a genetic algorithm to identify the optimal solution and a Monte Carlo method to estimate the uncertainty of the determination.

This integrated stress determination has been conducted with all the focal mechanisms available for the site (including those found to be heterogeneous with HTPF stress determination) and with HTPF data obtained within the same depth

interval as that of the focal mechanisms (all data obtained above 250 m have not been included). Further, the two deep HTPF measurements conducted close to a fracture zone which had been identified as being heterogeneous, have also been disregarded. This provides 87 focal mechanisms and 22 HTPF measurements.

Results of the joint inversion yields for S (defined at 750 m): $S_1 = 20$ MPa, $S_2 = 19.4$ MPa and $S_3 = 11.8$ MPa, $\lambda_1 = -34°$, $\lambda_2 = 86°$ and $\lambda_3 = 88°$. The principal values for the vertical gradient are $\alpha_1 = 0.0226$ MPa/m, $\alpha_2 = 0.0084$ MPa/m; $\alpha_3 = 0.0264$ MPa/m (in the vertical direction); the orientation of α_1 with respect to the north is $\eta = \text{N}162°\text{E}$.

The stress field and its uncertainty are shown on Figure 5 for various depths. The maximum principal stress was found to be vertical below 700 m and is equal to the weight of overburden as determined from the rock density (0.026 MPa/m). Also, the orientation of the maximum horizontal principal stress is very close to that determined with the sole HTPF measurements.

The misfit between a given fault plane and a given stress tensor is characterized by the rotation which must be applied to the fault plane in order to bring the resolved shear stress supported by the fault parallel to the slip vector observed for this plane. A focal plane is considered inconsistent with a given tensor when its misfit is larger than three times the standard deviation associated with the plane orientation determination. The results obtained from the joint inversion are consistent with 21 of the HTPF measurements and 70% of the focal plane solutions. This clearly shows that a few microseismic events occur in zones of stress heterogeneity.

Given the observation mentioned earlier that fault zones involve small-scale fractures of very diverse orientation, it may be anticipated that locally, along the fault plane, the stress is very heterogeneous with respect to the regional stress field. Spectral analysis of the *P* waves for the microseismic signals reveals corner frequencies in the 200–500 Hz range (TALEBI and CORNET, 1987). Thus, the mean size of these events is estimated to stand somewhere between 0.5 and 5 m. This suggests that the rock volume affected by the stress heterogeneities causing the discrepancy between the observed slip plane and the estimated resolved shear stress, is of the same order of magnitude.

4. Identification of Stress Heterogeneities near Fault Zones

In order to easily conduct stress determination with the HTPF technique, MOSNIER and CORNET (1989) have developed a tool (the HTPF tool) combining an electrical imaging function with a wireline straddle packer. The electrical imaging function is used first to identify pre-existing fractures of various dip and azimuth in the borehole. Next, the straddle packer is placed precisely at the required depth, by means of real time imaging of the borehole wall, and hydraulic tests are run in order to measure the normal stress supported by these pre-existing

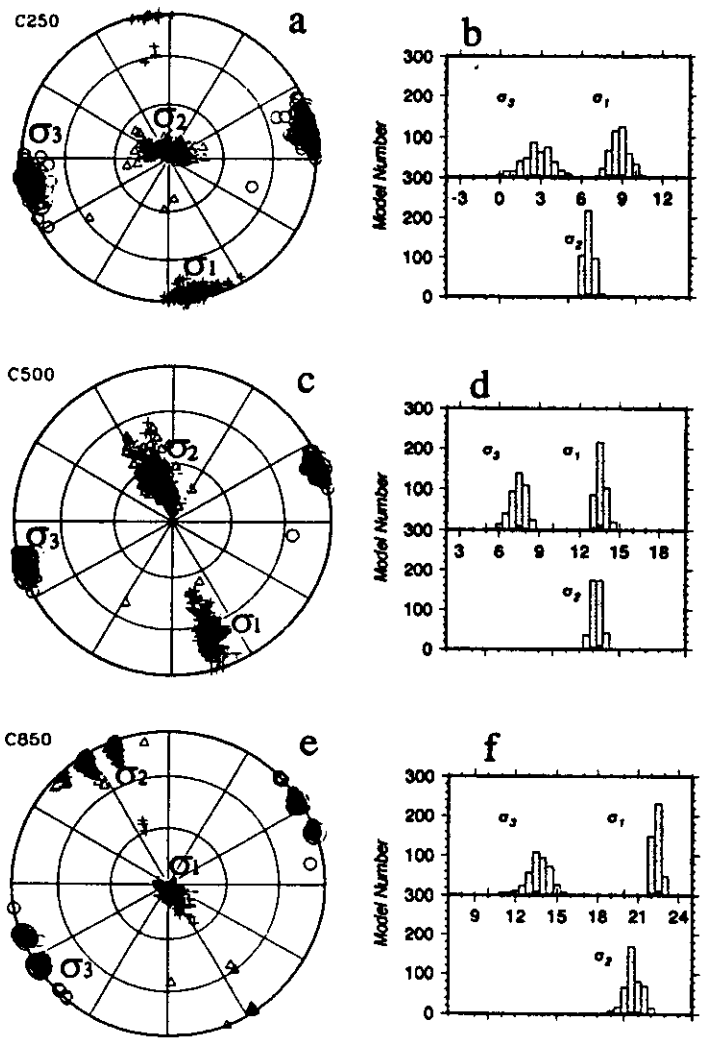

Figure 5
Stress determination obtained after integrating 22 HTPF measurements and 87 focal mechanisms. The stress field is presumed to vary linearly with depth. Results are shown at three different depths (250 m, 500 m, 850 m). a), c) and e) refer to the principal stress directions while the magnitudes (in MPa) are shown on b) d) and f). These results correspond to 430 models which are included within 95% confidence level.

fractures. This provides a unique opportunity to thoroughly investigate stress heterogeneities associated with local faults or altered zones.

As mentioned above, CORNET (1992) successfully used this technique to identify a stress perturbation in the vicinity of one of the most significant flowing zones in the well INAG III-9. SCOTTI and CORNET (1994a) analyzed two different mecha-

nisms for modelling this observed heterogeneity. The first one assumes that the fault zone can be assimilated with a soft inclusion in an otherwise stiff rock; the second one supposes that the shear stress supported by the fault plane was partially released through creep or friction. Only the second mechanism (shear stress relief) was found to be consistent with observations. Further, this mechanism was also shown to be consistent with heterogeneities identified with the focal plane solutions of induced seismicity. Thus, a new set of HTPF measurements has been undertaken in order to determine whether the stress field near the two upper planar seismic zones is also heterogeneous with the regional stress field and consistent with a local shear stress relief. Results are shown in Table 3.

In Table 3, the measured values of normal stress are compared to the values computed with the regional stress field identified by the integrated method. Given the uncertainty on the orientation of the fracture planes (about 5°), many of these results are found to be consistent with the computed regional stress. Locally, within the depth interval at which the upper planar seismic zone intersects the well, some data are found to be heterogeneous while some nearby data (less than 6 meters away) are found to be consistent. This supports the proposition that very locally the stress field near and within fault zones is heterogeneous so that focal plane solutions of induced seismicity may not be representative of the regional stress field.

However, the most striking result is the observation that between 550 m and 611 m the measured normal stress is larger than the regional maximum principal stress, in some places by as much as 10 MPa. Clearly this observation does not fit the uniform shear stress relief process proposed by SCOTTI and CORNET (1994a), but requires some locally heterogeneous slip motion. It is not clear at this point whether this heterogeneity of slip motion is associated with the spatial extension of the fault zones or if it is associated with heterogeneous slip within the faults. The quality of the data does not provide means for precisely constraining the geometry of the fault zones. Nonetheless these results do demonstrate that faults are associated locally with very heterogeneous stress distributions so that focal plane solutions may not be representative of the regional stress field.

It is concluded that, when only focal mechanisms are used to determine the regional stress field, those which are clearly inconsistent with this regional stress are easily identified by the inversion technique, but those which are only slightly inconsistent influence the solution and induce some systematic error. Hence the different results obtained with the different sets of focal mechanisms, and the systematic error observed between fault plane inversions and HTPF measurements.

It could be argued that this conclusion is only valid for focal mechanisms of induced seismicity because of the small size of the events considered for this analysis. Although this will not be further discussed here, it will be mentioned that SCOTTI and CORNET (1994b) have reached conclusions similar to those presented here above, after comparing results from various HTPF stress determinations with the focal mechanisms of natural seismic events with magnitude ranging from 3 to

Table 3

HTPF data obtained in 1994 in order to explore the stress field in the vicinity of the upper and lower planar seismic zones. x_3, ϕ, θ, σ_n are respectively the values measured for the depth, the azimuth and the dip of the normal to the fracture plane and the normal stress supported by the fracture plane. ϕ_c, θ_c, σ_{nc} are the a posteriori values for ϕ, θ, σ_n as determined by the least squares inversion procedure. ε_ϕ, ε_θ, $\varepsilon_{\sigma n}$ are the standard deviations on the measurements. $\Delta\sigma_n$ is the difference between the measured value and that expected from the integrated stress determination. When $\Delta\sigma_n$ is larger than 1 MPa, the measurement is considered heterogeneous with the regional stress field; it is not considered for the stress determination. Note the strong heterogeneity around 600 m, i.e., in between the two planar seismic zones. Since these seismic zones exhibit very strong dip, they remain fairly close to the borehole for long depth intervals.

x_3 m	ϕ	ε_ϕ	ϕ_c	θ	ε_θ	θ_c	σ_n MPa	$\varepsilon_{\sigma n}$ MPa	σ_{nc} MPa	$\Delta\sigma_n$ MPa
401	114,0	4	105,0	85,9	2	86,0	8,5	0,2	8,9	−0,4
482	115,0	4	117,0	80,1	2	80,0	12,3	0,5	11,6	0,7
501	68,7	4	73,0	89,0	2	88,9	9,6	0,2	9,3	0,3
554	132,0	4	132,6	89,1	2	89,1	14,3	0,3	14,2	0,1
558	103,2	5	118,8	88,5	2	88,4	15,3	0,4	13,7	1,6
665	196,0	4	193,0	85,5	2	85,43	12,8	0,3	12,6	0,2
678	187,0	4	179,4	85,5	2	85,3	14,8	0,3	14,4	0,4
686	180,0	4	188,6	73,3	2	74,1	13,3	0,3	13,7	−0,4
762	262,9	4	263,0	7,3	2	7,0	20,0	0,3	19,6	0,4
446	192,0			81,1			12,8	0,3	10,3	2,5
530	182,0			81,1			15,0	0,5	12,0	3,0
597	95,0			85,8			17,3	0,4	12,7	4,6
605	43,5			84,3			20,6	0,4	10,2	10,4
611	276,0			80,0			23,4	0,4	13,2	10,2
698	134,5			86,0			13,8	0,3	17,8	−5,0

4.5. Given the proposition that slip motion along faults is very heterogeneous (HERERO and PASCAL, 1994; COCHARD and MADARIAGA, 1994), it seems reasonable to anticipate that the stress field in the vicinity of fault zones is also very heterogeneous. This implies that some aftershocks of major seismic events are also very likely affected by local stress heterogeneities so that inversion of focal mechanisms of aftershocks may lead to biased stress determinations.

Further, considering the Le Mayet de Montagne results, one may wonder if the source of the heterogeneities are to be found in the morphology of the fault or simply in the heterogeneity of the slip motion along the fault. Answering this question will require some modelling which has not yet been done. Given the fact that many of the microseismic events are located a short distance from the main fault zone identified with the least-squares technique, and that most of the slip planes observed for these events are not parallel to this main fault plane, it seems very likely that morphology plays a significant role in developing the stress heterogeneities. This may

in turn induce a heterogeneous slip motion along the main fault which may further enhance these stress heterogeneities. Only modelling, in close connection with detailed mapping of the stress heterogeneities, will help resolve this question. This modelling requires an accurate description of the local pore pressure within the fault. This is discussed now.

5. Analysis of the Consistent Focal Mechanisms for Pore Pressure Mapping

In addition to the regional stress determination, the joint inversion of HTPF data and focal plane solutions yields two results. First it identifies those focal mechanisms which are homogeneous with the regional stress field; then for these mechanisms it selects which of the two nodal planes is the slipping plane. This can be beneficial in obtaining some estimate of the friction coefficient for this rock mass. It can also be used to map the pore pressure perturbations induced by the fluid injections.

It is often assumed that the shear strength of pre-existing fractures obeys the effective stress principle (TERZAGHI, 1945), namely that the resistance to shear depends on the difference between the total normal stress (σ_n) supported by the fractures and the fluid pressure (p_p) assumed to act on the totality of the fracture area undergoing failure ($\sigma'_n = \sigma_n - p_p$). However, it also has been proposed (ROBINSON and HOLLAND, 1970) to consider that, since the pore space corresponds to a fraction of the total fracture area, only a fraction (β) of the pore pressure is to be considered for the effective normal stress ($\sigma'_n = \sigma_n - \beta p_p$). In the present paper we have considered both possibilities ($\beta = 1$ or $\beta = 0.9$) and assumed that the shear strength of pre-existing fractures follows Coulomb's friction law, with the assumption of zero cohesion

$$|\tau| = \mu(\sigma_n - \beta p_p) = \mu\sigma'_n. \tag{2}$$

The pore pressure at the location of a microseismic event can be written $p_p = p_0 + dp$, where p_0 is the original hydrostatic pressure and dp is the increment of pressure induced by the fluid injection. This yields

$$dp = \{(\sigma_n - \beta p_0)/\beta[1 - |\tau|/\mu(\sigma_n - \beta p_0)]\}. \tag{3}$$

The value of dp can be normalized with respect to p_i, where p_i is the increment of pressure with respect to hydrostatic pressure in the injection well at the depth of injection (i.e., the well-head pressure corrected for pressure losses caused by flow through the tubing in the injection well). In the rock mass, the ratio dp/p_i varies between 1, in the vicinity of the injection hole where pre-existing fractures are opened, and 0 near the production well or near the far field boundary, where the interstitial pressure is hydrostatic. On Figure 6, β is assumed to be equal to one (standard effective stress law) and the values for dp/p_i have been plotted versus the

values of $|\tau|/\mu(\sigma_n - \beta p_0)$, first with μ equal to 1 (Fig. 6a), second with μ equal to 0.6 (Fig. 6b). It may be observed that if the friction coefficient μ becomes slightly larger than 1, then the local pore pressure increment required to induce shear would have to be larger than the injection pressure. Also, if the friction coefficient is equal to 0.6, the pressure required to induce slip for some events is about equal to hydrostatic pressure. Thus the friction coefficient is found to stand somewhere between 0.95 and 0.65, i.e., values which are fairly common for most rocks. Results shown on Figure 7 are similar to those of Figure 6 (for a friction coefficient of 0.5) except that β has been taken equal to 0.9 (the pore pressure is not acting throughout the complete area of the fracture). These results suggest that, with such an effective stress law, the pressure required to induce slip for some of the events is larger than the injection pressure. Yet for other planes, equilibrium is barely reached with hydrostatic pressure conditions. This demonstrates that for this rock mass Terzaghi's effective stress concept is satisfactory, so that the coefficient β in the effective stress law applied to friction, is equal to 1.

Now, given the stress field determined with the integrated method and given the selection of the nodal planes which results from this stress determination, the selected friction law as expressed by equation (3) may be used to map the pore pressure distribution within the rock mass. The normalized pressure increment dp/p_i has been plotted as a function of the distance between the hypocenter of the corresponding seismic event and the closest point in the injection well where water penetrates the rock formation (Figure 8). It can be seen, that for some events in the upper planar seismic zone, the pore pressure increment required to induce shear some 100 m away from the injection point is nearly equal to the injection pressure increment. This implies that either only slight flow occurs through this fracture or that its hydraulic conductivity is extremely high. As mentioned above, preliminary flow logs conducted in the well before the circulation tests, revealed that the fracture zone intersected by INAG III-9 around 500 m was taking no fluid during injection, contrary to the fault zone intersected around 650 m. Thus the large pore pressure identified by the seismic activity analysis is consistent with the flow logs conducted in the borehole: the upper planar seismic zone, although hydraulically conductive, is not connected to the main fracture network of the rock mass, but is connected to the injection well.

This mapping of the interstitial pressure in the upper seismic zone raises an intriguing question regarding the hydraulic behavior of this system. Indeed, at some places the local pore pressure is nearly equal to the injection pressure (the well-head injection pressure varies between 8.3 MPa at 8.5 l/s to 12.5 MPa at 20.8 l/s), and therefore is larger than the regional minimum principal stress magnitude in this depth interval ($\sigma_h = 7.5$ MPa at 500 m). Since stress heterogeneities are only localized, according to the good fit observed for many microseismic events, this should have resulted in the development of hydraulic fracturing. But none has been identified. Indeed, during all the injection tests a network of six tiltmeters continu-

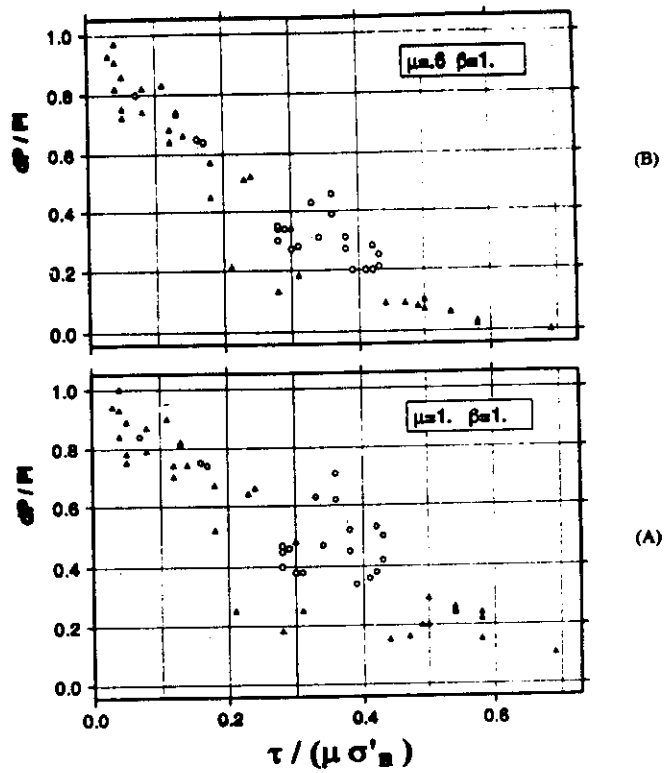

Figure 6

Calibration of the friction law controlling slippage along pre-existing fractures. On abscissa are plotted the values of the ratio between the tangential stress supported by the slip planes and the effective normal stress. On ordinate are plotted the ratio between the pressure increment required to induce slip and the injection pressure at the well head. A) The friction coefficient has been chosen equal to 1; B) The friction coefficient has been chosen equal to 0.6. In both cases the classical effective stress concept ($\beta = 1$) is assumed to be valid. Black triangles correspond to events in the upper planar seismic zone, open circles correspond to events in the lower planar seismic zone.

ously monitored the ground deformation (DESROCHES and CORNET, 1990). The absence of significant tilt during all the injection tests indicates that if any hydraulic fracture did propagate, it remained smaller than 15 to 20 m. Thus this analysis suggests that, within fault zones, the pore pressure may be significantly larger than the minimum principal stress without significant hydraulic fracturing, and this for time periods exceeding fifteen days.

The lateral extension of the lower planar seismic zone is considerably smaller than that of the upper seismic zone. Also, the pore pressure determined from the analysis of the induced seismicity is found to be substantially lower than within the upper seismic zone, and the values are decreasing regularly as the events occur

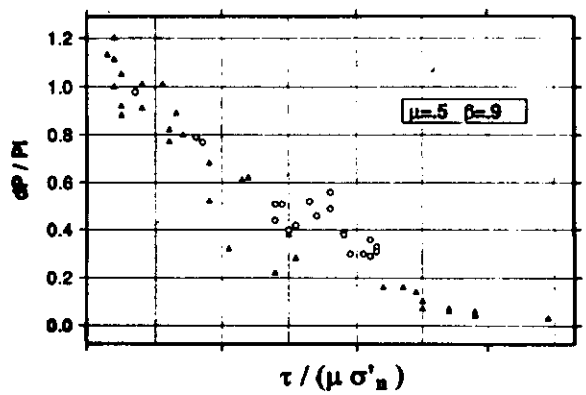

Figure 7
Same as Figure 6 but, in the effective stress law, β has been chosen equal to 0.9. Further, the friction coefficient has been chosen equal to 0.5.

further away from the well. This is consistent with the result from the flow logs which shows that this fault zone is well connected to the hydraulically significant fracture network of the rock mass.

This emphasizes the fact that induced seismicity is only representative of large pore pressure and not of large flow rate. In fact, the further away the microseismic events are from the injection well, the less likely they are to be associated with main flowing zones. Indeed, the interstitial pressure within the distant flowing zones is controlled by the far field pressure conditions and therefore, in opened systems, is too low to induce any seismicity. This is confirmed by the horizontal projection of the location of induced seismicity observed at Le Mayet de Montagne. It is observed on Figure 1 that, during injections in INAG III-9, no seismic event occured near INAG III-8 (the production well) even though the well was producing somewhere between 45% and 80% of the injection flow rate (depending on the injection flow rate). This absence of seismicity near INAG III-8 is simply linked to the low pore pressure in the vicinity of the production well.

It may be observed that none of the planar seismic zones is parallel to a principal stress direction. Thus, at least at the scale of these tests, for this granite, forced fluid flow does not occur along planes normal to the minimum principal stress but rather is controlled by a few pre-existing faults. Further, these results outline the difficulty in characterizing the hydraulic behavior of this rock mass and the shortcomings of the equivalent continuum approach: only three of four main fractures are absorbing more than 80% of the flow (BRUEL and CORNET, 1992) and these can be identified only through large-scale testing. Indeed, had straddle packer tests been conducted on the various fractures intersected by the wells, these tests would have shown that the zone around 500 m is locally hydraulically conductive

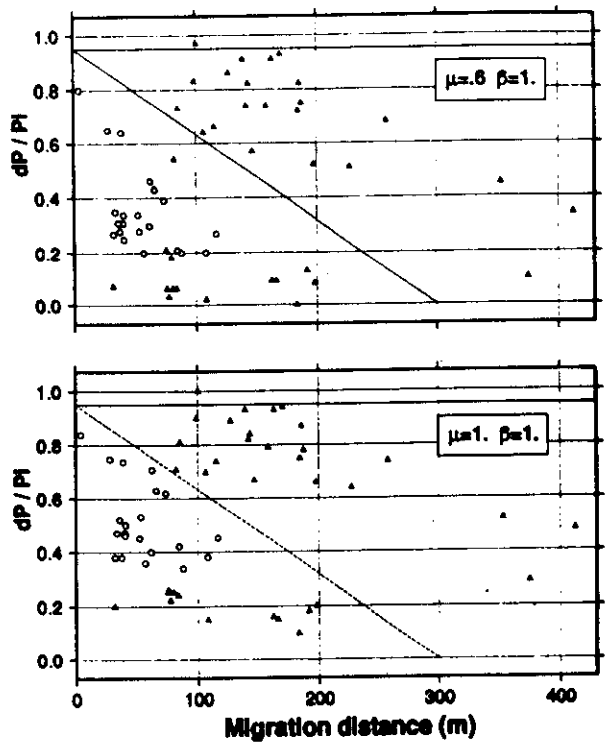

Figure 8
Mapping of the pore pressure in the rock mass during the various injections. For all focal mechanisms consistent with the integrated stress determination, the pressure increment (normalized with respect to the well-head injection pressure) required to induce slip is plotted versus the distance between the event and the closest injection point in the well (plotted in abscissa). Black triangles corrrespond to the upper planar seismic zone, the open circles refer to the lower planar seismic zone. μ is the friction coefficient, β is the corrective factor for the pore pressure in the effective stress law.

and they would have failed to identify the lack of connection at the 200 m scale. This dominance of a very limited amount of fractures on the hydraulic response of the system clearly illustrates that the concept of permeability of an equivalent continuum fails for this granite. This then raises the question of characterizing the large-scale hydraulic response of this rock mass to forced fluid flow. As shown here above, the detailed analysis of the focal plane solutions of induced seismicity, together with a sound regional stress determination, may yield part of the answer.

6. *Conclusion*

The mapping of seismic events induced by various water injections in this granite has shown that flow only occurs through a very limited number of fractured

zones. Some of these zones, although locally hydraulically conductive, are not hydraulically significant because they are not properly connected to the regional hydraulically significant system. All these fault structures exhibit a fairly intricate morphology so that locally the stress may be somewhat heterogeneous with respect to the regional stress field. This precludes identifying the regional stress field from the sole inversion of such locally induced focal mechanisms.

However, when combined with HTPF normal stress measurements, focal mechanisms of induced seismicity can be beneficial in efficiently constraining the regional stress field. The fact that this integrated stress determination has yielded for the Le Mayet de Montagne site a principal stress component in the vertical direction, when this was not imposed *a priori* in the inversion, is taken as a proof of the effciency of the method.

This precise regional stress determination shows that the stress heterogeneities observed along the fault zones are fairly localized and leave many portions of the fault unperturbed as demonstrated by the many consistent focal mechanisms identified within the fault zones. These numerously consistent focal mechanisms have been advantageously utilized to map the interstitial pressure. This mapping has shown that locally the pore pressure may be considerably larger than the regional minimum principal stress magnitude. Yet, no large-scale hydraulic fracture has been identified, either from the surface tilts or from the flow characteristics (a hydraulic fracture should be associated with large fluid flow, when very little has been observed in practice). The cause of this metastable situation is probably to be found in the morphology of the fault zone. This suggests that, in natural faults, the pore pressure may reach values extensively larger than the regional minimum principal stress, without inducing hydraulic fracturing, and this for a reasonably long duration (more than fifteen days in the case of Le Mayet de Montagne).

Acknowledgements

This research was supported by the European Economic Communities Directorate General XII (contract EN3G-0051-F), by Programme Interdisciplinaire de Recherche Sur l'Énergie et les Matières premières (PIRSEM) from Centre National de la Reserche Scientifique and by Agence Française pour la Maitrise de l'énergie. This work benefited greatly from the assistance of B. Bert for his technical contribution in all field work. Y. Willeveau, O. Scotti and G. Rozières assisted in some of the HTPF stress determinations.

References

Bott, B. (1959), *The Mechanics of Oblique Slip Faulting*, Geol. Mag. *96* (2), 109–117.

Bruel, D., and Cornet F. H., *Force fluid through fractured reservoirs modelling*. In *Fractured and Jointed Rock Masses* (eds. N. G. W. Cook and L. Myer) (Lawrence Berkeley Lab. Report LBL-32379, 3, 1992) pp. 519–526.

COCHARD, A., and MADARIAGA, R. (1994), *Dynamic Faulting under Rate-dependent Friction*, Pure and Appl. Geophys *142* (3/4), 419–445.

CORNET, F. H., *Experimental investigation on forced fluid flow through a granite rock mass.* In *Fourth European Geothermal Update* (eds. K. Louwrier, E. Staroste, and J. Garnish) (Kluwer Academic Pub. Dordrecht, Holland 1989) pp. 189–204.

CORNET, F. H., *In situ stress heterogeneity identification with the HTPF tool. In Rock Mechanics, Proc. 33 rd US Symposium on Rock Mechanics* (eds. Tillerson and Wawersik) (Balkema, Rotterdam 1992) pp. 39–48.

CORNET, F. H., HOSANSKI, J. M., BERNAUDAT, F., and LEDOUX, E., *Shallow depth experimentation on the concept of energy extraction from deep hot dry rocks.* In *Hydraulic Fracturing and Geothermal Energy* (eds. S. Nemat-Nasser, H. Abe, and S. Hirakawa) (Martinus Nijhoff, The Hague 1982) pp. 385–403.

CORNET, F. H., and JULIEN, Ph. (1989), *Stress Determination from Hydraulic Test Data and Focal Mechanisms of Induced Seismicity*, Int. J. Rock Mechanics Min. Sci. and Geomech. Abs. *26* (3/4), 235–248.

CORNET, F. H., YIN J., and MARTEL L., *Stress heterogeneity and flow path in a granite rock mass.* In *Fractured and Jointed Rock Masses* (eds. N. G. W. Cook, and L. Myer) (Lawrence Berkeley Lab. Report LBL-32379, vol. 1, 1992) pp. 80–87.

CORNET, F. H., and SCOTTI, O. (1993), *Analysis of Induced Seismicity for Fault Zone Identification*, Int. J. Rock Mech. Min. Sci. and Geomech. Abs. *30* (7), 789–795.

DESROCHES, J., and CORNET, F. H., *Channelling stiffness effects on fluid percolation in jointed rocks.* In *Rock Joints* (eds. N. Barton, and O. Stephanson) (Balkema, Rotterdam 1990) pp. 527–534.

FEHLER, M. C. (1989), *Stress Control of Seismicity Patterns Observed during Hydraulic Fracturing Experiments at the Fenton Hill Hot Dry Rock Geothermal Energy Site, New Mexico*, Int. J. Rock Mech. Min. Sci. and Geomech Abs. *26*, (3/4) pp. 211–219.

GEPHART, J. W., and FORSYTH, D. W. (1984), *An Improved Method for Determining the Regional Stress Tensor Using Earthquake Focal Mechanism Data: Application to San Fernando Earthquake Sequence*, J. Geophys. Res. *89* (B11), 9305–9320.

HERERO, A., and BERNARD, P. (1994), *A Kinematic Self-similar Rupture Process for Earthquakes*, Bull. Seismol. Soc. Am. *84* (4), pp. 1216–1228.

HOUSE, L. (1987), *Locating Microearthquakes Induced by Hydraulic Fracturing in Crystalline Rock*, Geophys. Res. Lett. *14*, 919–921.

JULIEN, Ph., and CORNET, F. H. (1987), *Stress Determination from Aftershocks of the Campania-Lucania Earthquake of November 23, 1980*, Ann. Geophys. *5B* (3), pp. 289–300.

MCGARR, A. (1980), *Some Constraint on Levels of Shear Stress in the Crust from Observations and Theory*, J. Geophys. Res. *85* (B11), pp. 6231–6238.

MOSNIER, J., and CORNET, F. H., *Apparatus to provide an image of the wall of a borehole during a hydraulic fracturing experiment.* In *Fouth European Geothermal Update* (eds. K. Louwrier, E. Staroste, and J. Garnish) (Kluwer Academic Pub., Dordrecht 1989) pp. 205–212.

NIITSUMA, H., NAKATSUKA, K., TAKAHASHI, H., ABE, M., CHUBACHI, N., YOKOYAMA, H., and SATO, R., *In situ AE measurements of hydraulic fracturing at geothermal fields.* In *Hydraulic Fracturing and Geothermal Energy* (eds. S. Nemat-Nasser, H. Abe, and S. Hirakawa) (Martinus Niijhoff, The Hague 1982) pp. 227–241.

PEARSON, C. (1981), *The Relationship between Microseismicity and High Pore Pressure during Hydraulic Stimulation Experiments in Low Permeability Granite Rocks*, J. Geophys. Res. *86*, 7855–7864.

PINE, R. J., and BATCHELOR, A. S. (1984), *Downward Migration of Shearing in Jointed Rock during Hydraulic Fracturing*, Int. J. Rock Mechanics Min. Sci. and Geomech. Abs. *21*, 249–263.

RICE, J. (1993), *Spatio-temporal Complexity of Slip on a Fault*, J. Geophys. Res. *98* (B6), 9885–9907.

RIVEIRA, L., and CISTERNAS, A. (1990), *Stress Tensor and Fault Plane Solutions for a Population of Earthquakes*, Bull. Seismol. Soc. Am. *80* (3), 600–614.

ROBINSON, L. H., and HOLLAND, W. E., *Some Interpretation of pore fluid effects in rock failure.* In *Rock Mechanics—Theory and Practice, Proc. 11th Symp. on Rock Mech.* (ed. W. H. Somerton) (Soc. Min. Eng., Am. Ins. Min. Met. Pet. Eng., New York 1970) pp. 585–597.

SCOTTI, O., and CORNET, F. H. (1994a), *In situ Evidence for Fluid Induced Aseismic Slip Events Along Fault Zones*, Int. J. Rock Mech. Min. Sci. and Geomech. Abs. *31* (4), 347–358.

SCOTTI, O., and CORNET, F. H. (1994b), *In situ Stress Fields and Focal Mechanism Solutions in Central France*, Geophys. Res. Lett. *21* (22), 2345–2348.

TALEBI, S., and CORNET, F. H. (1987), *Analysis of the Microseismicity Induced by a Fluid Injection in a Granite Rock Mass*, Geophys. Res. Letts. *14* (3), 227–230.

TERZAGHI, K. (1945), *Stress Conditions for the Failure of Saturated Concrete and Rock*, Proc. Am. Soc. Test Mat. *45*, 777–801.

VASSEUR, G., ETCHECOPAR, A., and PHILIP, H. (1983), *Stress State Inferred from Multiple Focal Mechanisms*, Ann. Geophys. *1*, 291–297.

WALLACE, R. E. (1951), *Geometry of Shearing Stress and Relation to Faulting*, J. Geology *59*, 118–130.

YIN, J., *Détermination du Champ de Contrainte Régional à Partir de Mesures Hydrauliques et de Mécanismes au Foyer de Microséismes Induits*, Thèse de Doctorat de l'Univ. Paris VII et de l'Inst. Phys. Globe de Paris 1994.

YIN, J., and CORNET, F. H. (1994), *Integrated Stress Determination by Joint Inversion of Hydraulic Tests and Focal Mechanisms*, Geophys. Res. Lett. 29 (24) 2645–2648.

Received November 18, 1994, revised March 31, 1995, accepted April 10, 1995.

3. Two examples of stress determination from focal mechanisms inversion

3.3 The Soultz Geothermal experiment.

This example has been discussed in two papers :

Cornet F.H., J. Helm, H. Poitrenaud and A. Etchecopar, 1997; Seismic and Aseismic Slips Induced by Large Scale Fluid Injections; PAGEOPH ,vol. 150, nb 3/4, pp 563-583.

Cornet F.H., 2000, Comments on large scale in situ permeability tensor of rocks from induced microseismicity by S.A. Shapiro, P. Audigan and J.J. Royer; Geophys. Jou. Int. , vol. 140, pp 465-469.

These notes are copies of the transparencies shown during the lecture, with some additional comments, when deemed necessary.

At Soultz, some 20 km to the north of Strasbourg, at the border between Germany and France, a site is being developed for testing the possibility of exploiting the geothermal energy of hot rocks with no or too small natural permeability. The experiment reported here corresponds to the first large-scale water injection undertaken for developing an efficient downhole heat exchanger in the granite that is underlain by about 1400 m of sedimentary cover.

The injection was conducted in a 600-m long open-hole section of well GPK1. During injection, microseimicity was monitored with two networks:

1. a downhole network of 3 3-components accelerometers and a hydrophone, all located in the granite
2. a surface network of 6 3-components stations (LANF, AUF, SCH, HOFF, SRBF, KHLa) and 8 1-component sensors.

Injection proceeded at constant flow rate, with incrementation of the flow rate every other day, with a total injected volume of 25 000 m^3. The pressure stabilized once the flow rate reached 24 l/s, at about 9.2 mPa.

The European Hot Dry Rock Experiment at Soultz (Fr.)

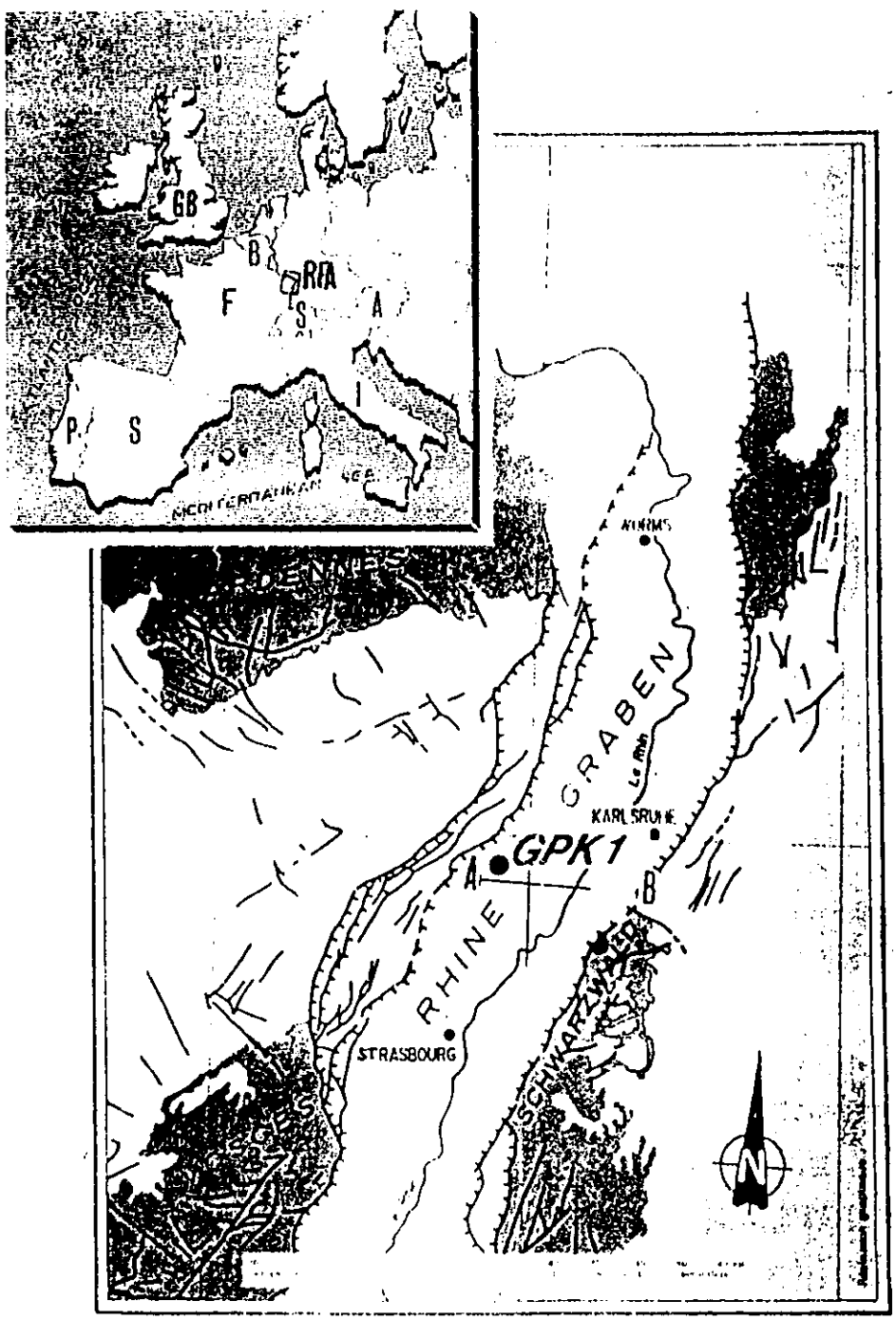

Figure 1a

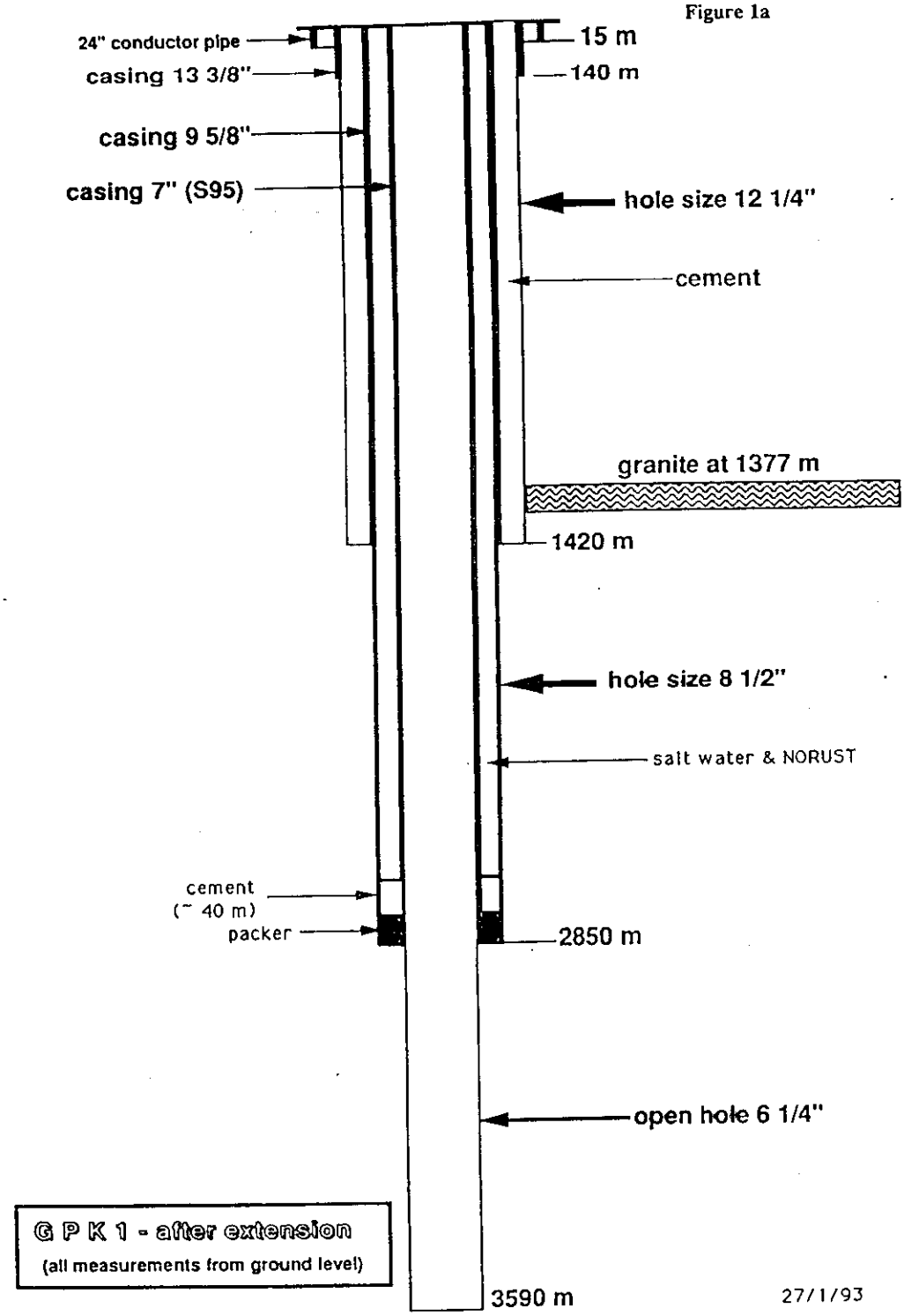

12-b

Seismic network deployed around the Soultz-sous-Fore site July-November 1993

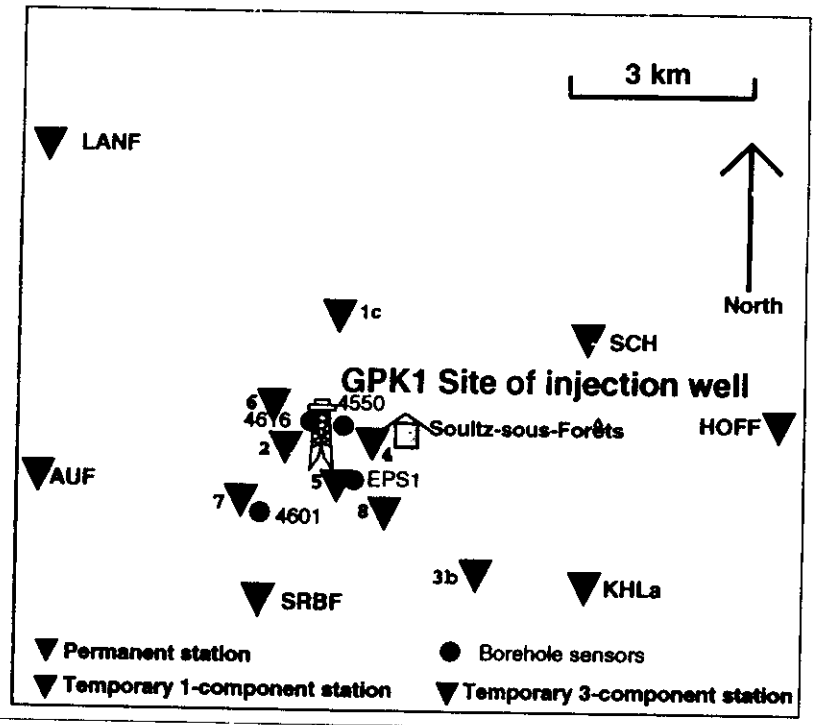

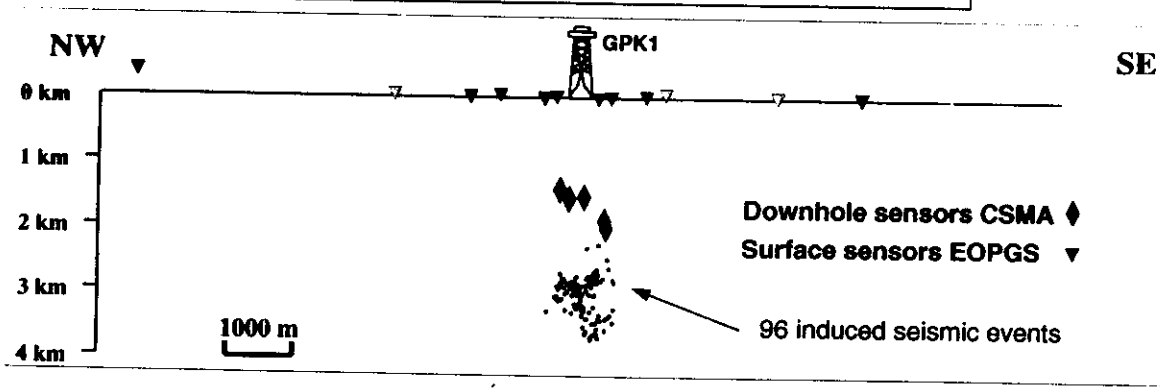

Note: i) Much larger angular opening of the surface network compared to the downhole network (good for focal mechanisms)

ii) Surface stations at greater epicentral distances (and smaller gains) so no problems with record saturation for large events (good for event magnitude determinations)

iii) Closer proximity of downhole sensors to micro seismicity

12 - C

3.2.1 Induced seismicity and rock mass failure

At the same time as pressure stabilized, induced seismicity started migrating upward and, at the same time, flow losses got concentrated in the upper 120 m of the well. Interestingly, while the downhole seismic network recorded more than 12 000 events, the surface network recorded only 166 events. The horizontal projection of microseismic events detected with the downhole network show a clear difference in orientation of the microseismic cloud. It is North South between 2800 and 2900 m but inclined about 30 ° to the west below 2900 m.

The orientation of principal stress directions is well constrained by the orientation of tensile failures at the borehole wall (mostly thermal fractures but also hydraulic fractures). It is found that the vertical component is principal (clear vertical fractures) and that the maximum horizontal principal stress is about North South

It is argued that this change in orientation of the seismic cloud reflects a change in the failure process of the rock mass : joint opening nearly perpendicularly to the minimum principal stress direction around between 2800 and 2900 m, shear failure along preexisting planes below 2900 m. However, the preexisting fractures being sheared are organized so as to yield a global failure of the rock mass inclined about 30 ° to the maximum principal stress.

It is concluded that the front of migration of induced seismicity is linked to the failure process of the rock mass and not to the natural permeability. This failure process requires an overpressure of about 5 mPa so that the rock mass may be considered to be naturally in its elastic domain.

Present work is in progress concerning the interpretation of the 9.3 mPa stabilization pressure observed during injection. When thermal stresses induced by the cooling of the rock in the vicinity of the well are taken into account, it can be shown that the stabilization pressure is about 4 to 5 mPa below the unperturbed far-field minimum principal stress.

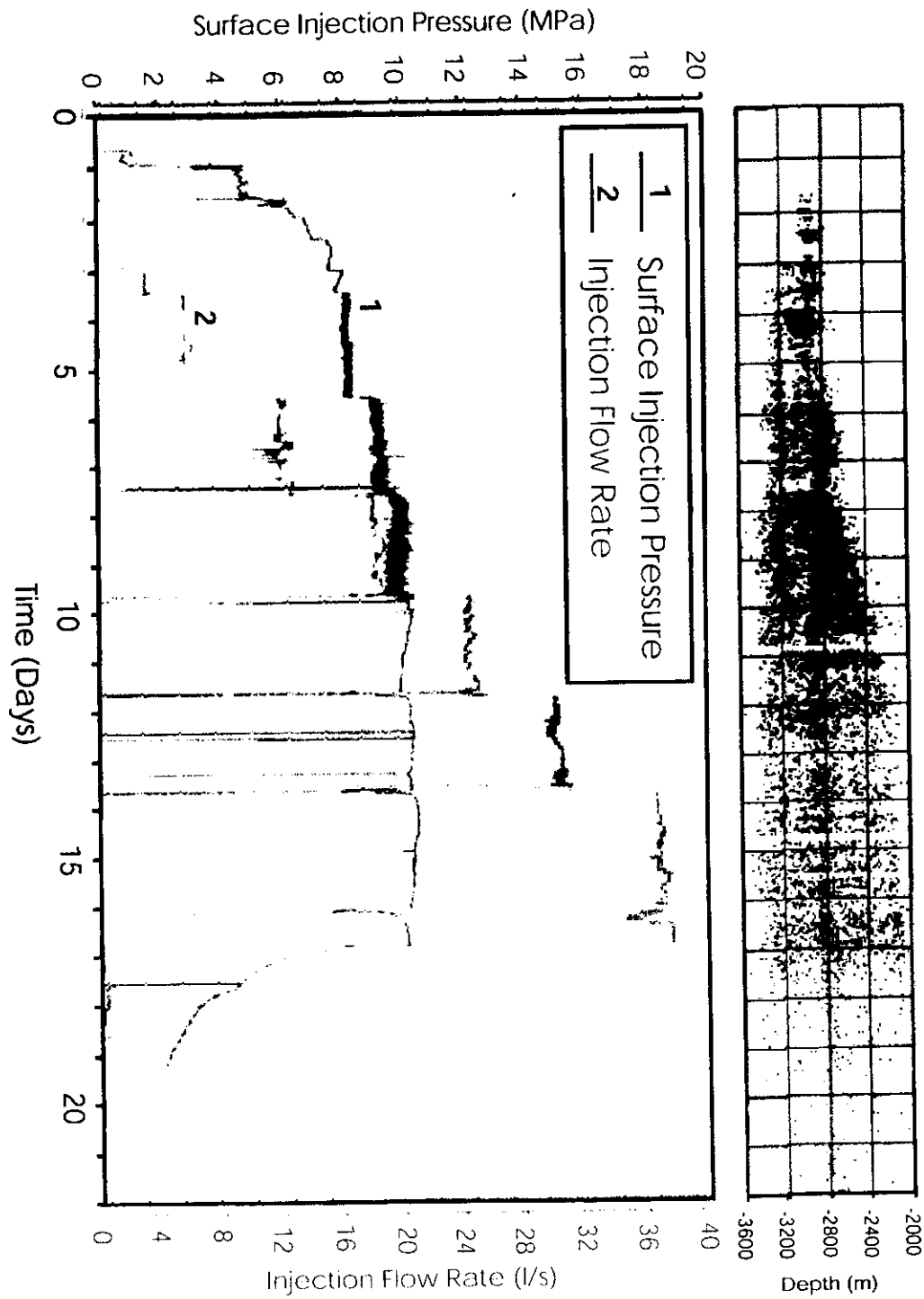
Surface Injection Pressure (MPa)
0
2
4
6
8
10
12
14
16
18
20
1
2
1 Surface Injection Pressure
2 Injection Flow Rate
Time (Days)
0
5
10
15
20
Injection Flow Rate (l/s)
0
4
8
12
16
20
24
28
32
36
40
Depth (m)
-2000
-2400
-2800
-3200
-3600

13-a

Spinner logs run during Injection

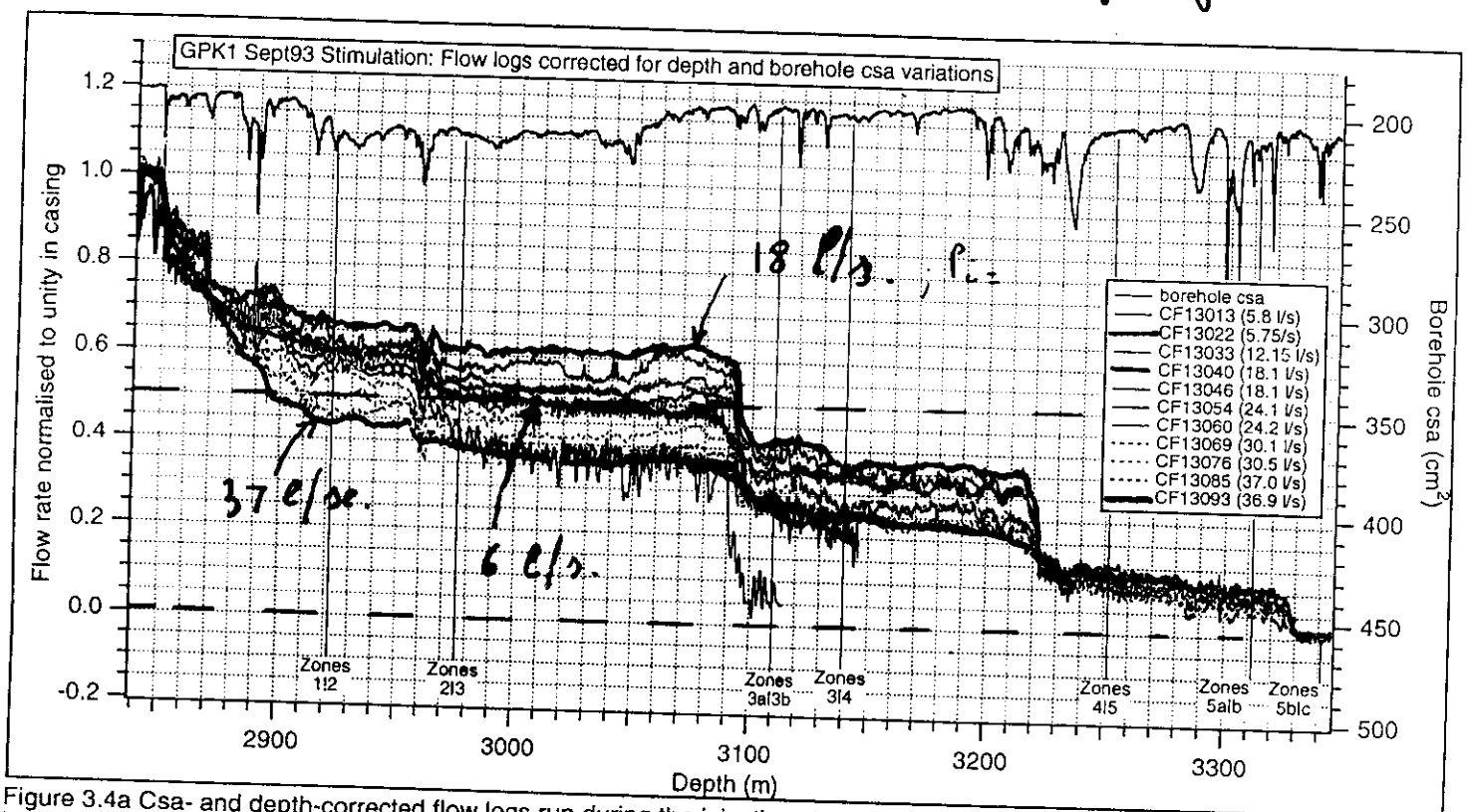

Figure 3.4a Csa- and depth-corrected flow logs run during the injection phase of the 93Sep01 test performed on GPK1. The lower part of the open hole section had been sanded-off. The cross-sectional area log is shown above. The flow rates listed in the caption are estimates taken at the time of the logs have been corrected for estimated leakage at the riser.

Variation with time of flow losses in borehole (doted curve) and depth distribution of seismicity (continuous curve)

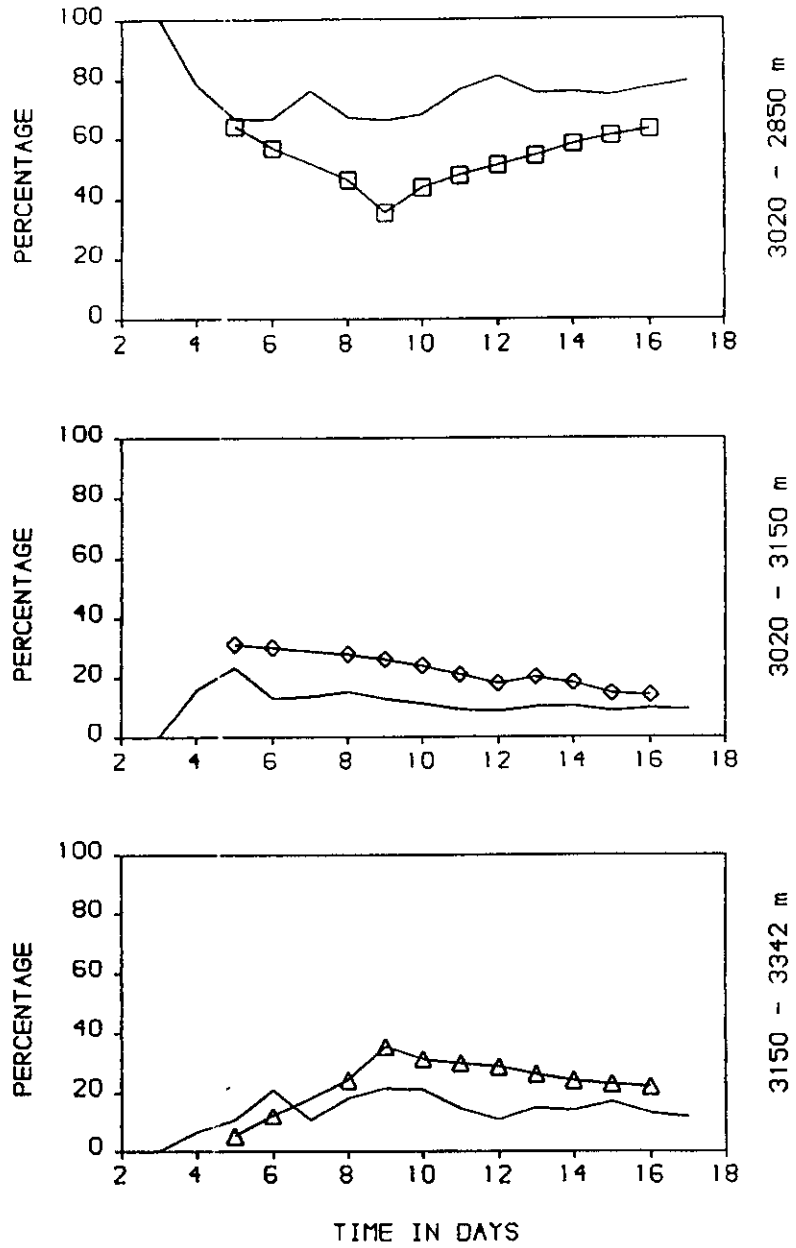

Source Magnitudes

166 events recorded on surface network
about 20 000 on downhole network

Magnitudes determined from the average of the duration of the signal recorded on the 3 nearest stations.

Magnitude determination scaled with natural signals observed simultaneously on local and regional network.

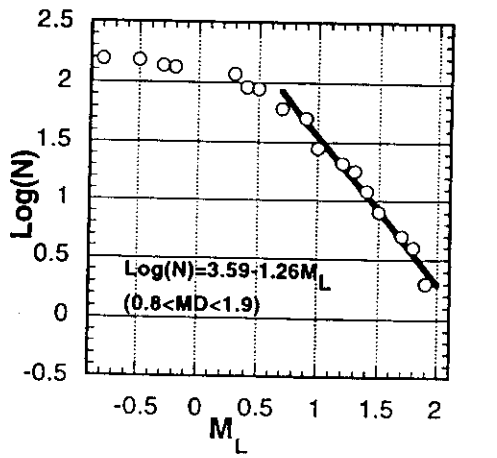

Frequency - Magnitude Relationship
(according to J. Helm, 1996)

13-e

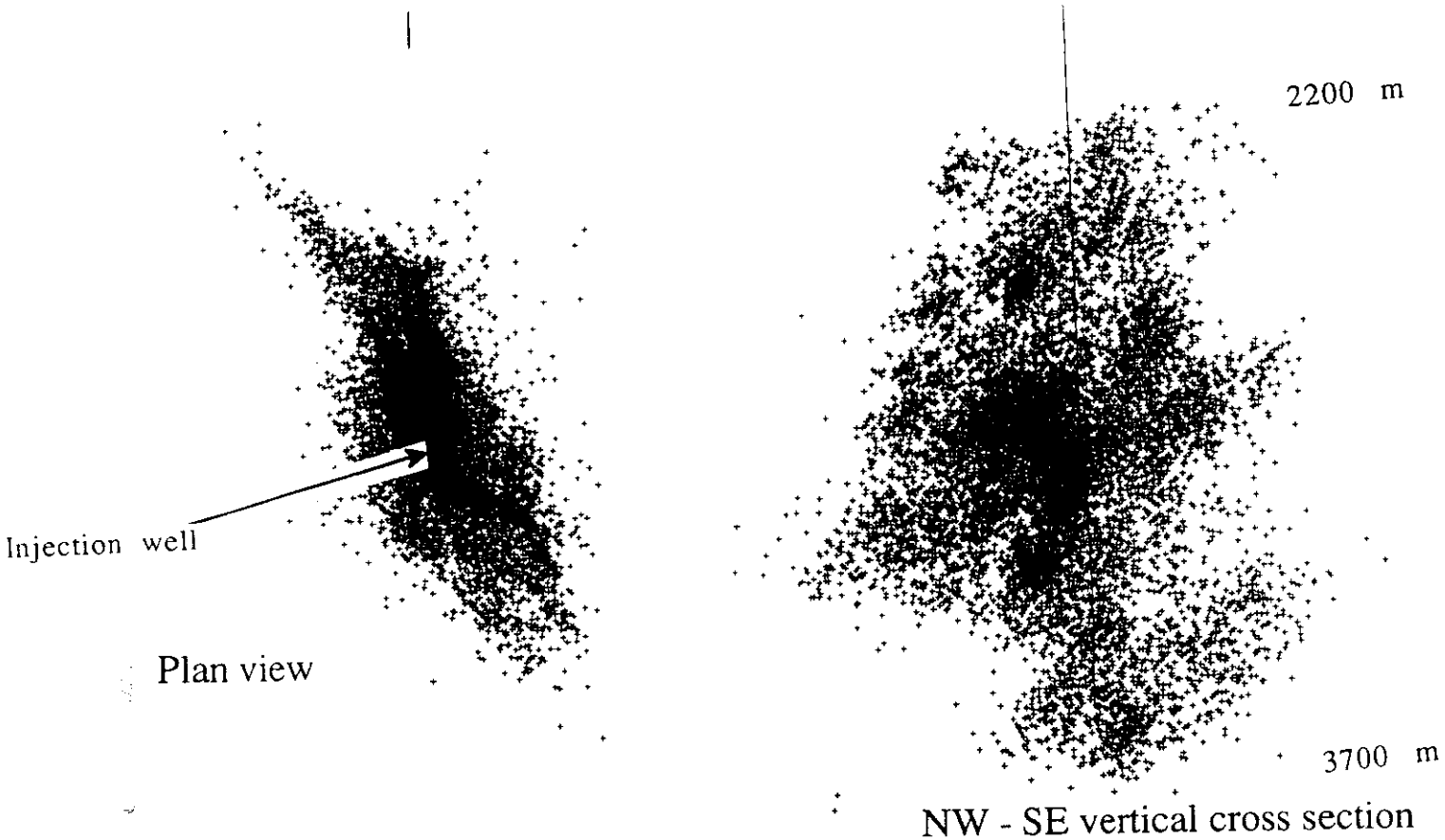

Location of induced seismicity

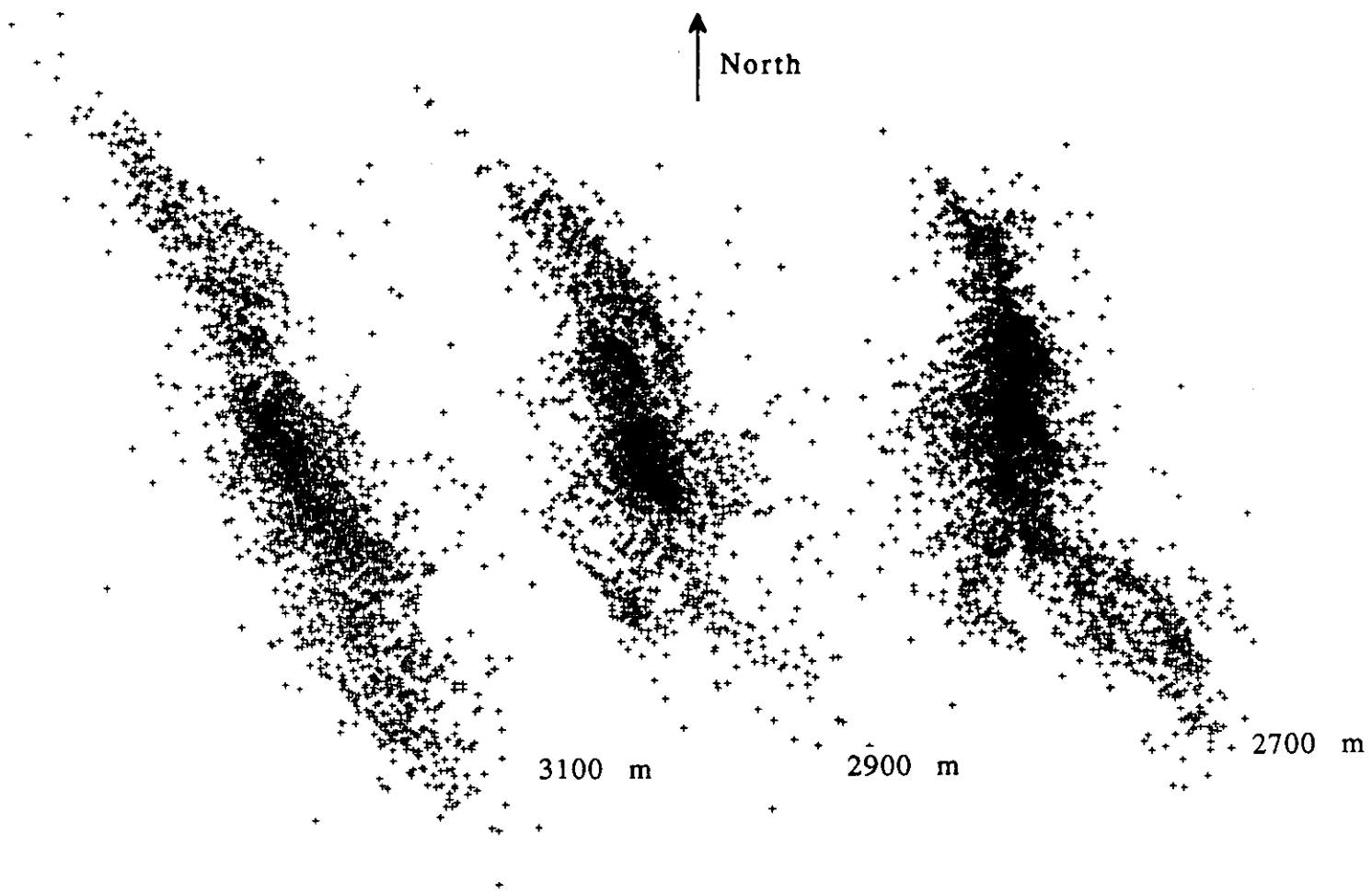
North
3100 m
2900 m
2700 m

3.2.2 On the significance of Shear wave velocity anisotropy as compared to focal mechanisms inversion for the stress field determination

The downhole seismic sensors have been used to investigate anisotropy by analyzing the polarization direction of shear waves and their rotation with time. For both stations considered for this analysis (the third one is not amenable for this investigation because of local site effects) results show a fast north south direction for the first one, a fast direction N 15 ° E for the second one. For this second station, very close to the sediment interface, local structural effects may explain the rotation.

The inversion of focal mechanisms of events observed with the surface network yield a direction N 124° E, i.e. about 30° to the known orientation of the maximum principal stress.

It is concluded that, as in Le Mayet de Montagne, the inversion focal mechanisms taken alone does not yield the correct principal stress directions.

S wave polarization

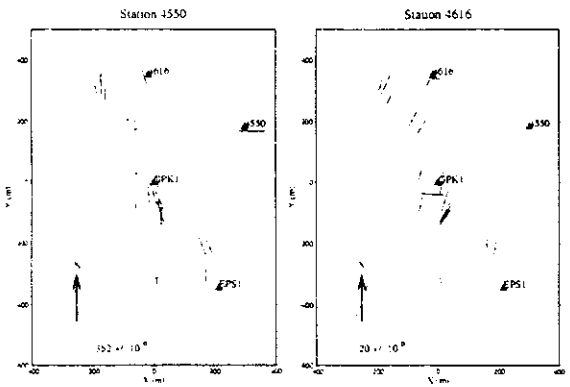

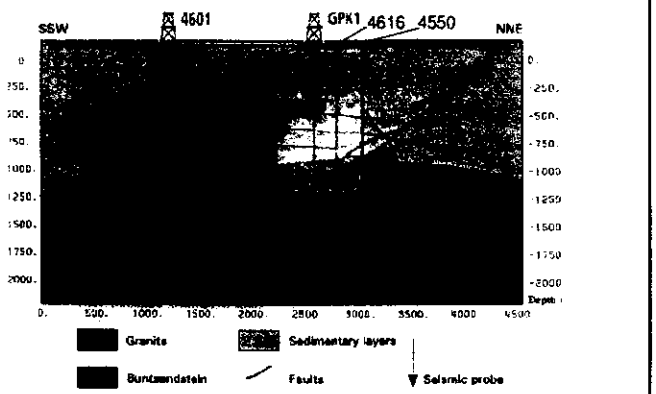

- S wave splitting
  ⇐ hexagonal anisotropy with a N-S horizontal symmetry axis, consistent with σ_H

- Stress rotation
  ⇐ topography of the sediment-granite boundary

Location and focal mechanism diagram of 10 induced events recorded during fluid injections.

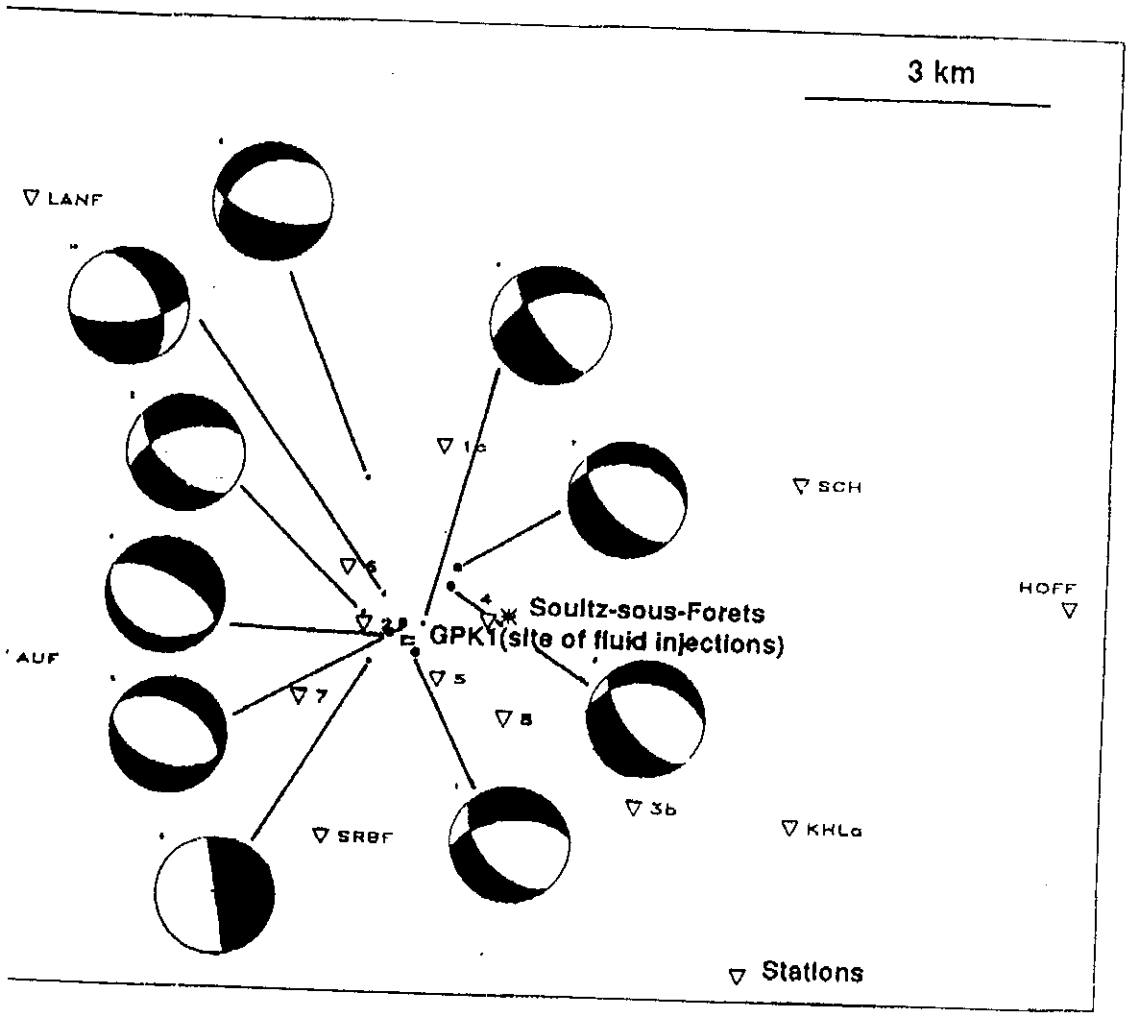

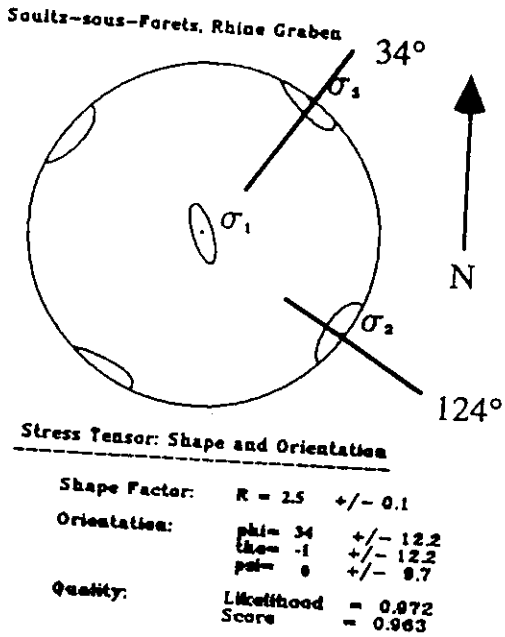

Figure 6.9 Final stress inversion of all 96 events located by CSMA, using EOPGS polarities (fixed and mobile surface stations)

3.2.3 On the role of aseismic slip and its influence on the stress field

Ultrasonic imaging logs may be used to measuring shear displacements which have occurred along preexisting weakness planes, provided these shear displacements are lager than about 4 mm (the resolution of the method). These measurements are based on travel time readings that provide direct measurements of the distance between the tool and the borehole. These data are taken to advantage for reconstructing the exact borehole geometry if it is assumed hat the tool has not moved during a complete rotation cycle (one rotation per second, 180 travel time readings with 2 ^{o} azimuthal increments for each rotation cycle).

Slip along six different fractures has been measured. It is observed that the magnitude of these slip motions is much larger than the amount, which can be determined from seismic data. Even if all events were concentrated on one single plane would the displacements still be to large. It is concluded that these shear motions had some significant non-seismic component.

Further, the orientations of all slip vectors are not consistent with a unique stress tensor. It is concluded that shear induced by the injection has modified progressively the stress field, so that inversion of all observed focal mechanisms is not warranted.

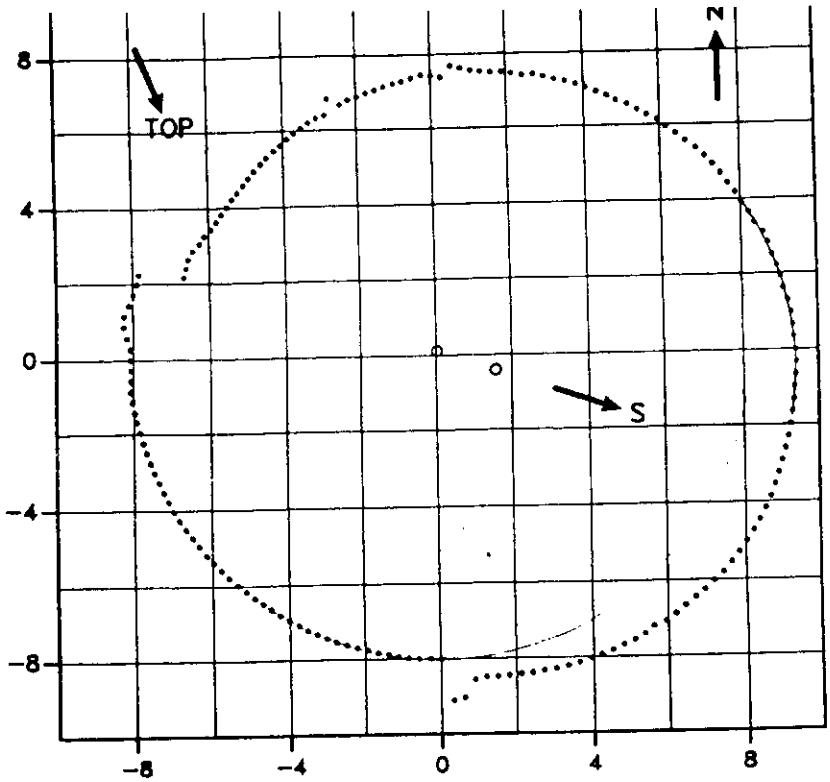

Schlumberger

HSVIEW 001E02
29-JUN-94 10:02:30

APRES
p = 15

Depth	:	2867.203 m
Hole deviation	:	5.6 deg
Hole azimuth	:	158.3 deg
Slip	:	108.7 deg
	:	130.3 deg
	:	1.3 cm

Data Points
Segment 1 radius = 8.1
Segment 1 continued
Segment 2 radius = 7.

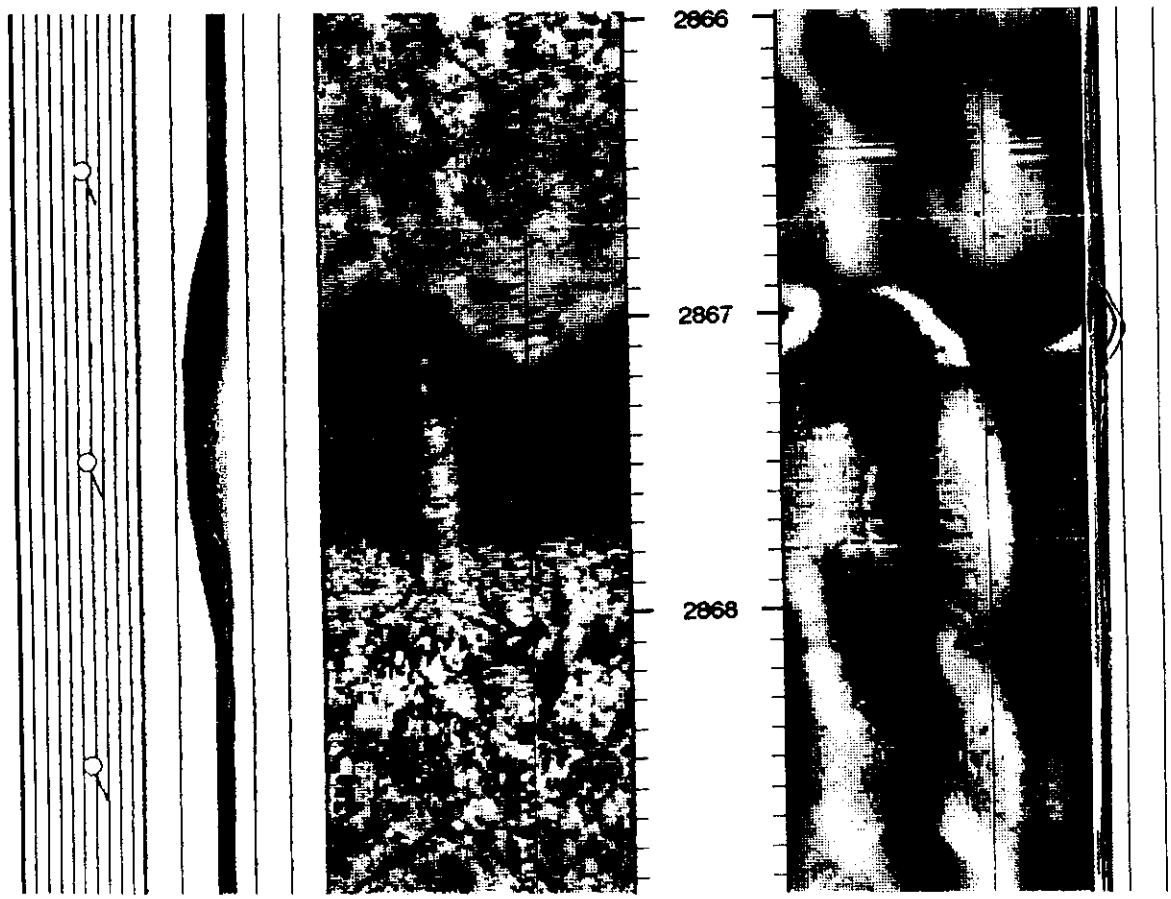

15.a

Determination of slip vector from BHTV observations

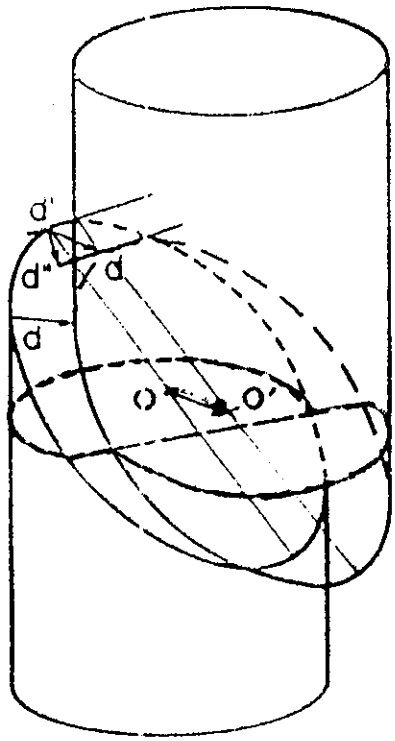

Borehole geometry result from shear displacement along existing fracture (general case):

d = Displacement
d' = Strike component
d" = Dip component

Results from slip motions measurements

slip vectors could been measured for 6 different fractures :

Fracture depth	slip amplitudes
2867 m	2.2 cm
2887 m	0.85 cm
2925 m	4.7 cm
2966 m	4.3 cm
2973 m	0.4 cm
2976 m	0.8 cm

Slip directions not consistent with one unique stress tensor

Some orders of Magnitude from elastostatics

For a pure shear motion over a circular crack :

$$\Delta\sigma = 7\Pi/16 * G * D/a$$

where

$\Delta\sigma$ = stress drop associated with slippage
G = shear modulus = $2\ 10^4$ Mpa
D = dislocation magnitude = 4.7 cm
a = radius of circular crack.

But, at 2900 m , $\sigma 3 \cong 42 \pm 5$ Mpa; $\sigma 1 \cong 77 \pm 2$ Mpa
so that $\Delta\sigma \leq 18$ Mpa .

Accordingly : if $\Delta\sigma = 18$ Mpa, a = 60 m;
if $\Delta\sigma = 9$ Mpa, a = 120 m.

Also: seismic moment M_0 is :

$$M_0 = G * S * D = 16/7 * \Delta\sigma * a^3$$

so, if $\Delta\sigma = 9$ Mpa, then $M_0 = 3.6\ 10^{20}$ dyne.cm
if $\Delta\sigma = 18$ Mpa, then $M_0 = 8.9\ 10^{19}$ dyne.cm

But, according to Majer and McEvilly (1979) for the Geysers, and to Pearson (1982) for the Fenton Hill HDR site :

$$\log M_0 \cong 0.8\ M + 17$$

where M is magnitude of seismic event.

Accordingly, a 4.7 cm seismic slip motion should yield a magnitude of the order of 4. (between 3.7 and 4.3, depending on hypothesis)

Discussion

If $M = 1.8$

then $M_0 \cong 3\ 10^{18}$
and $a \cong 24$ m if $\Delta\sigma \cong 9$ Mpa

If $M = 1.0$

then $M_0 \cong 6.3\ 10^{17}$
and $a \cong 15$ m if $\Delta\sigma \cong 9$ Mpa

Accordingly, a 4.7 cm slip motion requires 16 magnitude 1.8 events or 64 magnitude 1.0 events.

Given the observation that all events with magnitude larger than 1. 0 are not located near the injection well, it is concluded that all the elastic energy radiated by the seismic activity cannot account for observed displacements.

Conclusion

The fluid injection has induced non seismic slip motions.

3.3 Induced seismicity along the Philippine Faults on the Island of Leyte:

The work presented in this section has been partly published :

Prioul R., F.H. Cornet, C. Dorbath, L. Dorbath, M. Ogena & E. Ramos, 2000, An induced seismicity experiment across a creeping segment of the Philippine Fault, Jou. Geophys. Res. , vol. 105, (June), p 13 595.

The material on anisotropy and focal mechanism inversion can partly be found in R Prioul Ph. D. Thesis (Sept. 2000, IPGP) : Apport de la sismicite induite a l'etude du comportement d'un segment d'un grand decrochement actif – La Faille Philippine. A publication is in preparation.

The Philippine fault is an active senestral strike slip fault, about 1200 km long, which has given rise to numerous earthquakes with magnitude larger than 7. However, in it central part, in Masbate and Leyte Islands, GPS measurements have shown displacements up to 3.5 cm per year, with only a very limited seismic activity. At the Tongonan geothermal site, on Leyte Island, the fault separates in two segments, with relative displacement of about 2.5 cm/y.

A large geothermal field located to the East of the fault has resulted in many wells being drilled, some for production, some for reinjection of brines produced at the plants. Many wells have been drilled for reinjecting the brines, either in between the two fault segments or through the faults themselves. These wells have revealed to be very impervious. They have also demonstrated that temperature west of the central fault segment drops rapidly from the 300 $^{\circ}$ C value observed within the reservoir, about 1500m below ground level.

A large injection experiment, comparable to that conducted at Soultz, has been performed in well MG2RD which crosses the central fault segment around 1600 m below ground level. The well is cased down to 700 m and then lined with a slotted liner. A total volume of 36 000 m^3 has been injected at incremental flow rates, while induced microseismicity was monitored with a surface network.

For a period 18 months (February 1996, July 1997) the background microseismicity associated with the geothermal exploitation has been monitored with a 7 one-component (vertical) stations network. An additional 7 one-component network as well as four 3-componenets stations was installed for two two-month periods (October-November 1996 and June-July 1997). The injection experiment in MG2RD was conducted in June-July 1997 but injections linked to the reservoir exploitation occurred routinely during the duration of the recording.

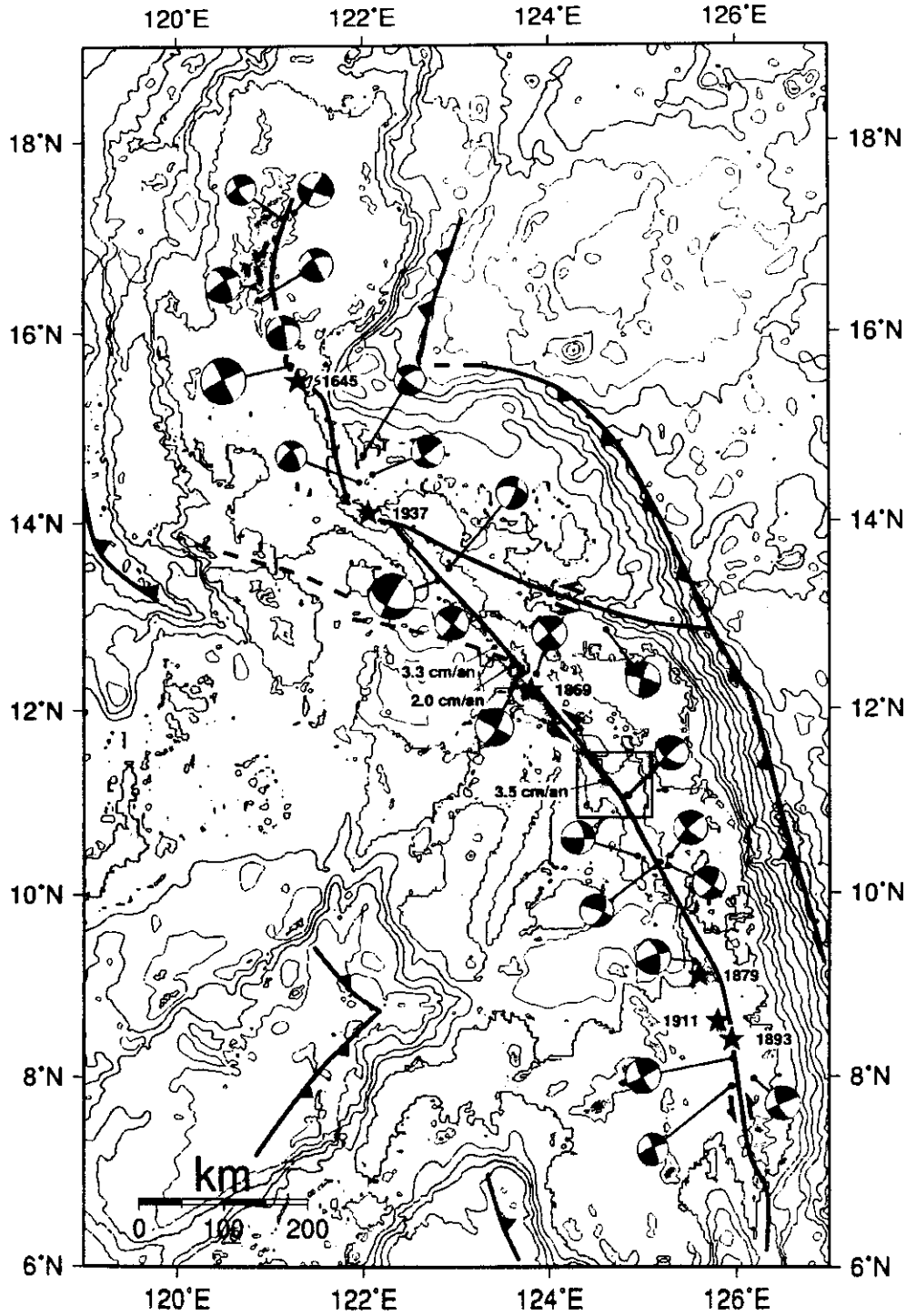
120°E
122°E
124°E
126°E
18°N
16°N
14°N
12°N
10°N
8°N
6°N
1645
1937
1869
1879
1911
1893
3.3 cm/an
2.0 cm/an
3.5 cm/an
km
0
100
200

16 - a

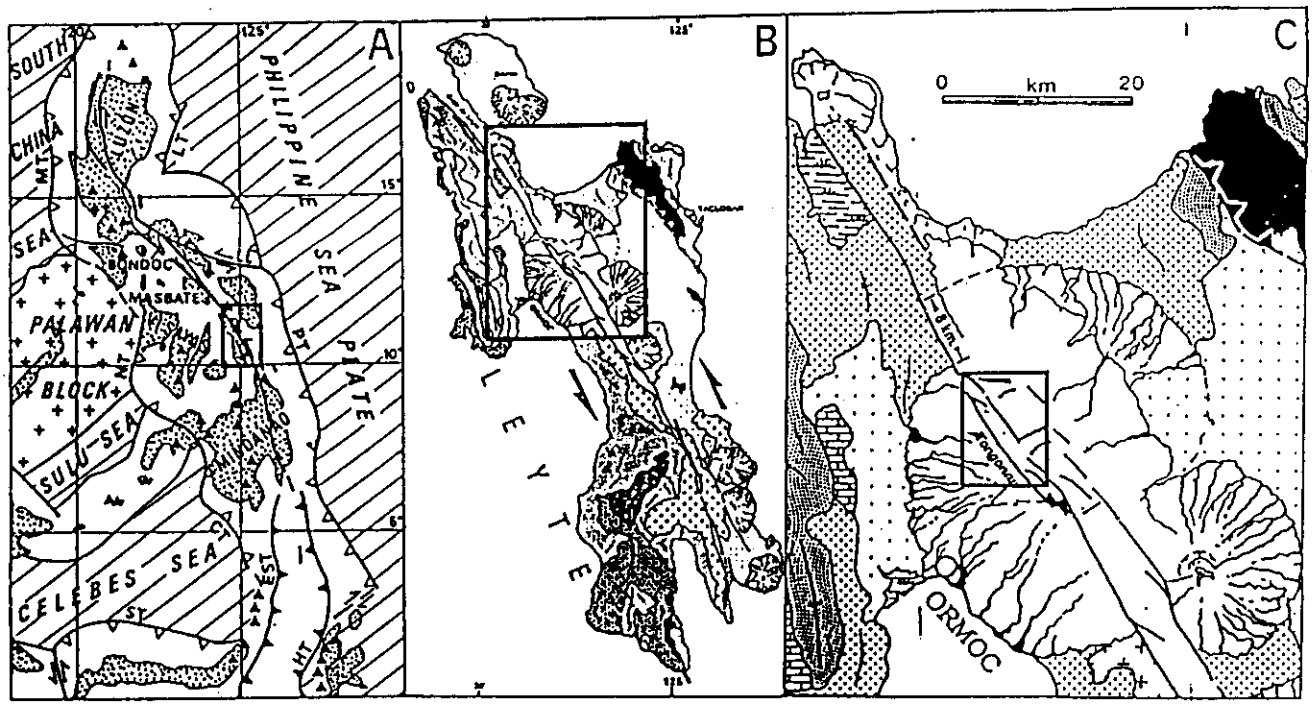

Fig. 1.- Tectonic setting of the Tongonan Geothermal field
(A) Geodynamical framework of the Philippines; volcano as triangle. (B) Geological sketch of Leyte (location in A) showing the geometry of the Philippine Fault and the main volcanoes. (C) Geometry of the Philippine Fault in northern Leyte and location of the Tongonan Geothermal field and of the geodetic network (inset). The displacement of the volcanic cone, 8 km since about 500 000 years, indicated an average displacement rate of about 2 cm/y.

Déplacements GPS

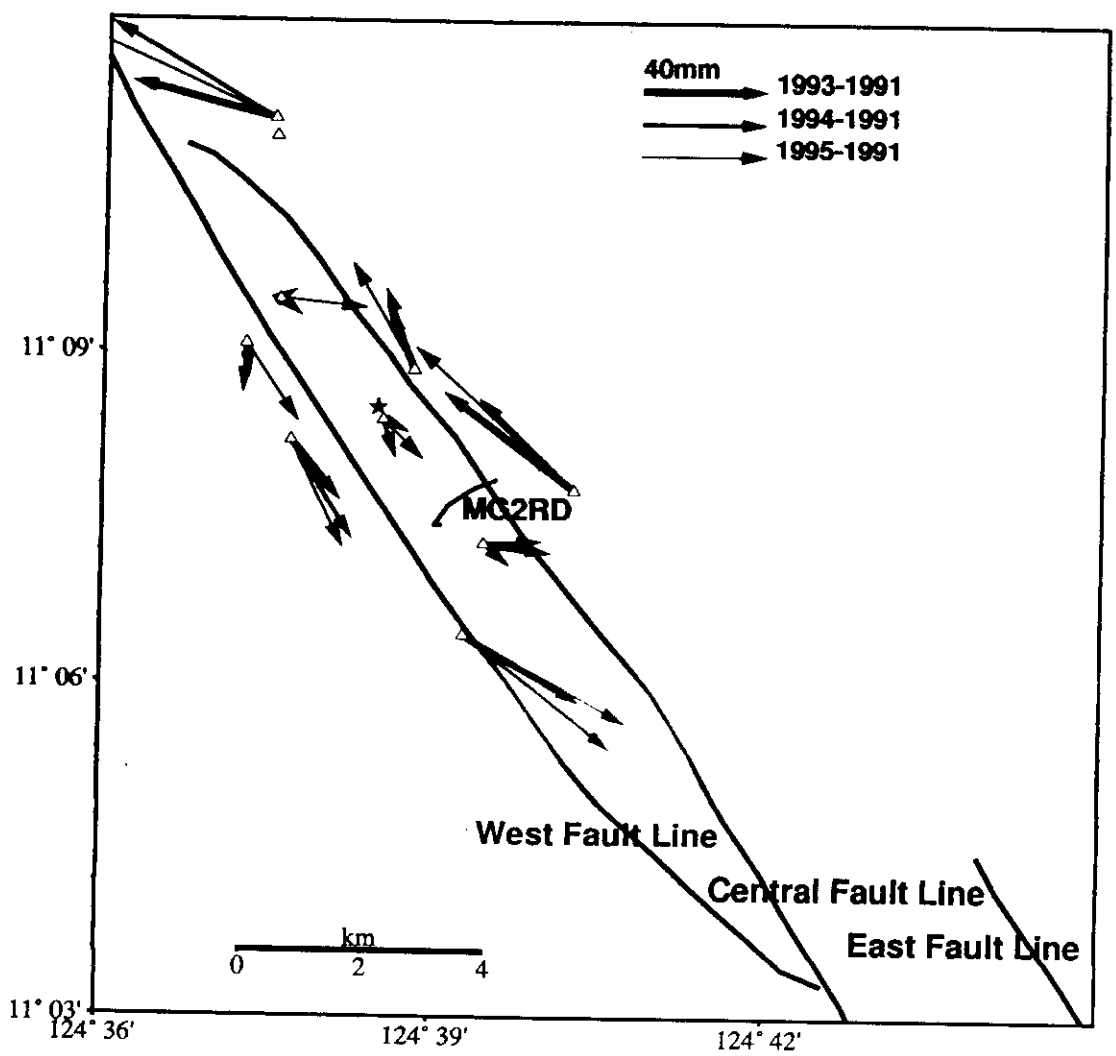

(Duquesnoy, 1997)

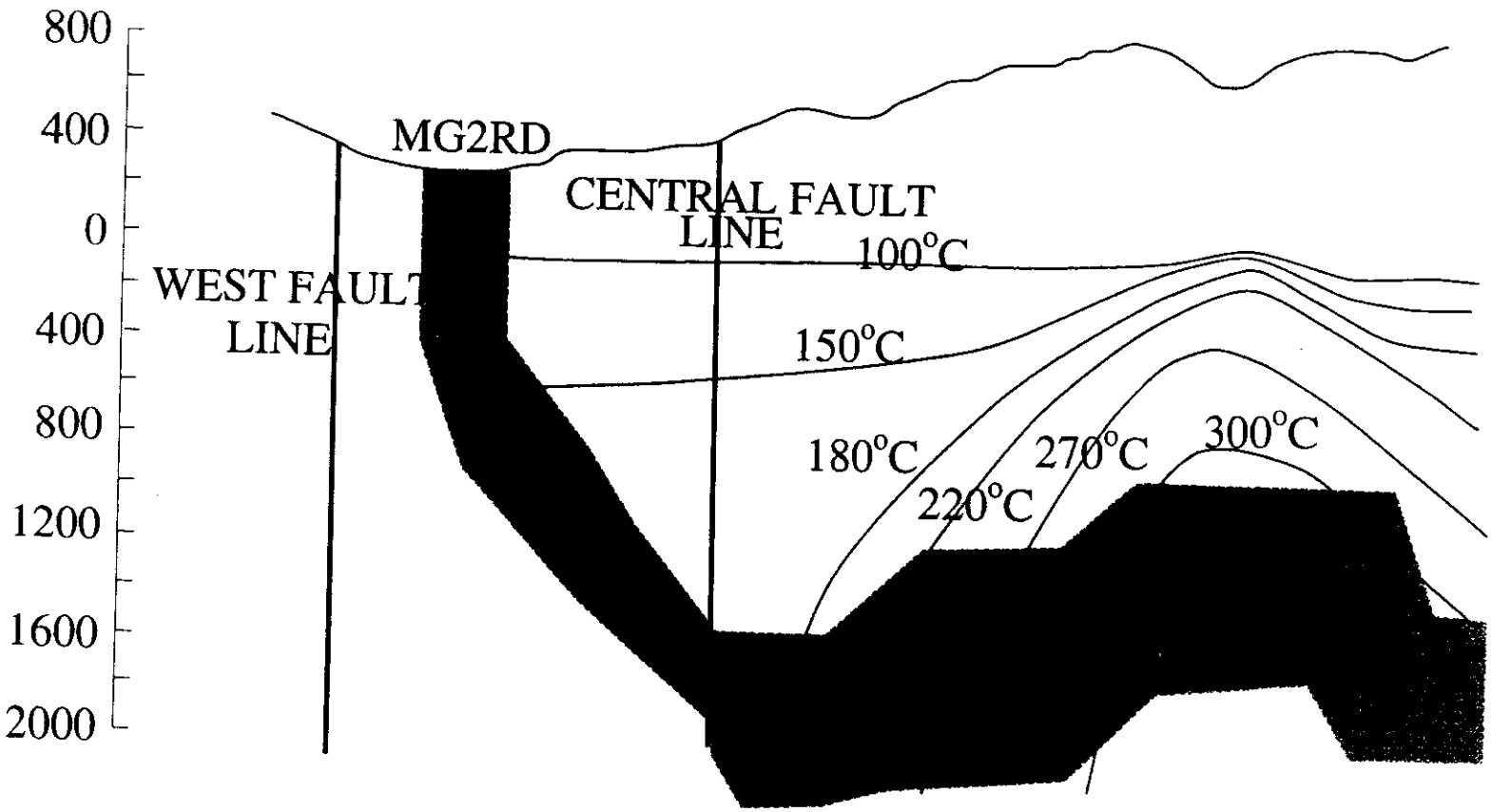
800
400
0
400
800
1200
1600
2000
MG2RD
CENTRAL FAULT LINE
WEST FAULT LINE
100°C
150°C
180°C
220°C
270°C
300°C

Expérience d'injection

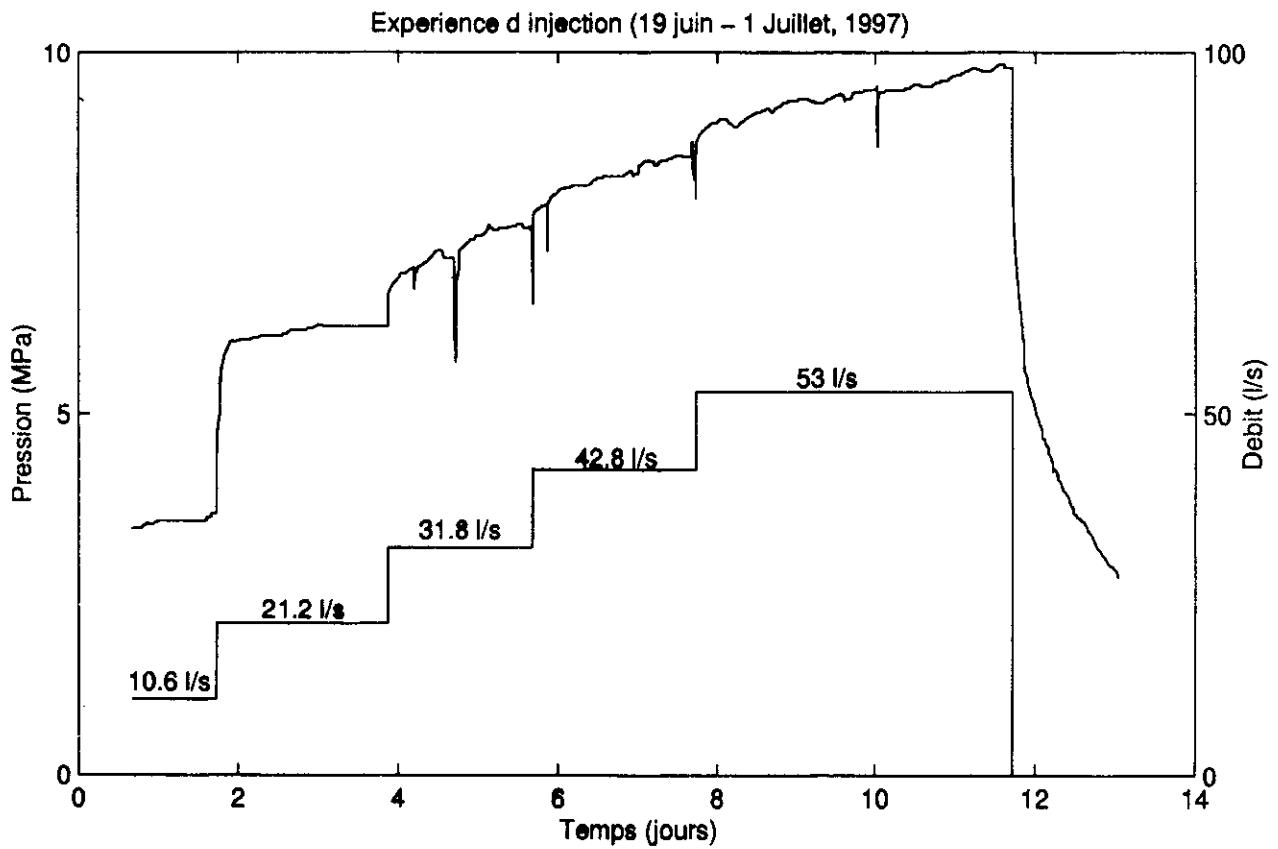

Tongonan geothermal field

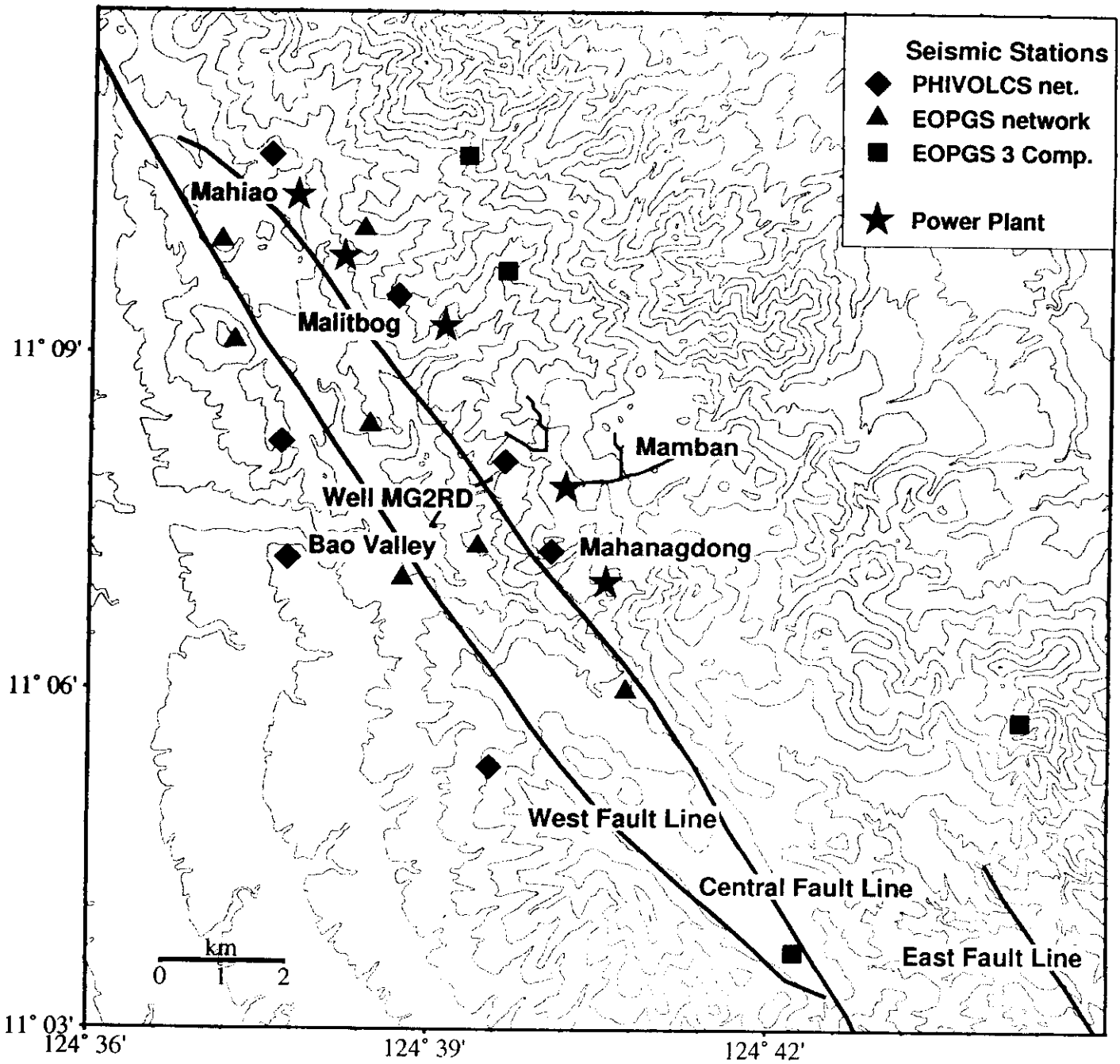

16-f

3.3.1 On the lack of permeability within this creeping segment of the fault

While no event was observed in the vicinity of MG2RD before the beginning of injection, microseismic events were soon observed after the beginning of injection but disappeared in the vicinity of the well when injection stopped. None of the events is located on the fault, but all occurred within the reservoir. It must be mentioned that some injection was started in neighboring wells, for operational reasons, at the end of our injection. This explains the seismicity observed away from well MG2RD, when injection stops in MG2RD.

Flow and thermal logs run in the well during injection down to the intersection with the fault show that no flow was lost in the upper section of the well, above the intersection with the fault. Given the size of the activated seismic zone and the complete lack of seismicity along the fault, it is concluded that the fault is impervious. This is corroborated by the fact that, before the stimulation was undertaken the borehole injectivity index was very low and that ground temperature drops drastically across the fault.

Hence, it may be anticipated that the fault is filled by impervious gauge, although no information is available yet on the nature of the fault gauge.

Location of seismicity has been determined simultaneously to inverting for the velocity field according to Thurber's method (Thurber C., 1983, Earthquake location and three-dimensional crustal structure in the Coyote lake area, central California, jou. Geophys. Res., vol. 88, pp 8226-8236)

This insures that ray paths are properly determined for focal mechanism determinations.

Injection experiment results

Induced seismicity

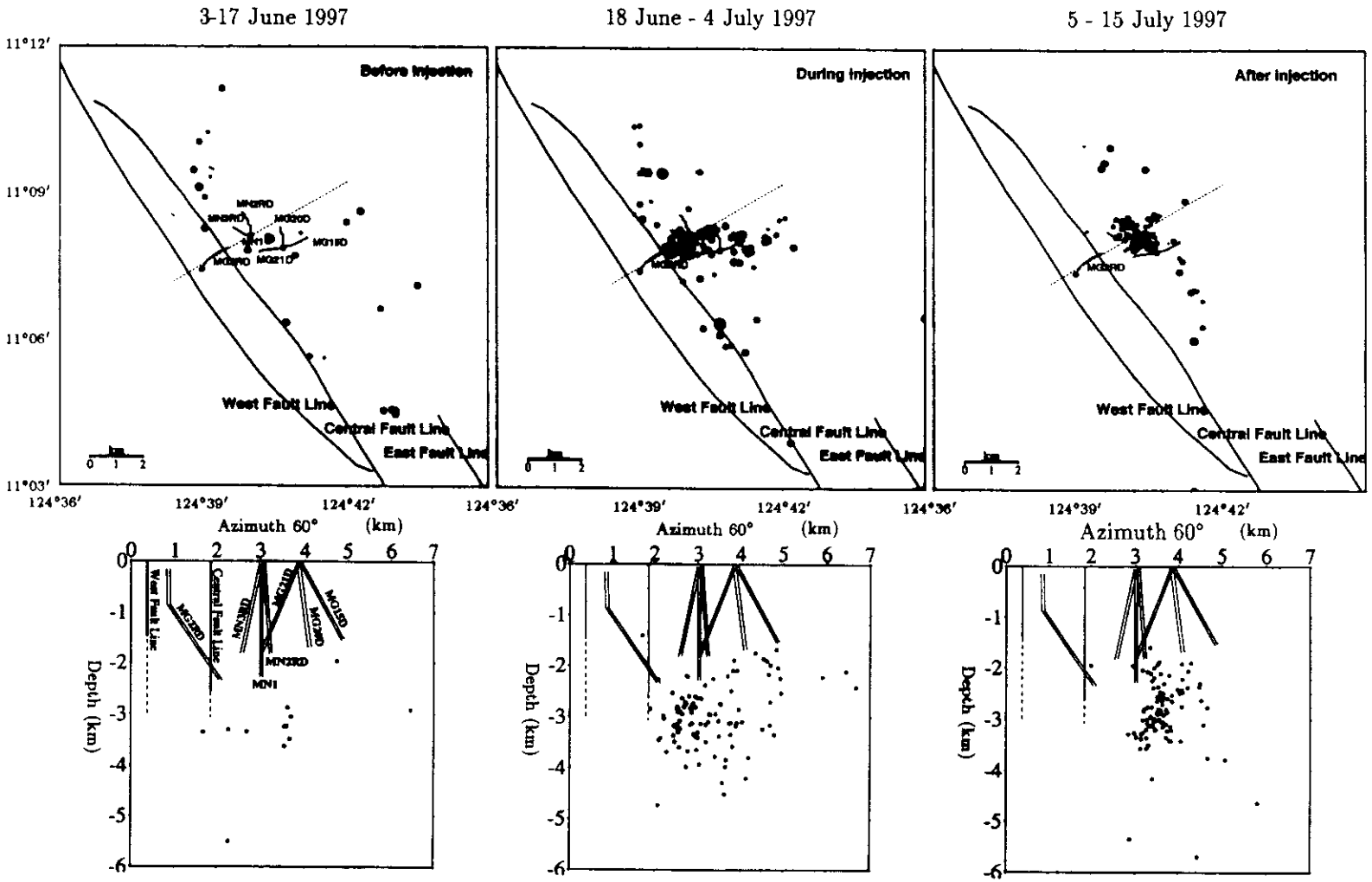

Seismic Tomography

Objective :
Determine simultaneously the location of microseismic events and the velocity field

Method (after Thurber, 1983) :
The method is based on a least squares minimization technique which includes perturbations of the initial apriori velocity model together with perturbation of the initial location determination according to the initial apriori velocity model :

$$R_{ij} = \Delta t_{0i} + \partial t_{ij}/\partial x_i \, \Delta x_i + \partial t_{ij}/\partial y_i \, \Delta y_i + \partial t_{ij}/\partial z_i \, \Delta z_i + \Sigma^{N}_{n=1} \, \partial t_{ij}/\partial V_n \, \Delta V_n$$

Where :

R_{ij} is the arrival time residual at station j for event i,

Δt_{0i} , Δx_i , Δy_i , Δz_i are perturbations to the hypocentral parameters for event i,

$\partial t_{ij}/\partial x_i$, $\partial t_{ij}/\partial y_i$, $\partial t_{ij}/\partial z_i$, $\partial t_{ij}/\partial V_n$ are partial derivative of the arrival time at station j for event i with respect to microseismic event coordinates and velocity parameters.

Arrival times are calculated using an approximate ray tracing method.

Initialization of the algorithm starts with a location determination based on a simple one-dimensional layered model.

Injection experiment results

P velocity models - before and during injection -

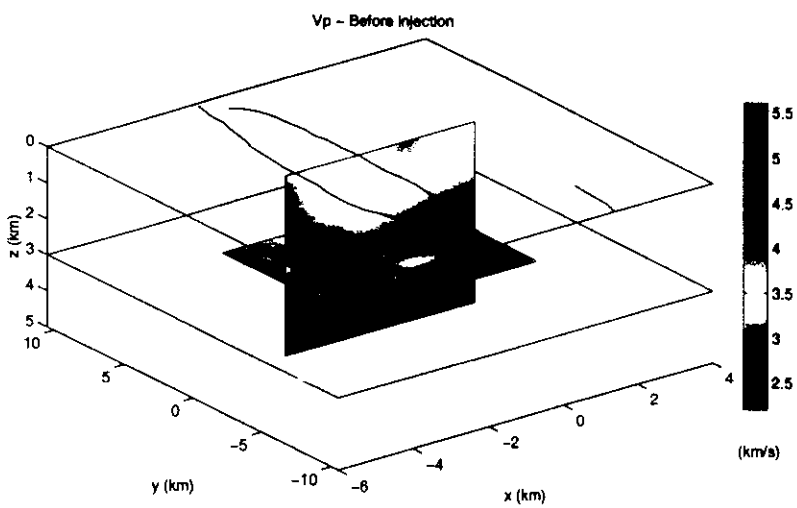

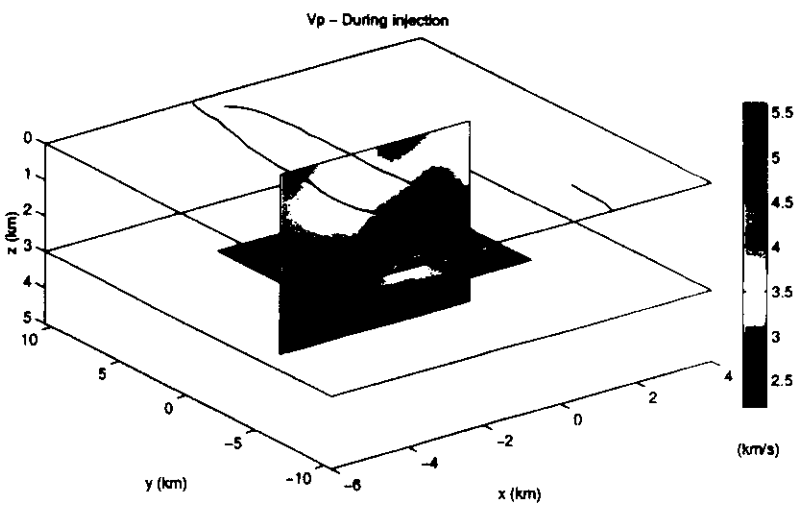

→ Before injection

→ During injection: Vp increase up to 14 %

3.3.2 On the orthogonality of the regional stress field to the fault on Leyte island

Because the well was lined, no borehole observation on the stress field could be obtained and the only sources of information come from the induced seismicity analysis. Two independent approaches have been followed. The first one concerns investigations on anisotropy by shear wave splitting analysis following Zollo and Bernard 's procedure (see reference in section 1). The other one comes from the inversion f focal mechanisms.

Shear wave splitting can be detected on all four 3-component stations. The three stations to the East of the central segment of the fault (stations G1, G2, G4) show a direction of high velocity parallel to he fault, while the station located just at the intersection of the central and western segment of the fault (G3) shows a direction of fast velocity oriented perpendicularly to the fault.

The influence of topography on the regional stress has been investigated and it is concluded that it remains negligible given the wavelength used for this investigation (a few hundred meters). The direction of fast velocity observed to the East of the fault may be linked either to a high density of fractures parallel to the fault or to a maximum horizontal stress component parallel to the fault.

For the two periods during which the seismic network involved 18 stations, focal mechanisms based on P wave first arrival polarity have been determined. 32 focal mechanisms could be obtained for the first period (fall 96) and 40 for the second period (during the high-pressure water injection in MG2RD). The determination has been conducted according to Julien and Cornet's method (same as Gephart and Forsyth except for the weighting of misfits by the uncertainties on the nodal plane orientation). For period 1 a solution compatible with 75 % of the data is obtained. It shows a poor resolution and the best solution is about 30 ° to the East of the solution obtained for anisotropy. For period 2 the solution fits also 75 % of the data. It is slightly different from the solution obtained during the first period. Hence no unique solution is derived from both types of data.

Given he results obtained at Soultz which clearly indicated that the release of shear associated with slippage could perturb significantly the stress in the neighborhood of the event, it has been decided to exclude all event which occurred within a volume that could have been perturbed by a previous event. Hence volumes of exclusion, the size of which has been adapted to the magnitude of the event, have been associated to all events so as to consider only events which affected undisturbed volumes. This leaves only 13 focal mechanisms. However, now, the inversion yields a solution compatible with 91 % of the data. Furthermore, now, the solution is the same as that derived from anisotropy investigations.

It is concluded that the fault is perpendicular to the minimum principal stress direction. This implies that this segment of the Philippine fault supports no shear stress component, a feature somewhat similar to what has been described for San Andreas fault, except that here, the fault is normal to the minimum principal stress component. This result is consistent with GPS data obtained some 30 km to the East of the fault, on Leyte. It is also consistent with the focal mechanism of a magnitude 5 earthquake which occurred about 10 km to the South of the site. Interestingly, the existence of extension basins has been described at various locations along the fault, less than 100 km from the subduction zone.

Anisotropy and homogeneous materials

→ The concept of anisotropy concerns homogeneous materials on the scale of the wave lengths used (here : λ ~240 m).

→ If we assume a relation between **crack-induced anisotropy and principal stress directions** [Crampin, 1985, Booth *et al.*, 1985, Zollo & Bernard, 1989, Gamar & Bernard, 1997]: The wave lengths controls the size of the domain in which the principal stress directions are assumed to be stationary.

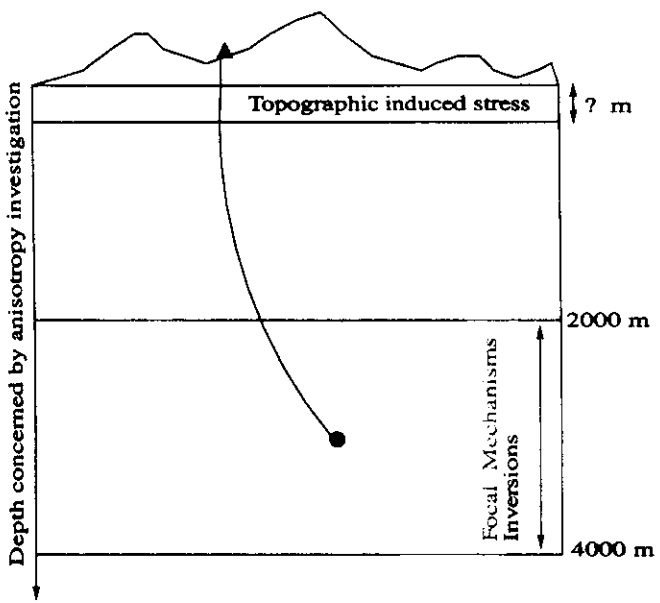

Shear wave polarization analysis

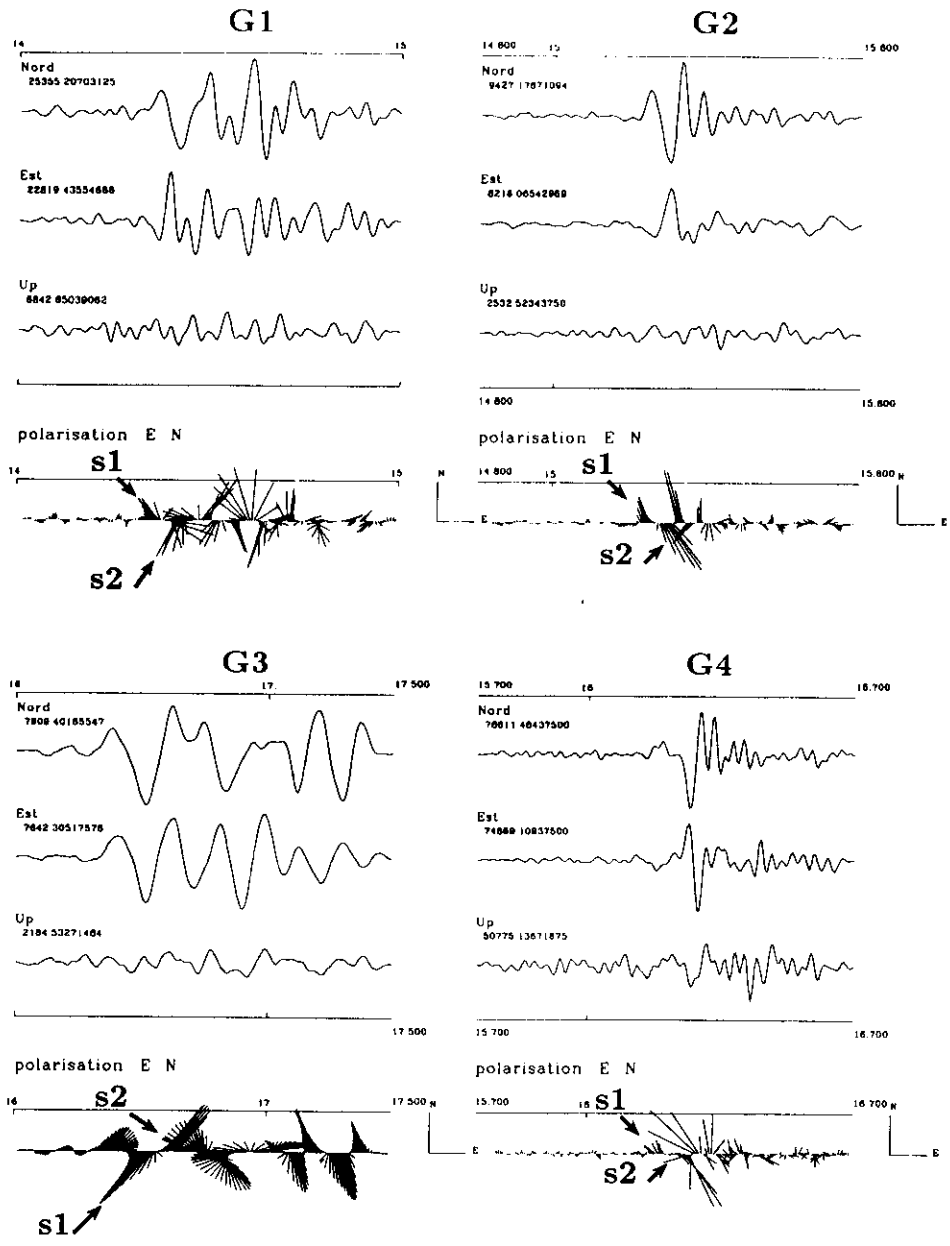

Shear wave splitting signal at stations G1, G2, G3, G4

18-6

Directions of anisotropy at stations G1, G2, G3, G4 for period 2 and 4

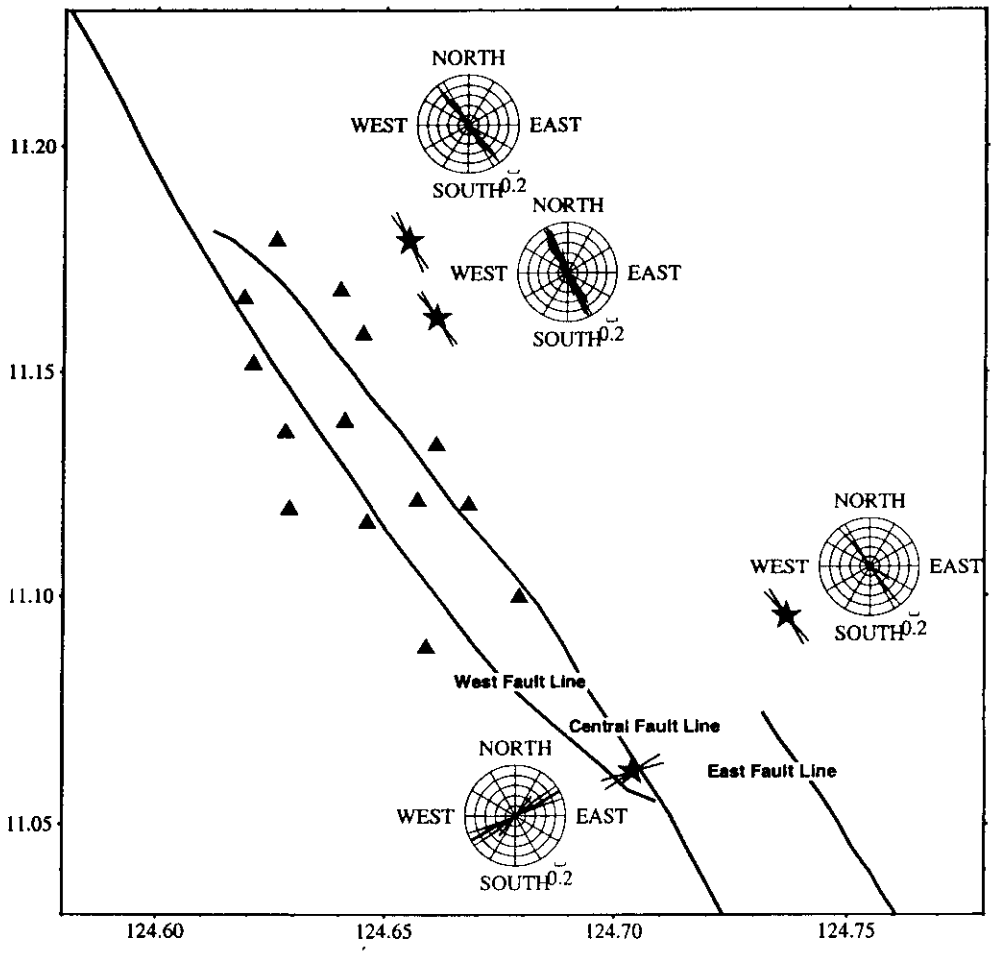

Mean topography slope at each stations

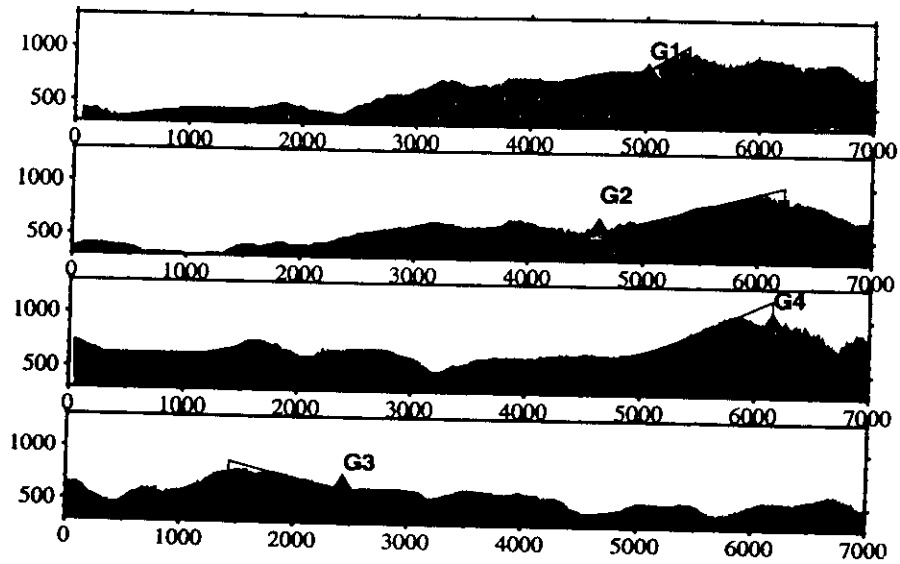

Directions of σ_1 under topographic stress perturbations

[Savage et al., 1985]

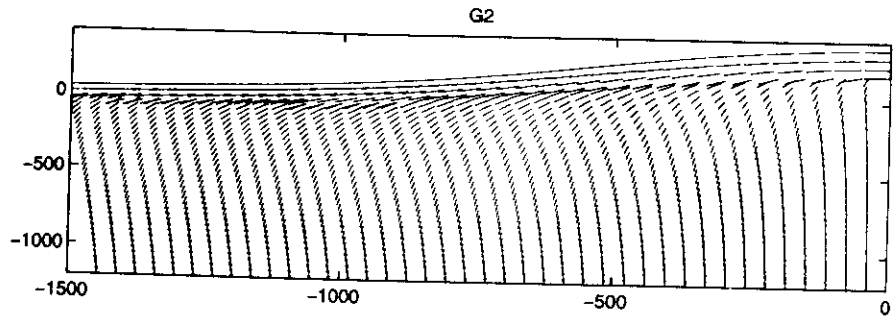

⇒ Topographic induced stress may be taken into account when analysing the volume in which the principal stress field directions are supposed stationary. It may have in important effect especially when using decametric wave lengths.

Focal mechanisms

Period 2

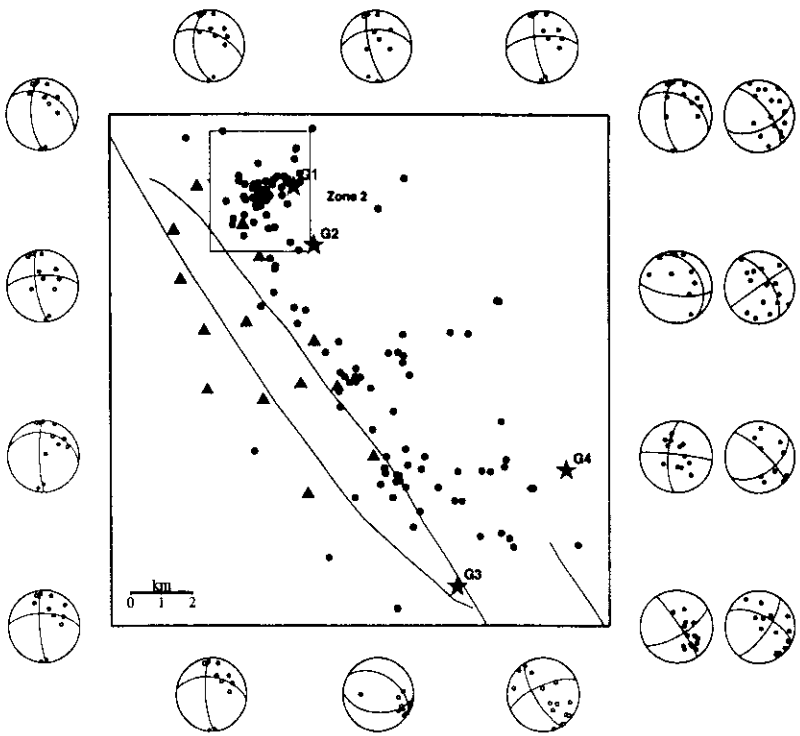

32 solutions

Period 4

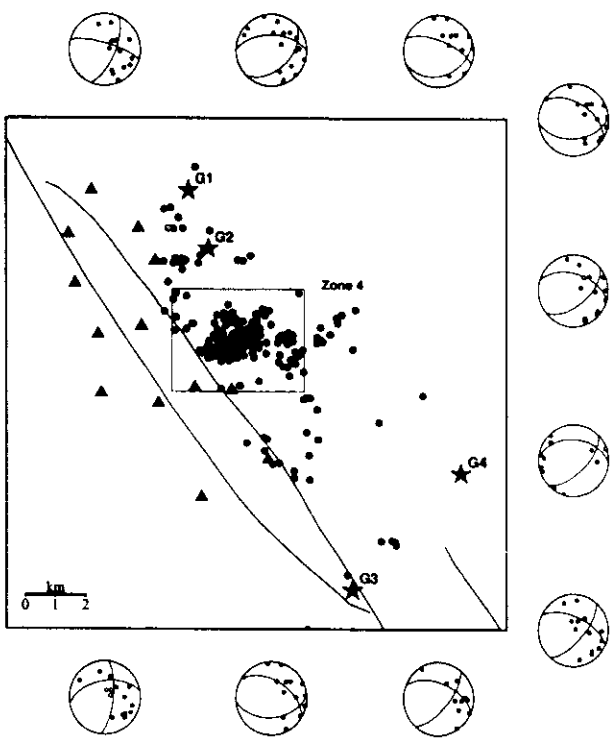

40 solutions

Focal mechanism inversions

Method

- Hypothesis 1: Uniform stress field.
- Hypothesis 2: Slip vectors are parallel to the resolved shear stress supported by the slipping planes.
- Parameters : principal stress directions (Euler angles) and aspect ratio R ($= (\sigma_2 - \sigma_1)/(\sigma_3 - \sigma_1)$)

Zone 2
23 foc.
mec.

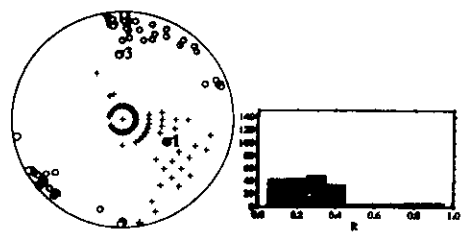

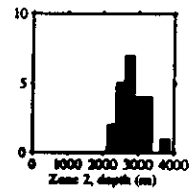

Solutions for 90 % confidence level
Best solution compatible with 75 % of the data

Zone 4
35 foc.
mec.

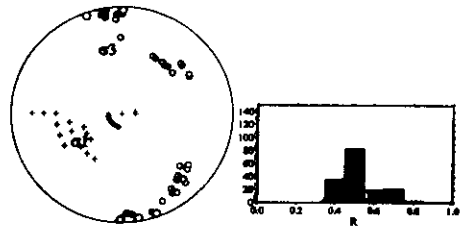

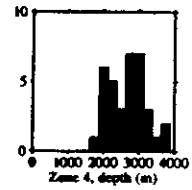

Solutions for 90 % confidence level
Best solution compatible with 75 % of the data

Zone 2
+ 4
58 foc.
mec.

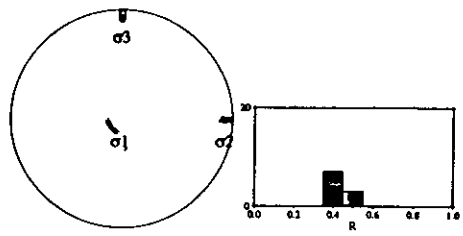

Solutions for 90 % confidence level
Best solution compatible with 60 % of the data

Anisotropy direction

at G1

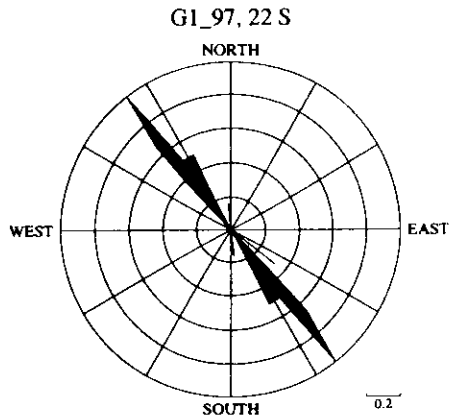

dir.~ 145°

Focal mechanism inversion

zone 2 (under G1)

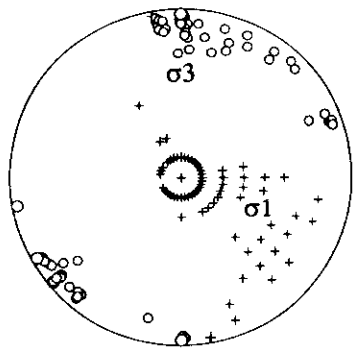

Solutions for 90 % confidence level

Anisotropy direction at G1 imposed in focal mechanism inversion

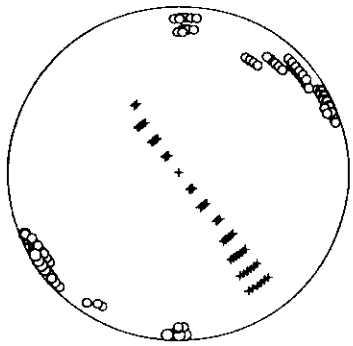

Solutions for 90 % confidence level

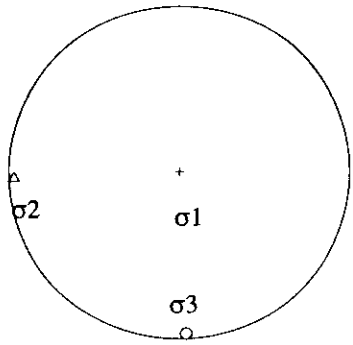

Best solution consistent with 60 % of the data

⇒ No unique solution compatible with both type of observations in the vicinity of G1 and G2

Inversion - nouvelle sélection -

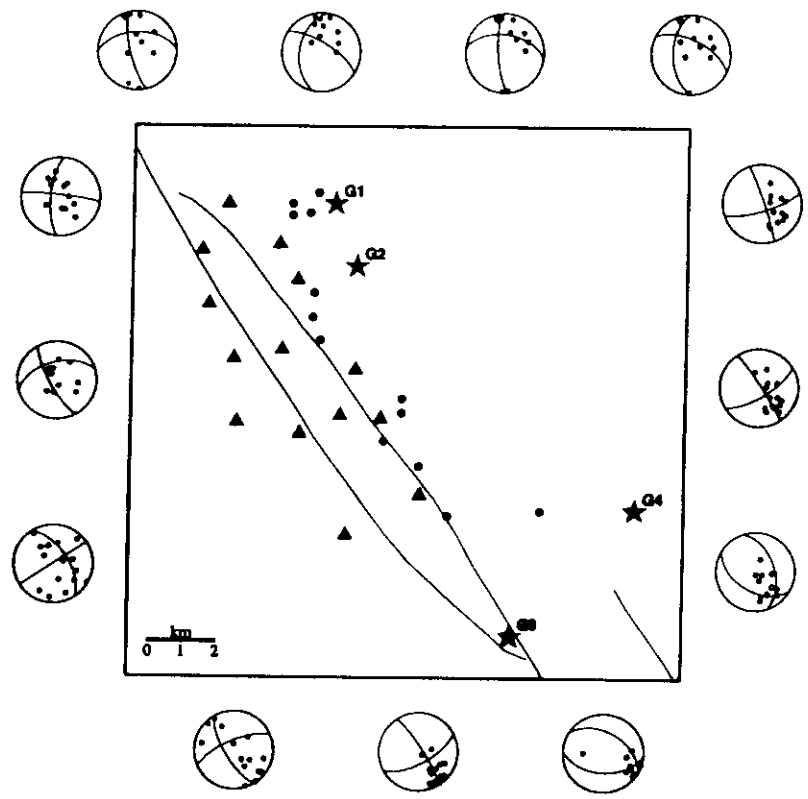

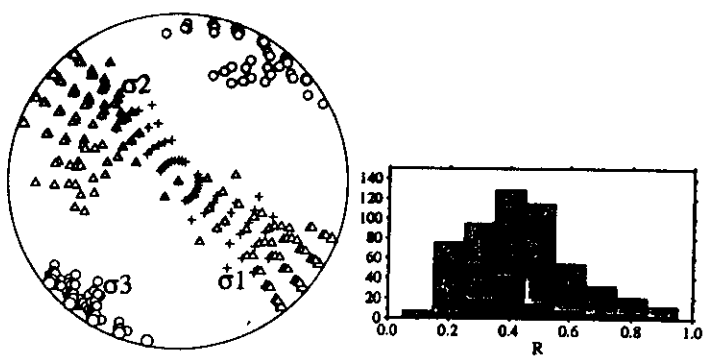

13 mech. foy.

Solutions, domaine de confiance à 90 %
Meilleure solution compatible avec 91 % des données

Here, only events occurring in undisturbed zones are considered.

18 - Ph

Directions de polarisation S

- A l'est de la Faille Centrale (G1, G2, G4) -

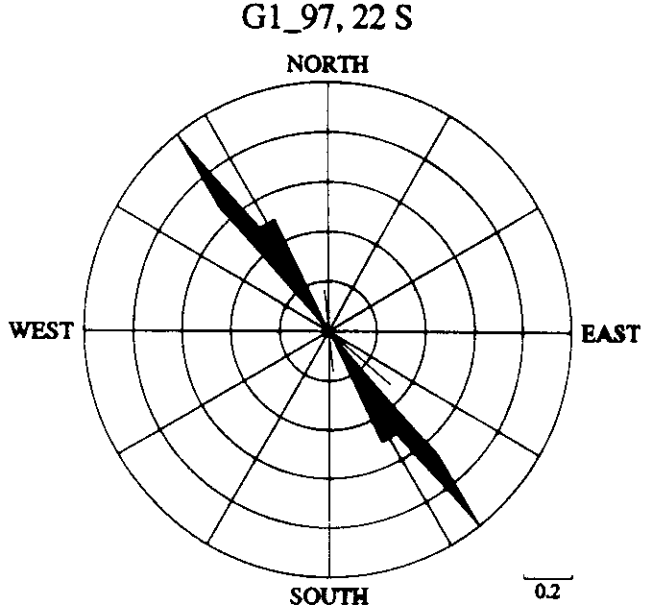

Polarisation rapide : $\sim 145°$

Inversion mécanismes au foyer

- Nouvelle sélection -

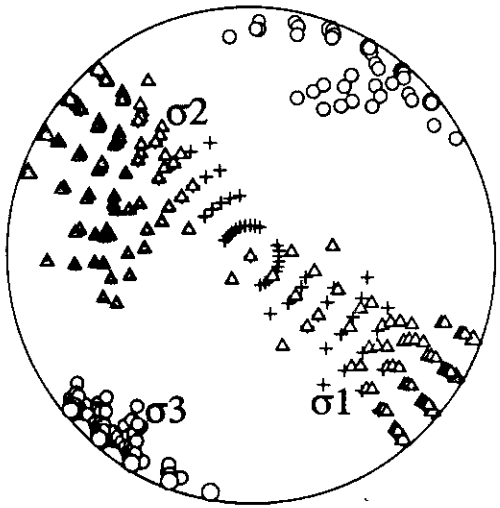

σ_1 et σ_2 : $\sim 110° - 150°$

⇒ Dans une hypothèse de contrainte, les polarisations des ondes S rapides, à l'est de la Faille Centrale, sont compatibles avec les directions principales obtenus par inversion de mécanismes au foyer.

Extension basins obsered along the fault

Bassins d'extension le long de la Faille

[Aurelio. 1992]